Materials Horizons

ROYAL SOCIETY OF CHEMISTRY

REVIEW

View Article Online
View Journal | View Issue

Cite this: *Mater. Horiz.*, 2023, **10**, 3895

Stimulus-responsive nonclose-packed photonic crystals: fabrications and applications

Yang Hu,†[a] Siyi Yu,†[a] Boru Wei,[a] Dongpeng Yang,*[a] Dekun Ma[b] and Shaoming Huang*[a]

Received 8th June 2023,
Accepted 29th June 2023

DOI: 10.1039/d3mh00877k

rsc.li/materials-horizons

Stimulus-responsive photonic crystals (PCs) possessing unconventional nonclosely packed structures have received growing attention due to their unique capability of mimicking the active structural colors of natural organisms (for example, chameleons' mechanochromic properties). However, there is rarely any systematic review regarding the progress of nonclose-packed photonic crystals (NPCs), involving their fabrication, working mechanisms, and applications. Herein, a comprehensive review of the fundamental principles and practical fabrication strategies of one/two/three-dimensional NPCs is summarized from the perspective of designing nonclose-packed structures. Subsequently, responsive NPCs with exciting functions and working mechanisms are sorted and delineated according to their diverse responses to physical (force, temperature, magnetic, and electric fields), chemical (ions, pH, vapors, and solvents), and biological (glucose, organophosphate, creatinine, and bacteria) stimuli. We then systematically introduced and discussed the applications of NPCs in sensors, printing, anticounterfeiting, display, optical devices, *etc.* Finally, the current challenges and development prospects for NPCs are presented. This review not only concludes the design principle for NPCs but also provides a significant basis for the exploration of next-generation NPCs.

Wider impact

What makes the area of study of significant wider interest?

•Stimulus-responsive nonclosely packed photonic crystals (NPCs) receive growing attention due to their potential applications in display, sensing, printing, photocatalysis, optical coating, solar energy, anti-counterfeiting, information encryption, *etc.*

What key developments in the area of study have been discussed?

• In this review, we describe the fundamentals, fabrication, structures, properties, and applications of NPCs. NPCs with exciting bioinspired functions, and the working mechanisms are sorted and delineated according to their diverse responses to physical, chemical, and biological stimuli.

What will the future of this field hold, and how will the insight in your review help shape materials science?

• NPCs with low-cost fabrication, stimulus-responsive structural colors, angle-dependent wavelengths, anti-photobleaching, and environment-friendly properties will have wide applications in various fields, involving car painting, iridescent packages, ink-free printing, low-power displays, rewritable papers, soft robotics, photonic noses, artificial smart skins, multilevel anticounterfeiting, fluorescence regulation, smart windows, and 3D printing. We believe that the design principle concluded in this review will provide a significant basis for exploring next-generation NPCs.

1. Introduction

Colors commonly originate from pigments and dyes that strongly absorb certain wavelengths of visible light. These colors depend on the chemical composition of materials; however, they suffer from color fading by photobleaching and serious environmental pollution. Unlike these chemical colors, physical structural colors based on the selective reflection of visible light by periodic structures possess various characteristics in antiphotobleaching and low toxicity. In fact, structural colors have been widely found in nature. For example, morpho butterflies can show brilliant blue color due to the diffraction of light by a layered one-dimensional (1D) structure composed of chitin on the scales.[1] (Fig. 1a) Antifogging mosquito eyes composed of a nonclose-packed two-dimensional (2D) array display a bright structural color and show potential applications for antireflection and self-cleaning (Fig. 1b).[2,3] The

[a] *School of Materials and Energy, Guangzhou Key Laboratory of Low-Dimensional Materials and Energy Storage Devices, Guangdong University of Technology, Guangzhou 510006, P. R. China. E-mail: dpyang@gdut.edu.cn, smhuang@gdut.edu.cn*

[b] *Zhejiang Key Laboratory of Alternative Technologies for Fine Chemicals Process, Shaoxing University, Shaoxing 312000, P. R. China*

† These authors contributed equally to this work.

chameleon uses periodically nonclose-packed three-dimensional (3D) structures of guanine nanocrystals in the iris cells of the epidermis to develop colors (Fig. 1c).[4] More interestingly, chameleons can regulate their skin colors by altering the distance between neighboring guanine nanocrystals by stretching their skins. Such unique characteristics can

Yang Hu

Yang Hu received his BSc degree from Hunan Institute of Science and Technology in 2018 and is currently a PhD student at the Collaborative Innovation Center of Advanced Energy Materials at Guangdong University of Technology under the supervision of Dr Dongpeng Yang and Prof. Shaoming Huang. His current research interests include responsive colloidal photonic crystals and their applications in solvent detection and anti-counterfeiting.

Siyi Yu

Siyi Yu received his BSc degree (2022) from Guangdong University of Technology (GDUT) and is currently an MS student under the supervision of Dr Dongpeng Yang and Prof. Shaoming Huang at GDUT. His research interests are in the encryption of photonic prints and applications of multifunctional photonic crystals.

Boru Wei

Boru Wei received his BSc degree from University of South China in 2021 and is currently an MS student under the supervision of Dr Dongpeng Yang and Prof. Shaoming Huang at Guangdong University of Technology. His research interest is focused on the fabrication and applications of mechanochromic photonic crystals.

Dongpeng Yang

Dongpeng Yang received his PhD in inorganic chemistry from Fudan University in 2017. He is an associate professor at Guangdong University of Technology since 2017. His current research interests focus on the self-assembly of colloidal particles into smart photonic crystals and extending their applications in color display, pigment, printing, sensing, photocatalysis, and anticounterfeiting.

Dekun Ma

Dekun Ma received his PhD from University of Science and Technology of China in 2007. He studied as a visiting scholar at Domen-Kubota Lab, Tokyo University, Japan during 2012–2013. He was promoted to Professor in Wenzhou University in 2015. Now, he is Director of Zhejiang Key Laboratory of Alternative Technologies for Fine Chemicals Process. He has been working in the research area of photofunctional materials for over 12 years. His current research interests focus on photocatalysis, photoelectrochemical cell, photonic crystal, and electrocatalysis.

Shaoming Huang

Shaoming Huang is a distinguished professor and director of the Collaborative Innovation Center of Advanced Energy Materials at Guangdong University of Technology. He received his BSc and MS degrees in Physical Chemistry from Hangzhou University in 1985 and PhD degree in Chemistry from Nankai University in 1991. His research interests mainly focus on the synthesis and properties of nanostructured carbons and their applications in energy conversion and storage devices.

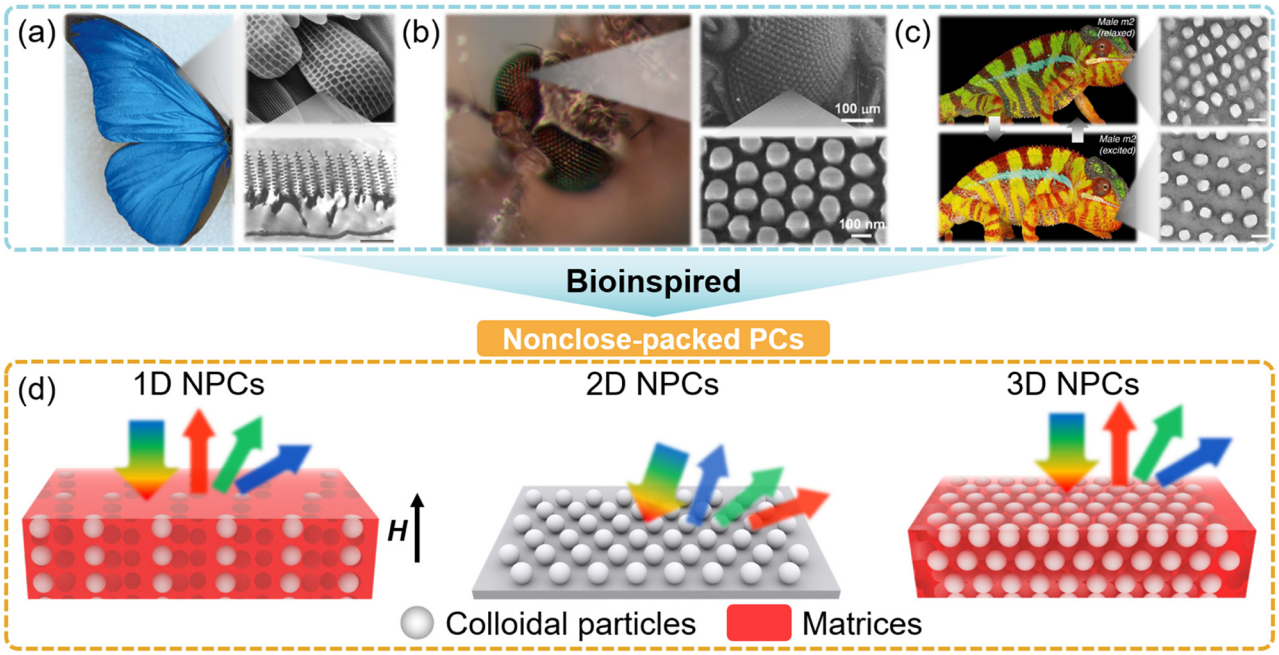

Fig. 1 (a) Digital photo of a butterfly and its SEM and TEM images. Reproduced with permission.[1] Copyright 2003, Springer Nature. (b) Digital photo and SEM images of antifogging mosquito eyes. Reproduced with permission.[2] Copyright 2007, Wiley-VCH. (c) Digital photos of a chameleon and the TEM images of the lattice of guanine nanocrystals in S-iridophores from the same individual in a relaxed and excited state. Reproduced with permission.[4] Copyright 2015, Springer Nature. (d) Schematic illustration of the structures of three types of NPCs.

be attributed to their dynamic nonclose-packing structures. These structural colors based on ordered structures with periodic refractive indexes also can be achieved by colloidal photonic crystals (PCs). Except for the structural colors, PCs have unique photonic bandgaps (PBGs), angle-dependent colors, slow-photon effects, fluorescence enhancement, *etc.* The PBG position of PCs follows Bragg's law and depends on the effective refractive index, lattice distance, and orientations.[5–7] These unique optical properties make PCs show potential applications in color displays,[8–14] printings,[15–24] sensors,[25–37] solar cells,[38,39] pigments,[40–42] anticounterfeiting,[43–56] and optical devices.[57–61]

Inspired by creature structure characteristics, PCs with nonclosely packed structures capable of mimicking creatures' functions have been developed. According to the structure periodicity, these nonclose-packed PCs (NPCs) can be divided into three categories: 1D, 2D, and 3D NPCs (Fig. 1d). In general, NPCs with colloidal particles nonclosely packed in solvents, gels, or polymer matrix were fabricated based on assembling colloidal particles in dispersion since this strategy is simple, facile, and cost-effective without the requirements of micromachining or holographic lithography.[7,62–64] Colloidal particles assemble into highly ordered structures in the matrix by balancing the electrostatic interactions between each other in the presence of shear forces as well as electric and magnetic fields. Compared to traditional close-packed ones, NPCs have the advantage of a flexible and tunable structure due to their high polymer volume fraction.[65–69] These merits offer new functions and specific applications of NPCs in sensing, displays, printing, anticounterfeiting, and optical devices. Although PCs have been well-reviewed recently,[7,35,62,66,69–73] most PCs possess closely packed structures. The preparation strategies, functionalities, and applications of NPCs have hardly been well-summarized.

In this review, we will discuss the progress of NPCs in the aspect of fabrications, structures, functions, and applications. In the following sections, a brief overview of the strategies for fabricating nonclose-packed PCs is presented first, including magnetic assembly for 1D NPCs, reactive ion etching for 2D NPCs, electrostatic self-assembly, and two-step filling for 3D NPCs. Then, the NPCs are summarized according to their unique functions of mechanochromic, thermochromic, magnetochromic, electrochromic, chemical-chromic, and biochromic optical performances. Based on their unique stimulus-responsive properties, the potential applications of NPCs are also discussed in detail. Finally, a summary and some perspectives on the remaining challenges of this research field are proposed.

2. Classification, principles, and fabrications

The NPCs are first divided into 1D, 2D, and 3D NPCs based on their differences in periodicity. Then, their optical principles (Bragg's law), color tunability, and fabrications are presented and discussed.

2.1 1D NPCs

1D PCs are composed of two materials with different refractive indices arranged alternately along one direction, and most of

them resemble the laminar structure of the butterfly wings.[74–77] Herein, we only discuss the 1D colloidal PCs with nonclose-packed structures. 1D NPCs require magnetic colloidal particles including Fe_3O_4,[78] Fe_3O_4@SiO_2,[79] and Fe_3O_4@carbon[80] particles as building blocks. By applying a magnetic field, these particles assemble into ordered structures only along the magnetic direction, and nonclosely packed structures are achieved by balancing the magnetic attraction forces and electrostatic repulsions between particles.[78,81–84] When superparamagnetic particles dispersed in solution are exposed to the external magnetic field, they will be subjected to two types of magnetic force. One is the dipole–dipole force of the magnetic field interaction between one dipole and another, and the other is the stacking force caused by the gradient of the applied magnetic field.[85] As shown in Fig. 2a–d, applying an external magnetic field induces a magnetic dipole moment m, a magnetic field H in the direction of the magnetic field in the superparamagnetic particle, a magnetic attractive force $F_{ma} = 6(m^2/d^4)$ between two adjacent particles arranged along the magnetic field, and a repulsive force $F_{mr} = 3(m^2/d^4)$ between two particles arranged perpendicular to the magnetic field, where d is the center–center distance. The magnetic packing force $F_p = \nabla(mH)$ can drive superparamagnetic particles toward the region of maximum magnetic field strength.[82,86,87] The highly charged surface of colloidal particles usually generates electrostatic repulsion, which is also essential for the assembly of magnetic colloidal particles into ordered arrays. Under the external magnetic field, superparamagnetic colloidal particles form chains in solution. The electrostatic repulsion between charged colloids in each chain increases with the closer colloidal particles and eventually forms 1D NPCs as the attractive and repulsive forces of colloidal particles reach a balance.

The diffraction wavelength of the 1D NPCs can be described by Bragg's law (eqn (1)), where m, d, and λ are the diffraction order, lattice distance, and reflection wavelength, respectively. θ is the angle between the reflected beam and the diffraction crystal plane. According to Bragg's law, the λ of 1D NPCs can be adjusted by n, d, and θ. In fact, due to the low content of magnetic particles (<1%), n is usually determined by dispersions. Hence, in most cases, d and θ determined by magnetic field strength and orientation, respectively, are two effective and widely used parameters to alter the λ.[88] The reflectance of NPCs is dependent on the refractive index contrast (Δn) and the order degree. The Δn between magnetic colloid (n = 1.7–2.42) and matrices (n = 1.3–1.5) can be calculated by eqn (2), where n_c and n_m are the colloidal particles and the matrices, respectively. The large Δn is considered as an important reason contributing to the high reflectance of 1D NPCs even at low-volume fractions of particles (<1%). When the magnetic field strength is enhanced, the surface-to-surface distance (d_{s-s}) of neighboring

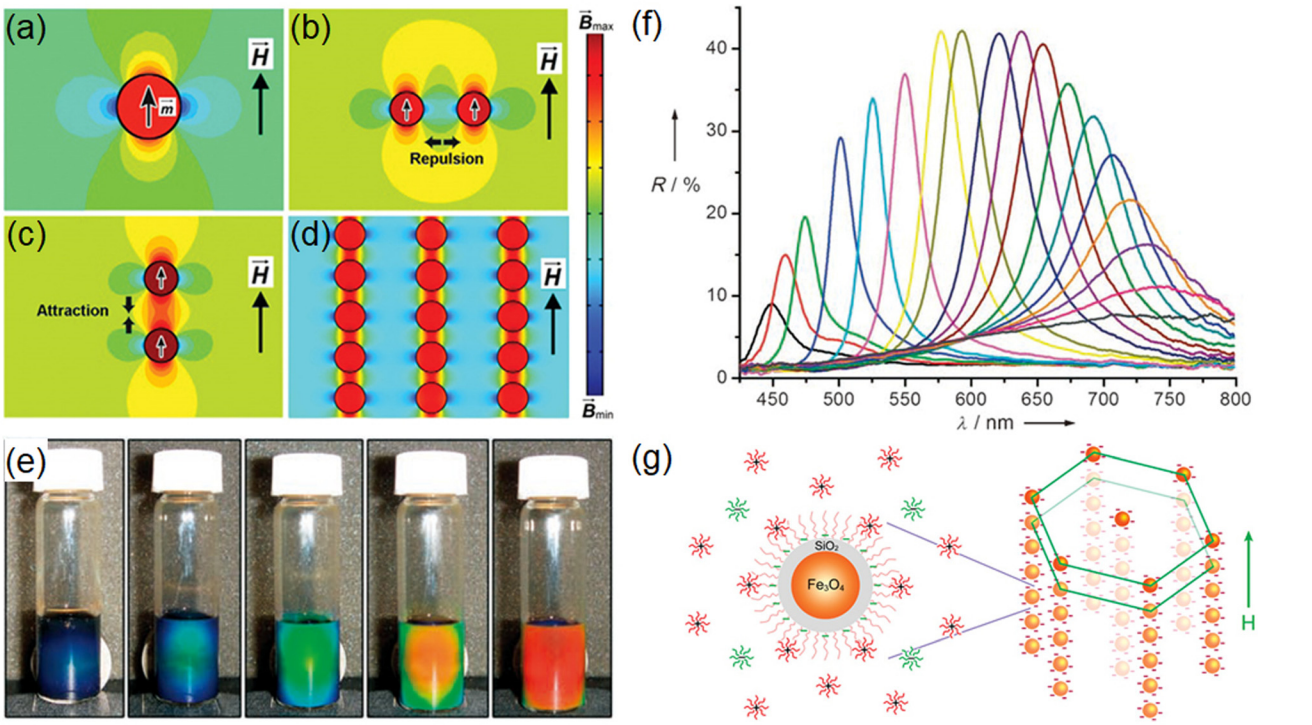

Fig. 2 (a) Magnetic field distribution around a superparamagnetic particle with a dipole moment in the same direction as the external magnetic field. The repulsive (b) and attractive (c) dipole–dipole forces in different particle configurations drive the formation of particle chains along the magnetic field (d). The color bar on the right shows the relative strength of the local magnetic field. Reproduced with permission.[85] Copyright 2012, American Chemical Society. (e) Photographs of colloidal crystals formed in response to an external magnetic field. (f) Dependence of the reflection spectra at normal incidence of the colloidal crystals on the distance of the sample from the magnet. Reproduced with permission.[78] Copyright 2007, Wiley-VCH. (g) Schematic illustrations showing the creation of negative charges on the surface of superparamagnetic colloids in nonpolar solvents. Reproduced with permission.[91] Copyright 2009, American Chemical Society.

particles of the same nanochain decreases, which can be calculated by eqn (3), where d_c is the diameter of colloidal particles. Therefore, only nonclosely packed structures can realize the dynamic regulation of λ and colors under magnetic fields.[63]

$$m\lambda = 2nd\sin\theta \quad (1)$$

$$\Delta n = n_c - n_m \quad (2)$$

$$d_{s-s} = d - d_c \quad (3)$$

Magnetic attraction and electrostatic repulsion provide favorable conditions for the assembly of colloidal particles.[89] Therefore, uniform colloids with superparamagnetic properties, adjustable sizes, and highly-charged surfaces are ideal candidates for constructing 1D NPCs. Yin and coworkers synthesized nearly monodisperse superparamagnetic ''colloidal nanocrystal clusters'' (CNCs) of polyelectrolyte-covered magnetite (Fe_3O_4) with controllable sizes of 30–200 nm by a high-temperature polyol process.[90] Each Fe_3O_4 CNC is composed of a large number of interconnected Fe_3O_4 nanocrystals with a diameter of approximately 10 nm. Such unique polycrystalline structures render the CNC exhibiting superparamagnetic properties and high saturation magnetization strength beyond the critical size (30 nm), over which single crystal particles show ferromagnetic properties. Due to the grafting of negatively charged polyelectrolytes on their surfaces, these Fe_3O_4 CNCs are highly charged and well dispersed in water. The strong electrostatic repulsion can balance the magnetic attractions, allowing the self-assembly of Fe_3O_4 CNCs at a large d_{s-s} (154 nm) under a magnetic field and excellent color tunability. As shown in Fig. 2e and f, Fe_3O_4 CNCs-based 1D NPCs show brilliant structural colors and high reflectance. The structural color and reflection wavelength covering all the visible ranges ($\Delta\lambda > 300$ nm) can be precisely modulated by the magnetic field strength.[78,91]

Unfortunately, these Fe_3O_4 CNCs cannot assemble into 1D NPCs in organic solvents due to the charge-screening effect of polyelectrolytes in solvents, restricting their practical applications. To address this issue, Yin and coworkers coated a uniform layer of silica shell on the surface of Fe_3O_4 CNC by a sol-gel process.[79,92] The Si–OH on the surface of Fe_3O_4@SiO_2 generates charge separation in most polar solvents (silica–OH $\rightarrow$ silica–O^- + H^+), resulting in strong electrostatic repulsion among particles and the packing of Fe_3O_4@SiO_2 particles in polar solvents into 1D NPCs. However, it is exceedingly difficult to realize strong electrostatic repulsion among particles in less polar or nonpolar solvents due to the high energy potential barriers for surface charge in these solvents.[93,94] The same group has prepared *n*-octadecyltrimethoxysilane (ODTMS)-capped Fe_3O_4@SiO_2 particles to disperse these particles in 1,2-dichlorobenzene (DCB) (Fig. 2g). The charge separation is greatly enhanced by introducing sodium bis (2-ethylhexyl)sulfosuccinate (AOT) as a charge control agent. The AOT in DCB can form giant reverse micelles dissolving counterions, promoting surface charge separation of particles. Therefore, Fe_3O_4@SiO_2-ODTMS can form 1D NPCs in less polar DCB, similar to the results in the water.[91] In addition, replacing the solvent with a polymerizable monomer such as polyethylene glycol diacrylate (PEGDA) and combining with UV curing can fix the ordered structures 1D NPCs and facilitate their applications.[15,95]

2.2 2D NPCs

2D NPCs are of wide interest due to their potential applications in ordered array masks,[96–99] surface patterning,[100,101] superhydrophobic substrates,[102–105] and biosensors.[1,106,107] However, 2D PCs with hexagonal or square closely packed rather than nonclosely packed structures were prepared mostly because of their stable mechanical stability and the thermodynamically lowest state.[100,108,109] To date, the fabrication of 2D NPCs remains a big challenge. The early strategy for constructing 2D NPCs was mainly based on the reactive ion etching (RIE) of 2D close-packed PCs.[110–112] For example, 2D PCs with close-packed arrays of polystyrene (PS) microspheres on silicon substrates were fabricated by a self-assembly approach. 2D NPCs were then obtained by exposing 2D PCs to RIE with oxygen plasma that can thin the PS spheres.[113] Reactive ion etching using pure oxygen plasma tends to result in a rough surface of PS spheres, while RIE mixing with a high percentage of CF_4 gas can obtain relatively smooth PS particles.[111] 2D NPCs can also be prepared directly by the self-assembly of colloidal particles. Wang *et al.* prepared 2D NPCs from $CaCO_3$-impregnated coated hydrogel spheres formed by *in situ* biomineralization.[108] The d_{s-s} can be well regulated by controlling the dip-coating speed and the concentration of colloidal particles. In addition to the preparation of 2D NPCs by RIE and self-assembly, a soft lithography technique for the preparation of 2D NPCs was reported by Yang *et al.*[114–117] As shown in Fig. 3a, a layer of close-packed 2D PCs was transferred to the surface of PDMS stamps, and the solvent was used to swell the PDMS to increase the lattice distance to obtain nonclosely packed structures. A modified microcontact printing (μCP) transfer technique can transfer the 2D NPCs to arbitrary solid substrate surfaces.[118] However, these methods require time-consuming processes and complex equipment, thus limiting their applications. In 2004, Jiang *et al.* developed a spin coating strategy to prepare 2D NPCs (Fig. 3b). According to their methods, silica particles were first concentrated in ethoxylated trimethylolpropane triacrylate (ETPTA) to form a silica/ETPTA precursor solution with nonclosely packed structures. Taking advantage of the spin coating technique, the precursor solution can be nonclosely packed with only one layer with large areas (Fig. 3c and d).[101,119–121]

2.3 3D NPCs

Typically, 3D NPCs with a low filling fraction (<0.5) and face-center-cubic (fcc) lattice are fabricated by assembling colloidal particles into polymers or solvents. Similar to conventional PCs, colloidal particles are size-tunable, highly charged, and monodisperse. To date, a variety of building blocks including PS,[122,123] PNIPAM,[124–126] SiO_2,[127,128] Fe_3O_4@SiO_2,[129,130] CeO_2@SiO_2,[131] and ZnS[132,133] have been successfully used to

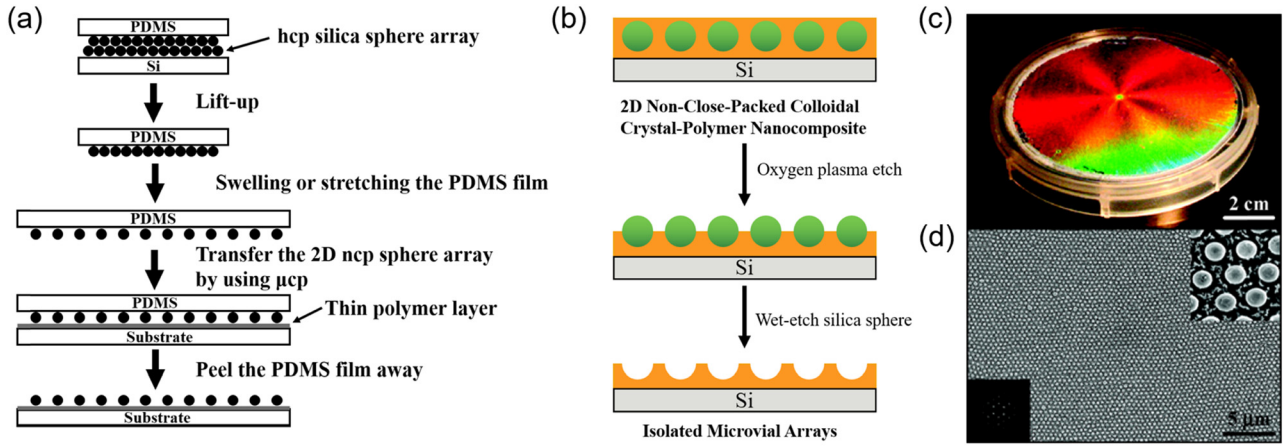

Fig. 3 (a) A schematic illustration of the procedure for the fabrication of a 2D NPC array of spheres with a tunable lattice structure. Reproduced with permission.[114] Copyright 2005, American Chemical Society. (b) Schematic illustration of the experimental procedures for making periodic polymer microvial arrays using 2D nonclose-packed colloidal crystal-polymer nanocomposites as templates. Reproduced with permission.[120] Copyright 2005, The Royal Society of Chemistry. (c) Photograph of a sample on a four in. silicon wafer illuminated with white light, (d) typical SEM image of the sample shown in (c). The top inset shows a magnified SEM image, and the bottom inset shows a Fourier transform. Reproduced with permission.[101] Copyright 2007, American Chemical Society.

prepare 3D NPCs. For matrices, most polar solvents and acrylates-based polymers with high boiling points and low viscosity are ideal candidates. The 3D NPCs display diverse functions through the rational design of their components and structures. For example, 3D NPCs show a unique metastable property when nonclosely packed silica particles are wrapped by ethylene glycol.[134] The polymeric matrices not only play the role of fixing the nonclosely packed structure[128,135,136] but also endow 3D NPCs to possess smart and unique functionalities.[28,123,137] For instance, inspired by chameleons' color regulation mechanism, mechanochromic 3D NPCs show force-dependent colors based on the variation of the surface-to-surface distance (d_{s-s}) between neighboring particles thanks to the nonclose-packing structures, which cannot be realized by PCs with closely packed structures. The d_{s-s} of the neighboring particles of 3D NPCs can be calculated by Bragg's law (eqn (4) and (5)).[138–140] m and λ are the diffraction order and the reflection wavelength, n_i and f_i are the refractive index and volume fraction of each component of 3D NPCs, D_{id} and D_c are the interparticle distance and diameter of colloidal particles, respectively, and θ is the angle between the reflected beam and the normal.

$$m\lambda = 1.633 D_{id}\sqrt{n_i^2 f_i - \sin^2\theta} \quad (4)$$

$$d_{s-s} = D_{id} - D_c \quad (5)$$

Indeed, colloidal particles will experience different interactions (electrostatic force, long-range attractive force, solvation force, magnetic force, and shear force) during the assembling process, depending on their fabrication strategies. Basically, the self-assembly strategies used for constructing 3D NPCs can be divided into three categories: (1) electrostatic self-assembly, (2) magnetic field-induced assembly, and (3) shear-induced assembly. In addition, micromachining the 3D CPCs can also obtain 3D NPCs.[141–147]

2.3.1 Electrostatic self-assembly. Traditionally, three different interactions between particles have been regarded as the major reasons for driving the self-assembly of particles into nonclose-packed structures: (1) electrostatic repulsion,[122,123,148–151] (2) the interaction balance between long-range attraction and electrostatic repulsion,[134,152] and (3) solvation forces.[153,154] Asher *et al.* reported that sulfate groups-modified PS particles can spontaneously self-assemble into NPCs in an aqueous solution by electrostatic repulsion.[122] The particles are negatively charged so that PS spheres can self-assemble into ordered arrangements even with the interparticle distance over one μm under low ionic strengths. Subsequently, they introduced highly purified nonionic polymerizable monomers into the surrounding PS colloidal crystals and fixed the ordered structures by forming a hydrogel network with UV irradiation.[123] They also demonstrated that the nonclose structure of such NPCs could be fixed when the water medium was replaced by polymerizable monomers. However, this method usually involves a time-consuming process and elaborate procedures, which may restrict their applications.

Ge *et al.* suggested that the self-assembly of silica particles into NPCs is caused by the balance between long-range attraction and electrostatic repulsion.[134] They developed a method of evaporation-induced supersaturation precipitation to prepare NPCs (Fig. 4a). Briefly, silica particles were dispersed in the mixture of ethanol and a target solvent with a high boiling point. After evaporating ethanol at 90 °C, silica particles will spontaneously self-assemble into a liquid "metastable" 3D NPC (Fig. 4b). They divided the formation of metastable CCAs into two processes. First, as the volume fraction of silica rises to a supersaturated value (12–20%) due to the evaporation of ethanol, the concentration of counterions and ionic strength increases, diminishing the electrostatic repulsion and leading to silica precipitation. Second, these precipitated particles quickly self-assemble into nonclosely packed structures by balancing the strong electrostatic repulsions and long-range attractions among particles.[155] The long-range attraction between particles was induced by a charged glass wall.

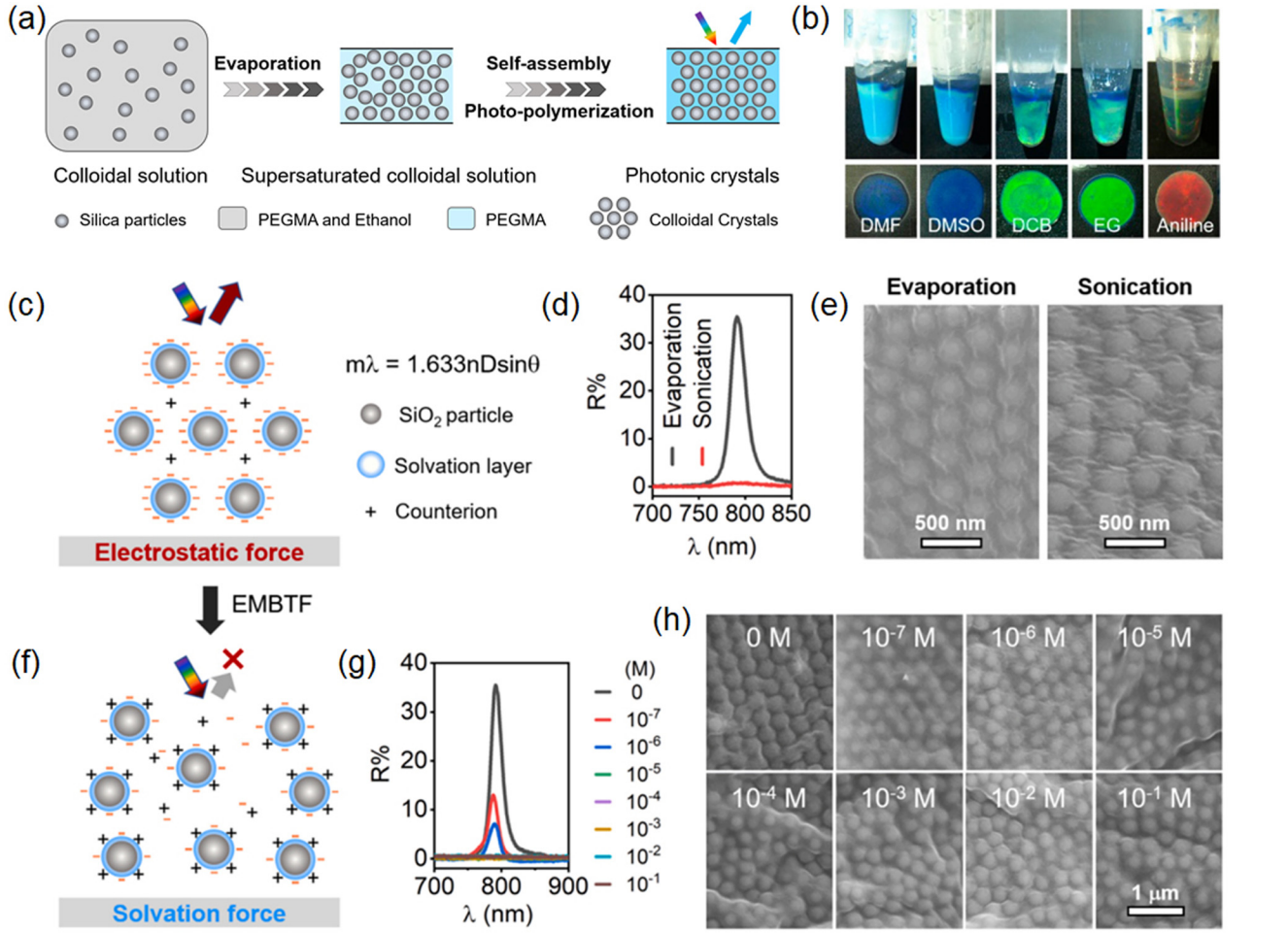

Fig. 4 (a) Schematic illustration of the fabrication of SiO_2-PEGMA photonic paper through the self-assembly of silica particles in the PEGMA and subsequently fixed through photopolymerization. (b) Photos of metastable CCAs formed in different solvents. Reproduced with permission.[134] Copyright 2013, American Chemical Society. (c) Schematic illustration of the repulsion force induced the self-assembly of silica particles into highly-ordered structures. (d) Reflection spectra and (e) SEM images of MPCs were fabricated through evaporation and sonication strategies. (f) Schematic illustration of the assembly behavior of silica particles when the solvation force dominates repulsion. (g) Reflection spectra and (h) corresponding SEM images of MPCs fabricated with different concentrations of EMBTF. Reproduced with permission.[156] Copyright 2022, Elsevier.

Although the long-range order is only effective with a few numbers of periodic structures, the newly formed ordered structures can act in a manner comparable to that of the glass wall and result in the unexpected long-range order.

The assembly behavior of particles in acrylates seems more complex in solvents. Kim *et al.* fabricated silica-based 3D NPC through a similar strategy developed by Ge's group, except that the target solvents were replaced by poly(ethylene glycol)phenyl ether acrylate (PEGPEA). Unlike the electrostatic repulsion between silica particles in solvents, they point out that the solvation repulsion based on the thick solvation layer coated on silica particles is the key to the ordered structure.[153] When the critical concentration is reached, and the solvation layers between the particles start to overlap and the particles repel each other due to the disjoining pressure, thus inducing the assembly of the particles into the ordered structure. The dense solvation layer, formed by the formation of hydrogen bonds between the acrylate group of PEGPEA and the silanol group of particles, stabilizes the colloidal suspension for several months. However, the van der Waals attraction and electrostatic repulsion among particles may also have a great influence on the silica/PEGPEA system and cannot be repelled due to the very limited interparticle distances.

Very recently, our group demonstrated that the self-assembly of silica particles is mainly driven by electrostatic repulsion rather than the solvation layers and van der Waals attraction.[156] We prepared silica/di(ethylene glycol)ethyl ether acrylate (DEGEEA) 3D NPCs through a similar strategy to that created by Ge *et al.* Interestingly, it was found that silica particles can form long-range order with a relatively low volume fraction (15%) in DEGEEA (Fig. 4c–e) due to the less polar properties of DEGEEA. Further experimental results proved that a trace amount of ethanol (6%) existing in the PC suspension after ethanol evaporation acts as a charge control agent to dissolve counterions. This leads to the long-range packing of silica particles with quite a large d_{s-s} of 132 nm, which exceeds

the effective distance caused by either solvation layers (10–40 nm) or van der Waals attraction (<20 nm). To further manifest the critical role of electrostatic repulsions, we introduce ionic liquids to selectively screen the electrostatic forces since the electrostatic force is extremely sensitive to ionic strength while the solvation force is not (Fig. 4f–h).[94] As expected, the reflectance of silica/acrylates PCs is highly sensitive to the ionic strength and inversely proportional to the concentration of ionic concentration, firmly verifying that the electrostatic is the key that drives the nonclose-assembling of silica particles. Moreover, the silica/acrylates PCs show outstanding stability in the presence of ionic liquid, strongly suggesting that solvation repulsion only can protect particles from aggregation. All these results vividly demonstrate that the electrostatic repulsion rather than the solvation repulsion drives the self-assembly of silica particles in acrylates.

2.3.2 Magnetically-induced assembly. 3D NPCs with nonmagnetic colloidal particles, magnetic colloidal particles, and magnetic nanorods as structural blocks can be fabricated by the magnetic field-induced assembly.[83,157] Yin *et al.* reported the nonclose-packed ordered structures of nonmagnetic colloidal particles in magnetic fluids induced by external magnetic fields.[158] Based on the magnetic hole effect, the photonic structure evolved from a 1D nonclose-packed structure to a 3D nonclose-packed structure as the external magnetic field strength and gradient were enhanced. 3D NPCs with reflectance (83%) were produced within minutes in strong magnetic fields with large magnetic field gradients (Fig. 5a).

External magnetic fields usually have two effects in inducing the assembly of magnetic colloidal particles into 3D-ordered structures. On the one hand, magnetic stacking forces driven by magnetic field gradients induce the local concentration of particles and thus trigger the crystallization of colloidal particles; on the other hand, interparticle dipole–dipole interactions can be controlled by the magnetic field strength, which leads to 3D photonic structure transitions between different phases.[84] He *et al.* reported the reversible transition of superparamagnetic colloidal particles from polycrystalline face-centered cubic to single-crystal-like hexagonal packing structures under the control of an external magnetic field (Fig. 5b and c).[129] Due to its nonclose-packed structure, the polydispersity of colloidal particles over 7% crystallization is also allowed.

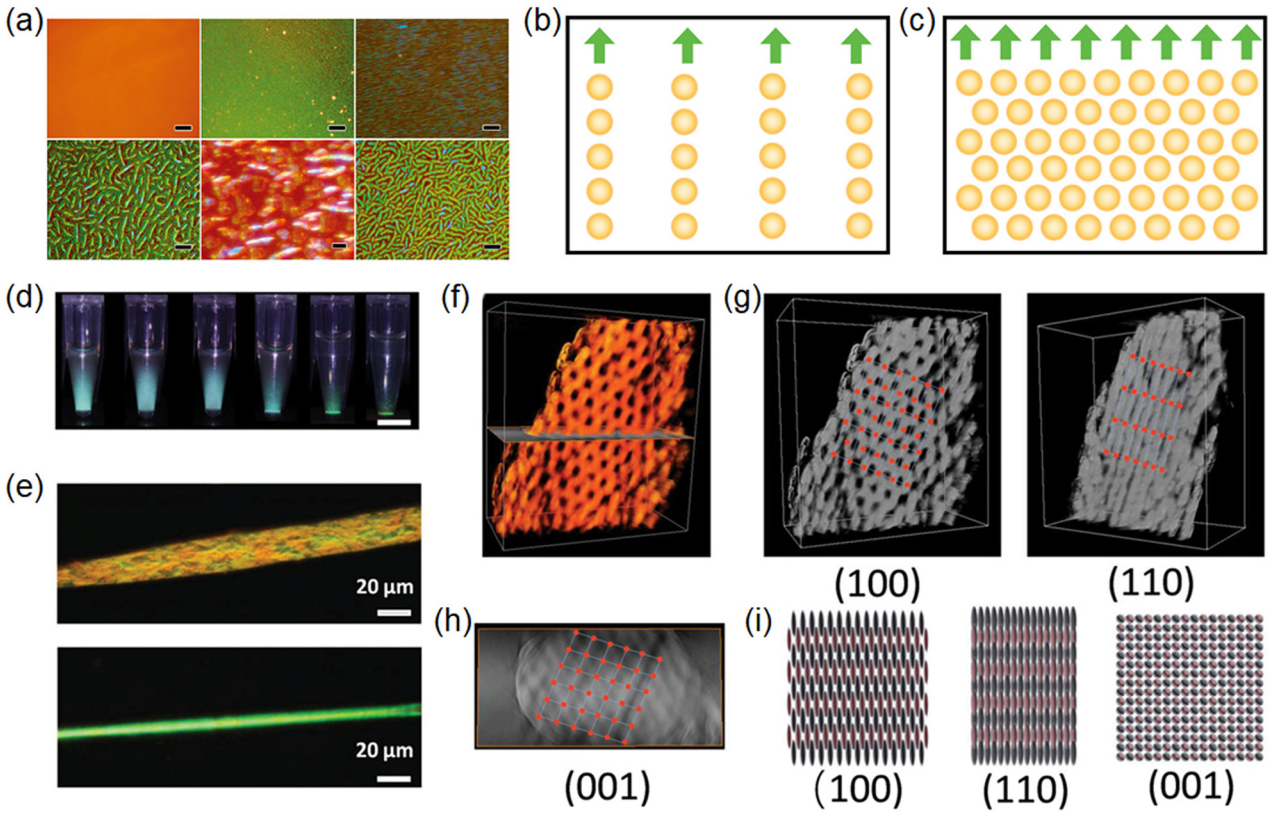

Fig. 5 (a) Optical microscope images showing the assembly of 185 nm PS beads (volume fraction of 3%) dispersed in the ferrofluid (volume fraction of 2%). Reproduced with permission.[158] Copyright 2010, American Chemical Society. (b) At low concentrations, the structural color results from the collective Bragg diffraction of individual chain assemblies. (c) The single-crystalline-like 3D structures diffract light as a whole unit. Reproduced with permission.[129] Copyright 2012, The Royal Society of Chemistry. (d) Digital pictures showing the self-assembly of Fe_3O_4@SiO_2 nanorods in the mixture of water and ethanol under a vertical magnetic field. Scale bar: 2 mm. (e) Dark-field optical microscopy images. (f) 3D rendering of the TEM tomography of a photonic crystal. (g) 3D rendering of the same crystal with two different exposed facets as indicated, leading to two typical projection patterns. (h) A horizontal cross-section of the reconstructed photonic crystal with exposed (001) facets. (i) Schematic illustrations of the projections of the photonic crystal with exposed (100), (110), and (001) facets, respectively. Reproduced with permission.[159] Copyright 2022, Wiley-VCH.

Recently, Li *et al.* reported the magnetically-induced assembly of monodisperse Fe_3O_4@SiO_2 nanorods into body-centered-tetragonal (bct) NPCs (Fig. 5d and e).[130,159] At the nanoscale, magnetic nanorods are assembled along a size-dependent critical angle. Shape-induced anisotropic interactions generate two domains of attraction separated by a central domain of magnetic repulsion. It guides the nanorods to assemble into bct crystals along the critical axis rather than tending to attach laterally in entropy-dominated assemblies or endwise in magnet-to-pole attraction. As shown in Fig. 5f–i, the bct NPCs contain large pores due to their nonclose-packed structure, which can allow for a fast and sensitive colorimetric response to surrounding dielectric changes.

2.3.3 Shear-induced assembly. The hard core-soft shell colloidal spheres can be self-assembled under shear-induced into large area NPCs with the core as the building block and the soft shell as the matrix.[160–164] For example, Zhao *et al.* assembled PS-PMMA-PEA core–shell particles into NPC flexible films by bending-induced oscillatory shear (BIOS) technique.[165] The PEA shell layer softened and filled the interstices between the spheres as they were heated. The PMMA interlayer covalently grafted the PEA chain to the PS core, thus contributing to the stress resistance of the PS core. During the BIOS process, the PS-PMMA-PEA particles gradually formed an ordered structure under the shear force and reached equilibrium after 40 shear oscillations. To prepare large-area NPC films at room temperature, Wang *et al.* introduced poly(2-ethylhexyl acrylate) with a lower glass transition temperature (T_g) into the shell layer and used an industrial roll-to-roll process to achieve the large-scale production of NPC films.[166]

2.3.4 Self-assembly combined with micromachining. Compared to 3D CPCs with filling fractions limited to the range of 0.74–1, 3D NPCs could have higher porosity, stronger optical scattering, and more intense reflections.[143] Meseguer and Fenollosa prepared silica opal with nonclose-packed structures through a combination of silica self-assembly, thermal sintering, and etching techniques (Fig. 6a).[141] The silica particles in this structure are connected by a tubular neck. However, the instability of the structures may restrict their practical application. Yang *et al.* reported a strategy for the preparation of 3D NPCs based on 2D nonclose-packed colloidal crystals in combination with photopolymerization techniques (Fig. 6b).[167] Specifically, the photoresist monomer was rotated with 2D NPCs on the silicon wafer and polymerized by UV irradiation. The above operation was then repeated by stacking another layer of 2D NPCs until 3D NPCs with the desired number of layers and spacing were obtained. Recently, Wu *et al.* prepared 3D NPCs composed of ZnS particles and polymers using a two-step filling strategy (Fig. 6c).[133] 3D CPCs templates were firstly prepared by the self-assembly of ZnS@SiO_2 particles, and then the gaps were filled with the polymer. The 3D NPCs were created by filling the polymer a second time after the silica shell of the colloidal particles was etched with HF solution. In addition, the d_{s-s} of the 3D NPCs could be flexibly controlled by the silica shell thickness. Despite the large Δn (0.4–0.6), the reflectance of the NPC (45%) is not as high as expected, which may be due to the interference of the etching process on the order degree.

To achieve brilliant structural colors, very recently, our group fabricated NPCs with high color saturation and adjustable structural colors by self-assembling the nonclosely packed ZnS–silica particles in trimethylolpropane ethoxylate triacrylate (ETPTA).[168] Due to the large Δn (0.142–0.230), the ZnS–silica NPCs show intense reflectance (maximal: 90%), wide photonic bandgaps, and large peak areas, 2.6–7.6, 1.6, and 4.0 times higher than those of silica NPCs, respectively. Benefiting from the nonclose-packing structure, the colors of NPCs can simply adjust the volume fraction of particles with the same size, which is more convenient than the conventional way of altering particle sizes. Furthermore, thanks to the core–shell structure of ZnS–silica particles, diverse derived photonic superstructures were fabricated by co-assembling ZnS–silica and silica particles into NPCs or by selectively etching silica or ZnS of ZnS–silica/silica and ZnS–silica NPCs (Fig. 6d and e). A new information encryption technique was developed based on the unique reversible ''disorder–order'' switch of water-responsive photonic superstructures. In addition, ZnS–silica NPCs are ideal candidates for enhancing the fluorescence (approximately 10 times), approximately 6 times higher than that of silica NPC.

2.3.5 Opto-thermoelectric and DNA self-assembly. Nonclosely packed metal micro and nanostructures will generate plasmonic resonance and are widely used for plasmonic sensing, surface enhanced Raman scattering, photovoltaic devices, and circular dichroism.[169] The resonant responses of such NPCs rely on the orders of the position and orientation and density of the particles, which can be manipulated by the self-assembly, such as opto-thermoelectric and DNA self-assembly. For instance, Zheng's group developed an opto-thermoelectric nanotweezers technique with low power to manipulate the diverse sizes and shapes of metal nanoparticles by optically heating a thermal-plasmonic substrate (Fig. 7a–c).[170] The spatial separation of dissolved ions in the heated laser spot creates the light-directed thermoelectric field that allows opto-thermoelectric nanotweezers to manipulate the transfer and assembly of a single particle to form the desired structures. An alternative approach to construct complex plasmonic metamaterials is DNA self-assembly. Kuzyk *et al.* fabricated the reconfigurable 3D plasmonic metamolecules *via* DNA self-assembly, which can execute DNA-regulated conformational changes at the nanoscale.[171] As shown in Fig. 7d and e, two gold nanorods (AuNRs) are hosted on a reconfigurable DNA template and excite the plasmons due to the proximity. The two crossed AuNRs constitute a 3D plasmonic chiral object that can convert its *in situ* conformational changes into circular dichroism changes in the visible wavelength range. Based on the combination of lithographic techniques with DNA self-assembly, Litt *et al.* developed a responsive plasmonic metamaterial that can precisely control the intensity of the electromagnetically-induced transparency-like effect (Fig. 7f).[172] The conformation of the DNA linkers is sensitive to the external stimuli (such as NaCl concentration),

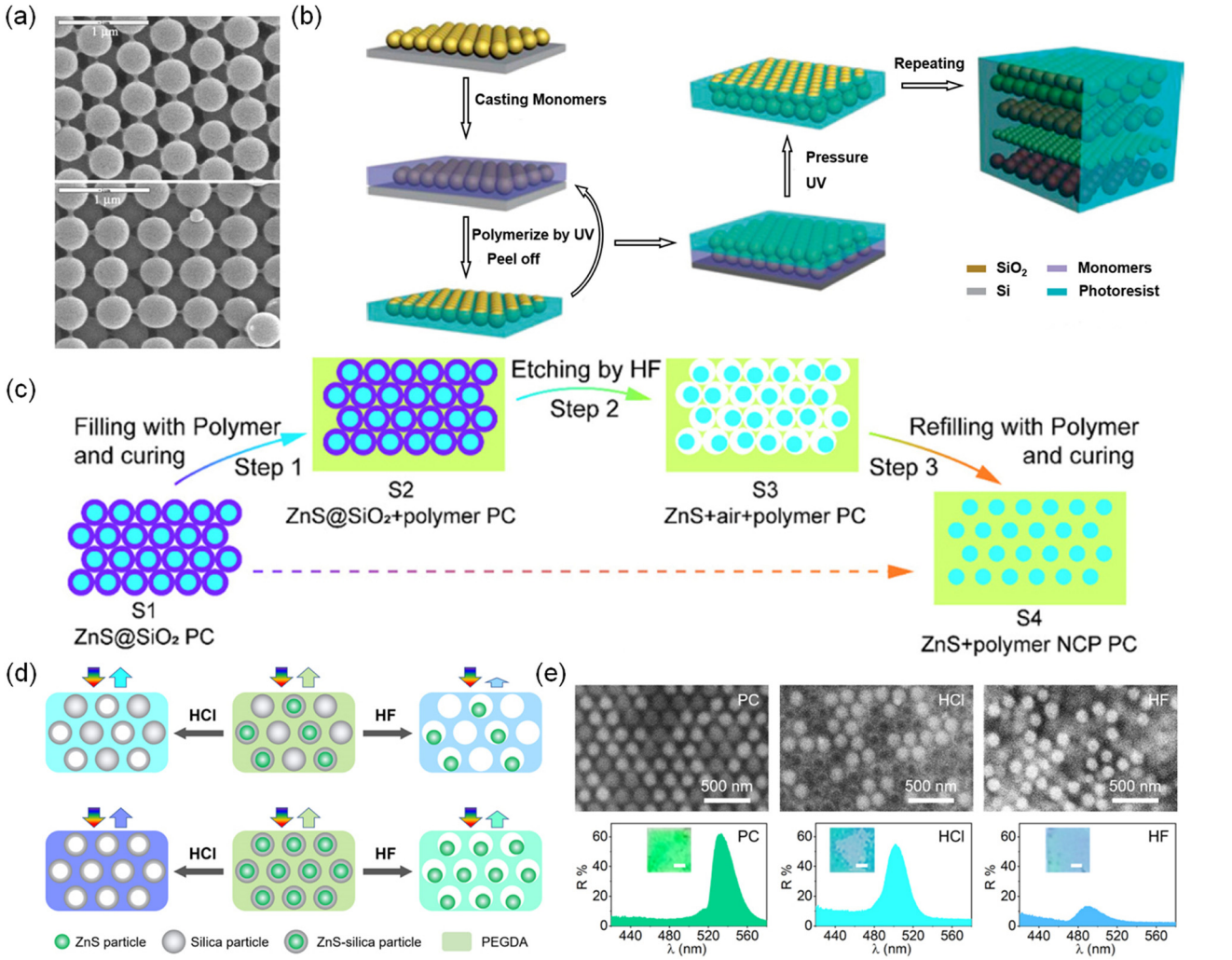

Fig. 6 (a) (111) and (100) faces were observed on the outer surface of an opal after sintering at 960 °C, followed by acid etching for 20 min. Reproduced with permission.[141] Copyright 2003, Wiley-VCH. (b) Schematic illustration of the procedure used to fabricate 3D NPC colloidal crystals with tunable sphere interstices *via* the LBLP technology. Reproduced with permission.[167] Copyright 2008, The Royal Society of Chemistry. (c) Schematic illustration of the scenario based on the two-step filling strategy. The cyan circles represent ZnS nanospheres, the purple rings represent parts of the silica shell, the cyan blocks represent the filled PEGDA-based polymers, and the white areas represent the air. Reproduced with permission.[133] Copyright 2021, American Chemical Society. (d) Schematic illustration of the fabrication of the derived photonic superstructures. (e) SEM images and reflection spectra and photos of the ZnS–silica/silica PC, corresponding HCl etched PC, and HF etched PC. Reproduced with permission.[168] Copyright 2023, Wiley-VCH.

resulting in the coupling distance between the DNA-linked nanorods and the resonant strength that can be modulated.

3. Functionalities of NPCs

NPCs with smart functionalities can change their reflection signals and structural colors through variations in order degree, orientation, refractive index, or lattice distance in response to physical or chemical stimuli. The smart functionalities are realized using responsive building blocks and matrices.[173,174] For example, magnetic field-responsive 1D NPCs can be prepared through the self-assembly of superparamagnetic colloidal particles in water.[78] These 1D NPCs will alter their colors and reflection wavelengths in response to different magnetic field strengths due to the unique capability of nonclosely packed structures with adjustable d_{s-s}. Another well-known example is mechanochromic 3D NPCs, inspired by the dynamic nonclosely packed structures from chameleon skins, which were fabricated by fixing nonclosely packed structures into elastic polymers. External forces-induced deformation will cause a change in the color of mechanochromic 3D NPCs owing to their specific deformable lattices. By a rational combination of responsive building blocks and matrices, a variety of smart NPCs with mechanochromic, thermochromic, magnetochromic, electrochromic, chemical-chromic, and biochromic functions have been fabricated.

3.1 Mechanochromic NPCs

Due to the nonclosely packed structures, mechanochromic NPCs are capable of modulating their reflection wavelengths

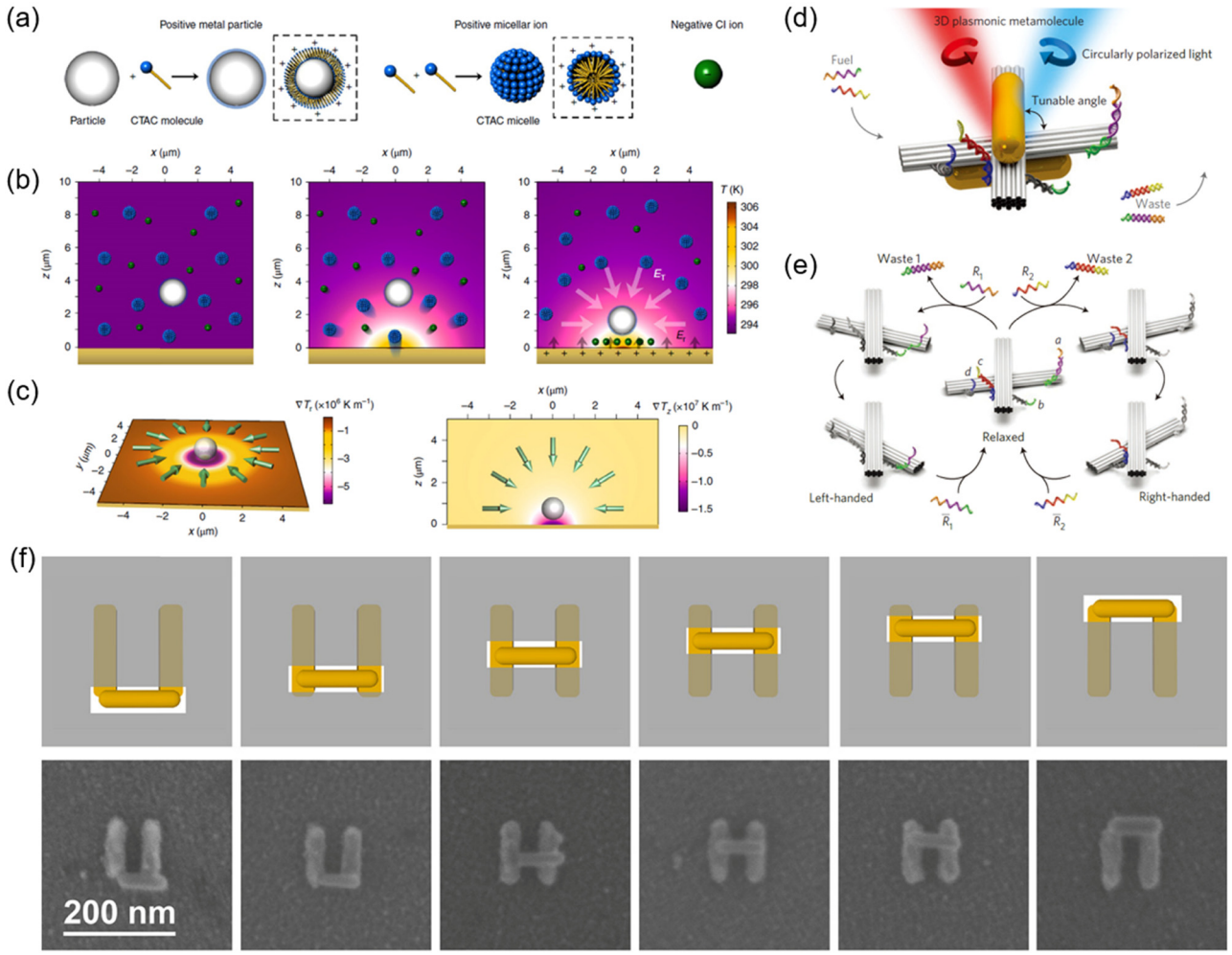

Fig. 7 (a) Surface charge modification of a metal nanoparticle by CTAC adsorption. Formation of CTAC micelles. Schematic view of a Cl^- ion. (b) Dispersion of a single metal particle and multiple ions in the solution without optical heating. Thermophoretic migration of the ions under optical heating. Steady ionic distribution under optical heating generates a thermoelectric field E_T for trapping the metal nanoparticle. (c) Simulated in-plane temperature gradient ∇T_r and direction of the corresponding trapping force. Simulated out-of-plane temperature gradient ∇T_z and direction of the corresponding trapping force. Reproduced with permission.[170] Copyright 2018, Springer Nature. (d) Schematic diagram. Two gold nanorods (AuNRs) are hosted on a switchable DNA origami template consisting of two connected bundles, which subtends a tunable angle. (e) Switching mechanism. The four arms of the two DNA locks are labelled a, b, c, and d. Reproduced with permission.[171] Copyright 2014, Springer Nature. (f) Symmetry control of inorganic–organic hybrid EIT-like structures. Reproduced with permission.[172] Copyright 2018, American Chemical Society.

and structural colors in response to external forces or strain by varying their lattice distances.[154,175–190] For practical usage, a superior mechanochromic NPC should possess a large tuning range of reflection wavelength ($\Delta\lambda$), high sensitivity, fast responsive speed, excellent reversibility, and outstanding stability. The sensitivity of mechanochromic NPCs is characterized by S_s ($\Delta\lambda/\Delta\varepsilon$, nm/%) and S_p ($\Delta\lambda/P$, nm kPa^{-1}), the change of maxima reflection wavelength relative to the mechanical strain and pressure, respectively. Apparently, a larger d_{s-s} inversely proportional to the volume fraction of particles will leave more space for deformation, thereby significantly increasing the $\Delta\lambda$, sensitivity, and responsiveness. On the other hand, a higher content of the elastic matrix will endow MPCs with better reversibility and smaller stress during deformation. Therefore, nonclosely packed structures, a large d_{s-s}, and a high-content elastic matrix are important and urgently desired for outstanding mechanochromic NPCs.

3.1.1 Mechanochromic NPC hydrogels. The fabrication strategies for mechanochromic NPCs include electrostatic self-assembly,[123,149,191] swelling the closely packed structures,[137,180,192] dialysis-based assembly,[175,180] magnetically induced assembly,[80,178,193–196] and shear-induced assembly.[162,179,197] In 1994, Asher *et al.* first reported the fabrication of mechanochromic NPCs by the electrostatic self-assembly of PS particles into *N*-vinylpyrrolidone and methyl acrylate (MA) monomer, followed by polymerization.[123] The mechanochromic NPC shows a small $\Delta\lambda$ (35 nm) under a uniaxial strain. Fudouzi *et al.* obtained PS/PDMS NPC elastomers by filling pre-cured PDMS elastomers into the gaps of close-packed PS colloidal crystal arrays and then swelling the PDMS network with silicone oil

(Fig. 8a).[137] Unfortunately, the low volume fraction of PDMS (26%) of closely packed structures leads to a small d_{s-s} and limited $\Delta\lambda$ of 30 nm and S_s of 1.50 nm/%, respectively. A low volume fraction of building blocks and a high-volume fraction

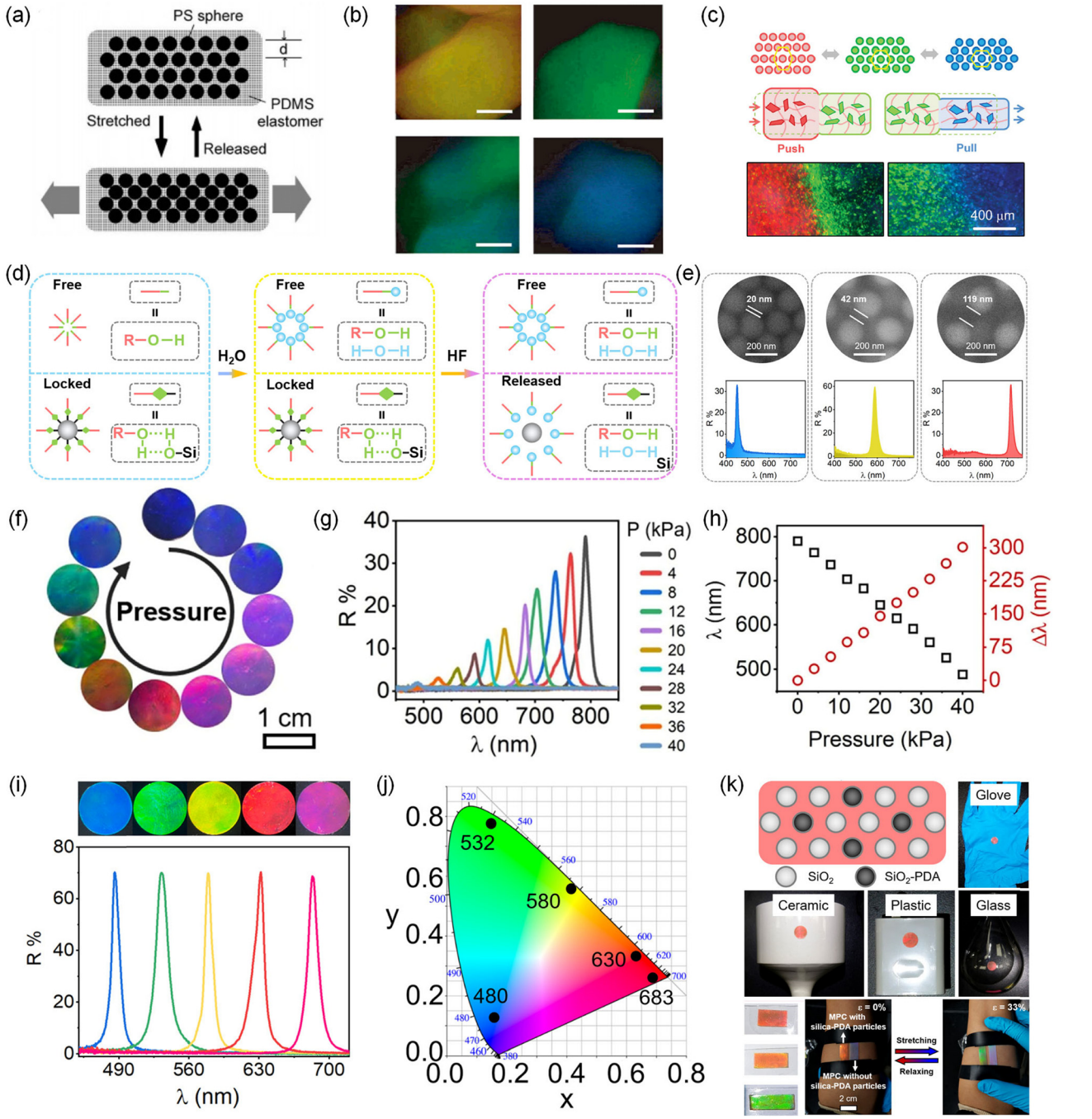

Fig. 8 (a) Schematic illustration of the reversible tuning lattice distance. Reproduced with permission.[137] Copyright 2006, American Chemical Society. (b) Reflection microscope images of single grains in the gelled photonic crystal under compression. Reproduced with permission.[175] Copyright 2003, American Chemical Society. (c) Optical microscope images of mechanochromic photonic crystals and illustration of their structural change under deformation. Reproduced with permission.[199] Copyright 2014, Wiley-VCH. (d) Schematic illustration of the locking and releasing of hydrogen bonds between HEA and silica. (e) SEM images, reflection spectra, and microscope images of PC, PCG, and MPC, respectively. Reproduced with permission.[200] Copyright 2023, Elsevier. (f) Digital photos and (g) reflection spectra of MPC under different pressures. (h) The reflection wavelength and shift of reflection wavelength of MPC as a function of pressure. Reproduced with permission.[156] Copyright 2022, Elsevier. (i) Digital photographs, corresponding reflection spectra, and (j) CIE coordination of MPSs prepared by silica particles with sizes of 142, 153, 166, 178, and 197 nm. Reproduced with permission.[201] Copyright 2022, American Chemical Society. (k) Schematic illustration of the structure of MPC and digital photos of the as-fabricated MPCs with silica-PDA particles on substrates with different materials and colors. Reproduced with permission.[203] Copyright 2022, Wiley-VCH.

of elastic or soft matrix are favorable for improving $\Delta\lambda$ and S_s of NPCs.[198] Sensitive NPC hydrogels reported by Yamanaka *et al.*[175] were achieved by embedding nonclosely packed PS colloidal crystals into a poly(acrylamide) gel matrix based on a dialysis process. Due to the high-volume fraction of the hydrogel (96.7%), the NPC hydrogel possesses a large $\Delta\lambda$ of 350 nm (810 to 460 nm) and a large S_s of 7.95 nm/% by compression (Fig. 8b). By combining swelling and dialysis processes, Hong *et al.* also prepared highly mechanochromic NPC hydrogels showing a large $\Delta\lambda$ of 460 nm and S_P of 36 nm kPa^{-1} under a 12.7 kPa stress.[180] However, these NPC hydrogels require a time-consuming dialysis process and easily lose their mechanochromic properties under dry conditions, which limits their practical applications.

3.1.2 Mechanochromic NPC organic gels. Compared to hydrogels, mechanochromic NPCs organic gels show better stability. For example, Ge *et al.* fabricated mechanochromic photonic gels by the self-assembly of silica colloidal crystal arrays in a mixture of ethylene glycol (EG) and polyethylene glycol methacrylate (PEGMA) through photopolymerization (Fig. 8c).[199] Due to the high boiling point of EG, the mechanochromic photonic gel can be stored for at least 20 days without losing its large $\Delta\lambda$ (150 nm), high S_p (0.7 nm kPa^{-1}), S_s (3.16 nm kPa^{-1}), and fast response speed (0.7 nm ms^{-1}). Mechanochromic NPC with excellent stability that can mimic chameleon skin[4] was fabricated by Kim's group based on the self-assembly of silica particles in PEGPEA.[153] The mechanochromic NPCs not only exhibit long-term stability (>180 days) due to their nonvolatility but also show color change from red to blue corresponding to the strain from 0 to 68%. Nevertheless, their $\Delta\lambda$ and S_s are limited to 133 nm and 1.93 nm/%, respectively, due to their insufficient d_{s-s}.

3.1.3 Mechanochromic NPC films. It is still a big challenge to fabricate mechanochromic NPCs with broad $\Delta\lambda$, large S_s or S_p, fast responsiveness, outstanding stability, and good reversibility. Recently, our group developed a simple and efficient method to significantly improve the d_{s-s} for fabricating mechanochromic NPCs with ultrahigh sensitivity (106.9 nm kPa^{-1}, 3.7 nm/% by stretching, and 7.6 nm/% by pressing) fast response speed (11.3 nm ms^{-1}), broad $\Delta\lambda$ (340 nm), and good reversibility (>100 times) by the two-step swelling of nonclosely packed structures.[200] The extremely sensitive SiO_2/H_2O-hydroxyethyl acrylate (HEA) mechanochromic NPCs with large d_{s-s} in this work were fabricated by swelling the nonclosely packed structure combined with a unique interface etching-induced swelling mechanism (Fig. 8d). This strategy can precisely and efficiently increase the d_{s-s}, displaying a maximum enhancement factor that is 12 times higher than that of photonic crystals, which is crucial for outstanding mechanochromic performances (Fig. 8e). Based on the high sensitivity and fast responsiveness of mechanochromic NPC, it can dynamically, instantly, and visually monitor the relatively low jumping pressure of small frogs and the distribution of pressure in each toe, which is helpful to understand the jumping behavior of frogs. For balancing the high sensitivity and long-term stability of mechanochromic NPCs, we fabricated extremely sensitive mechanochromic NPCs by nonclose-assembling silica particles (15% vt) into DEGEEA (85% vt) (Fig. 8f–h).[156] Compared to other NPCs, the as-fabricated NPCs possess super-large d_{s-s} (156–258 nm) due to the low crystallization threshold of silica in DEGEEA (7–9%). Therefore, the NPCs exhibit extraordinary mechanochromic performances, involving a large $\Delta\lambda$ (362 nm), high S_P (7.55 nm kPa^{-1}), fast responsiveness (7.0 nm ms^{-1}), excellent stability (>2 months), and good reversibility (>1000 cycles). Nevertheless, because of the matching of refractive index ($\Delta n \approx 0.01$) between silica particles and the DEGEEA, the reflectance of the NPCs is low (30–40%), which may restrict their practical applications. To address this issue, we developed a refractive index mismatching strategy to prepare mechanochromic NPCs with high reflectance (70%) and brilliant colors by the self-assembly of silica particles into acrylates with large refractive indexes (Fig. 8i and j).[201] The mechanochromic NPC has a large maximal ($\Delta\lambda$ = 205 nm) and S (3.68 nm/%) due to the large d_{s-s} (77 nm) and exhibits bright structural colors owing to their high reflectance (70%) during stretching processes.

Like other PCs, mechanochromic NPCs also show substrate-dependent colors, which is not favorable in reality. Generally, NPCs exhibit bright reflective colors on black substrates but dull, complex, or white colors on substrates with different colors due to the incoherent scattering of light from both NPCs and substrates (Fig. 8k).[202] To suppress the incoherent scattering of light, black particles such as carbon and Fe_3O_4 particles are usually introduced into the PCs. However, the co-assembly of black particles and building blocks may break their long-range order and lead to nonuniform colors due to the different sizes and surface properties between them. We prepared MPCs with substrate-independent bright structural colors, long-range order, and excellent mechanochromic properties based on the co-assembly of the same size silica and silica-polydopamine (PDA) in acrylates.[203] The silica-PDA effectively absorbs the incoherent scattering of light without interrupting the order degree of NPCs. As a result, the NPCs show vivid mechanochromic colors even on a white background, which is exceedingly difficult for other mechanochromic NPCs.

3.2 Thermochromic NPCs

Most thermochromic NPCs capable of constantly switching the reflected signal were prepared based on the combination of the thermally responsive PNIPAM and its derivatives.[124,125,204–211] PNIPAM has a low critical dissolution temperature of PNIPAM (LCST: ~32 °C). When the temperature is below the LCST, the NIPAM-based PC hydrogels are hydrophilic and can absorb water into the polymer network. In contrast, as the temperature is higher than the LCST, it becomes hydrophobic, leading to the expulsion of water molecules and shrinkage of volume. Therefore, PNIPAM-based NPCs can change their reflection wavelengths and reflectance in response to temperature when PNIPAM serves as either a building block or a matrix. The thermochromic performances are typically characterized by the range of tunable wavelength ($\Delta\lambda$) and reflectance (ΔR%), temperature sensing range (ΔT), and sensitivity.

3.2.1 Thermochromic NPCs based on variable d_{s-s}. The first thermochromic NPC hydrogel, first reported by Asher *et al.*, was prepared by embedding PS colloidal crystals into PNIPAM hydrogels (Fig. 9a).[124] As the temperature increased from 10 to 35 °C (ΔT = 25 °C), the lattice distance of the NPC gels decreased, resulting in a blue shift of the reflection wavelength from 704 to 460 nm, almost covering the entire visible range ($\Delta\lambda$ = 244 nm). The nonclosely packed structure should be attributed to the high sensitivity and large $\Delta\lambda$. Meanwhile, they also prepared another type of thermochromic NPCs using PNIPAM particles as building blocks. Unlike the previous one, this NPC changes its reflection intensity rather than wavelength due to the temperature-dependent scattering efficiency of the NIPAM particles. By combining the inverse opal template and PNIPAM, Watanabe *et al.* developed two types of thermochromic PC hydrogels by interconnecting and trapping gel particle arrays (Fig. 9b).[212] One type of thermochromic photonic hydrogel was fabricated by soaking the inverse opal template with interconnecting porous structure in the pre-gel NIPA solution and then polymerizing and removing the template. The wavelength changes at different temperatures due to the variation in their lattice distances. The fabrication of another type of thermochromic photonic hydrogel is similar to the above steps except for retaining the template to make each PNIPAM particle movable in the inverse opal structure. Such a unique structure allows the gradual breaking of long-range order of colloidal arrays by increasing temperature due to the random distribution of collapsed PNIPAM gel particles. Thus, its reflectance decreases as the temperature increases. Unfortunately, the ordered structure of the microgel colloidal crystals is fragile. To address this problem, Zhang's group developed a co-polymerization strategy to fabricate NIPAM-HEMA microgels and assemble them into thermochromic NPC hydrogels.[206] As shown in Fig. 9c, these thermochromic samples possess not only a large $\Delta\lambda$ of 298 nm but also good mechanical resistance. For NIPAM-based NPC hydrogels, the major drawback is that their ΔT are usually smaller than 30 °C due to the narrow response window of NIPAM. In addition, these thermochromic NPCs may change their peak positions when they are deformed, which is inconvenient in practical applications.

3.2.2 Thermochromic NPCs based on variable Δn. Our group recently reported a new type of liquid, transparent, and antideformable thermochromic NPC that can sense much larger ΔT based on a unique mechanism. This new thermochromic NPC was prepared by nonclosely assembling silica particles into the mixture of ethanol and PEGDA as the matrix. Due to the matching of the refractive index (Δn = 0), this NPC shows high transparency at room temperature (Fig. 9d).[213] When the temperature increases, the refractive index of silica

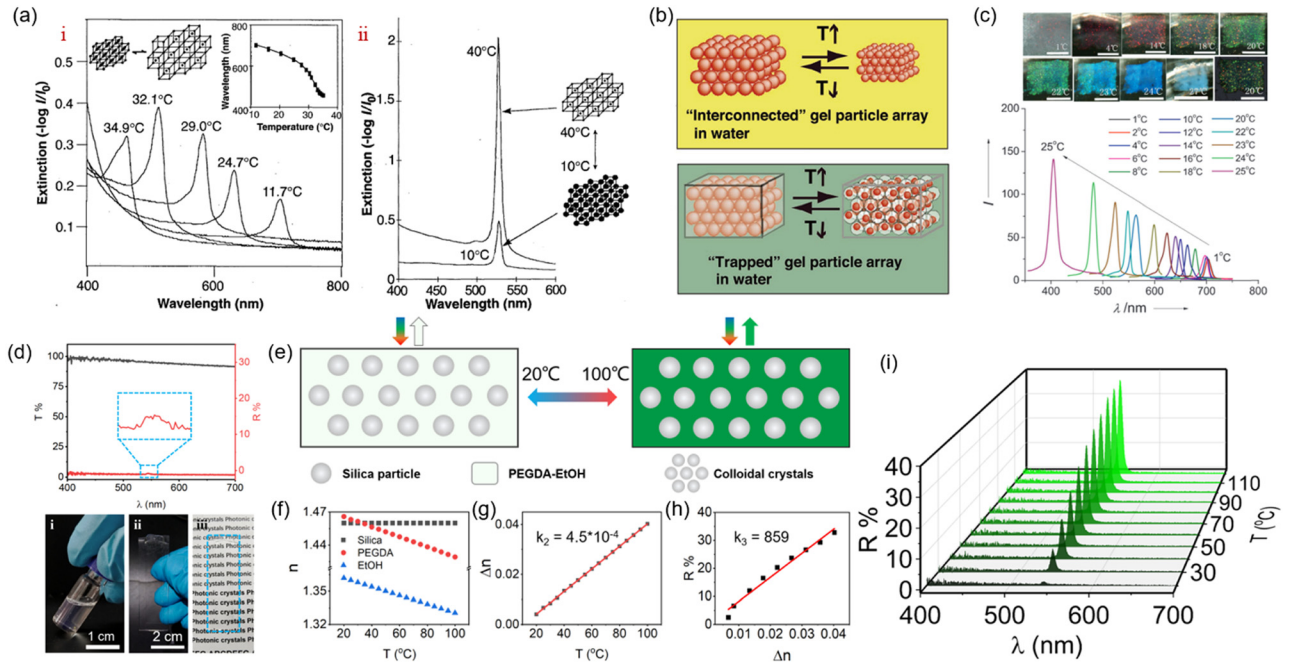

Fig. 9 (a) Temperature tuning of Bragg diffraction from a 125 μm-thick PCCA film of 99 nm PS spheres embedded in a PNIPAM gel and diffraction from a CCA of PNIPAM spheres at 10 and 40 °C. Reproduced with permission.[124] Copyright 1996, American Association for the Advancement of Science. (b) Preparation of an "interconnected" gel particle array and a "trapped" gel particle array using a closest-packing silica colloidal crystal as a template. Reproduced with permission.[212] Copyright 2006, American Chemical Society. (c) Photographs of a freestanding PMCC film taken when the temperature rises from 1 to 27 °C and reflection spectra of the PMCC film measured at various temperatures. Reproduced with permission.[206] Copyright 2013, Wiley-VCH. (d) Digital photos of the TPC filled into a bottle and PDMS mold at 20 °C and the reflection and transmittance spectra of the TPC. (e) Schematic illustration of the variation of structural color of the TPC at 20 and 100 °C. (f) The refractive index of silica, PEGDA, and EtOH as a function of temperature. (g) The Δn of the TPC is a function of temperature. (h) The reflectance of the TPC as a function of Δn. (i) Reflection spectra of the TPC at diverse temperatures (20–120 °C). Reproduced with permission.[213] Copyright 2022, Wiley-VCH.

is constant, while that of the liquid part decreases (Fig. 9e and f), leading to an increase in Δn and thus the reflectance (Fig. 9g and h). Interestingly, it is found that reflectance is linearly proportional to temperature (Fig. 9i). Compared with other thermochromic NPCs, it shows (1) a unique "off/on" characteristic at refractive index matching/mismatching state; (2) robust, shapeable, and antideformable properties; and (3) excellent thermochromic performances, including a large ΔT (80 °C), high sensitivity (0.46% $°C^{-1}$), fast response speed ($\approx$4.75% s^{-1}), and good reversibility (>30 times). This work provides a general principle for constructing sensitive thermochromic NPCs and enriches the understanding of the thermochromic mechanism.

Unlike the above thermochromic NPCs that can continuously modulate their reflected signals with temperature, Wang *et al.* developed a kind of thermochromic NPC by integrating NPC and heat-sensitive pigments.[214] The thermochromic NPCs can reversibly change their mixed colors at the specific phase change temperature.

3.3 Magnetochromic NPCs

In the magnetochromic NPC system, where superparamagnetic colloidal particles are dispersed in solvents, their lattice distance and orientation can be tuned by the magnetic field, leading to the variation of their reflection signals.[88,195,215–223] Specifically, the nonclosely packed structure is essential to such unique functions.

3.3.1 Adjustable structural color by magnetic field intensity. For instance, Asher *et al.* synthesized PS microspheres containing superparamagnetic nanoparticles and prepared magnetochromic NPCs by the electrostatic self-assembly of these particles.[81] As shown in Fig. 10a, the wavelength blueshifts from 560 to 428 nm ($\Delta\lambda$ = 132 nm) when the magnetic field gradient increases from 1.5 to 5.4 kOe cm^{-1}. Due to the low content of magnetic material in the colloidal particles, the magnetochromic NPCs show a limited wavelength shift, long response times, and consequently limited practical applications. Yin *et al.* reported sensitive magnetochromic NPCs by the self-assembly of superparamagnetic Fe_3O_4 colloidal nanocrystal clusters (CNCs) in water. These magnetochromic NPCs shift a broad $\Delta\lambda$ (> 300 nm) in a short time (<1 s) as the applied magnetic field increases from 87.8 to 352 G due to the extremely low content of superparamagnetic colloidal particles (<1%).[78] However, these magnetochromic NPCs suffer from instability under the large gradients of the magnetic field. Hu *et al.* reported a strategy to stabilize magnetochromic NPCs against packing forces exerted by magnetic fields using agarose hydrogels as polymer matrices.[217] The steric hindrance and

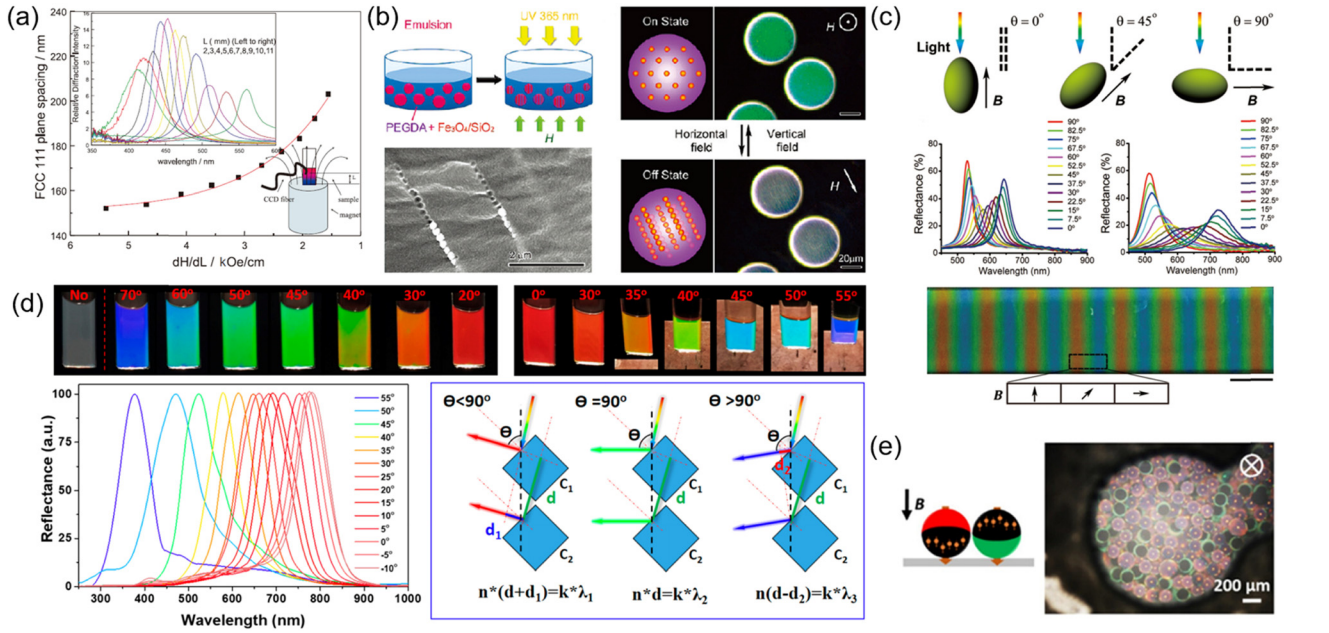

Fig. 10 (a) Influence of the average magnetic field gradient d*H*/d*L* on the lattice constant of a thick CCA composed of 134 nm superparamagnetic particles in deionized water. Reproduced with permission.[81] Copyright 2001, Wiley-VCH. (b) Synthetic procedures for the magnetochromatic microspheres, SEM images of Fe_3O_4@SiO_2 particle chains embedded in a PEGDA matrix, schematic illustrations, and optical microscopy images for the magnetochromatic effect caused by rotating the chain-like photonic structures in magnetic fields. Reproduced with permission.[215] Copyright 2009, American Chemical Society. (c) Schematic representation of the spontaneous alignment of nanoellipsoids under magnetic fields, reflection spectra of photonic structures under magnetic fields with varying directions with respect to the direction of light, and digital photo showing the photonic response of NE-B encapsulated in a flat glass tube under a nonideal linear Halbach array. Reproduced with permission.[226] Copyright 2015, Wiley-VCH. (d) Optical images of a colloidal dispersion of Fe_3O_4@SiO_2 nanocubes in a capillary without and with a magnetic field under different viewing angles (left) and directions (β) of magnetic fields (right). The corresponding normalized reflection spectra were measured by varying the directions of the external magnetic field and qualitative ray-optic model predicting the difference of the light pathway. Reproduced with permission.[228] Copyright 2019, American Chemical Society. (e) OM images show a round tip of the chameleon tail under the upward (top) field. Reproduced with permission.[235] Copyright 2020, American Chemical Society.

hydrogen bonding of the agarose hydrogel network is the key to restricting the migration of Fe_3O_4@SiO_2 particles and stabilizing the magnetochromic NPCs under large gradients of the magnetic field.

3.3.2 Adjustable structural color by magnetic field intensity direction. The hiding-showing switch of the structural color of 1D magnetochromic NPCs can be regulated by the magnetic field direction due to the orientation of 1D magnetochromic NPCs tending to align along the orientation of the magnetic field direction.[224–226] For example, Ge *et al.* prepared magnetochromic microspheres by self-assembling Fe_3O_4@SiO_2 particles in a photocurable resin to fix the ordered structure through photopolymerization (Fig. 10b).[215] The nanochains comprised of Fe_3O_4@SiO_2 particles tend to align along the magnetic field so that the photonic microspheres will rotate as the magnetic field direction changes, changing the direction of the lattice relative to the incident light and thus controlling the structural color of the photonic microspheres. Except for the isotropic magnetic colloidal particles, the introduction of anisotropic magnetic colloidal particles as the building blocks can obtain abundant structural colors related to the magnetic field orientation due to the anisotropic building blocks that favor complicated photonic structures.[130,226–229]

For example, Yin's group reported that the magnetochromic NPCs formed by the self-assembly of ellipsoidal colloidal particles with anisotropic morphology and magnetic properties strongly depend on the magnetic field orientation for their structural color (Fig. 10c).[226] The reflection wavelength is minimized when the magnetic field direction is perpendicular to the angle of incidence and maximized when the magnetic field direction is parallel to the angle of incidence ($\Delta\lambda \approx$ 200 nm, 0–90°). The reflectance reaches the maximum when the magnetic field direction is perpendicular or parallel to the incident angle and decreases gradually as the magnetic field direction deviates from the angle. Similarly, their group used Fe_3O_4@SiO_2 nanocubes as building blocks and assembled them into one-dimensional magnetochromic NPCs in an edge-to-edge manner by a magnetic field.[228] This unique assembly behavior is driven by the minimization of the competing dipole–dipole and Zeeman coupling energies from the shape anisotropy and allows wavelength and structural colors over the entire visible range ($\Delta\lambda \approx$ 400 nm) by magnetochromic NPCs to be tuned by varying the magnetic field orientation (−10°–55°). In addition, due to their cube shape, they can display bright structural colors at wide viewing angles (Fig. 10d).

3.3.3 Magnetochromic NPCs with nonmagnetic colloidal particles. Besides the magnetic building blocks, magnetochromic NPCs with nonmagnetic colloidal particles as building blocks can rapidly and reversibly respond to the magnetic field, and their reflectance can be tuned by magnetic fields to enable the on/off switching of structural colors.[158,230] Ge *et al.* reported that PS particles self-assemble into magnetochromic NPCs in a ferrofluid.[230] PS particles can be reversibly assembled into NPCs under a magnetic field due to the dipole–dipole interactions of "magnetic holes". However, the low reflectance (<15%) of magnetochromic NPCs may restrict their applications. The construction of anisotropic Janus balls with magnetic and NPCs properties can be realized with magnetochromic NPCs with high reflectance and brilliant structural colors.[231–234] Kim *et al.* prepared programmable structured color-switched magnetochromic NPCs with controllable magnetic moments by combining magnetic materials with NPCs by microfluidic techniques (Fig. 10e).[235] The magnetic moments are distributed by applying an external magnetic field and fixed by light curing. The silica in the heavier compartments spontaneously forms NPCs under repulsive forces, producing a structural color. In the absence of a magnetic field, the magnetochromic NPCs filled with carbon black compartments face upward and appear black; in the presence of an external magnetic field, the magnetochromic NPCs align their magnetic moments with the magnetic field and display the structural color. These magnetochromic NPCs with the advantage of bright structural colors can be fabricated on a large scale. Unfortunately, they exhibit indistinguishable structural colors at a wide viewing angle due to their Janus structure.

3.4 Electrochromic NPCs

Most electrochromic NPCs were prepared based on the self-assembly of highly charged colloidal particles in a low-viscosity liquid medium.[236–241] Their reflection peaks and structural colors can be precisely modulated by voltage. When they are exposed to an electric field, charged particles move to oppositely charged electrodes resulting from the electrophoretic motions. This leads to the can shrinkage of lattice distance and, thus the blueshift of the reflection wavelength. Upon removal of the electric field, the colloidal particles and the reflection wavelength return to their original state.

3.4.1 Adjustable structural color and saturation. For example, Yang *et al.* first reported that electrochromic NPCs with fast response and low voltage self-assembled by nonclosely packed PS particles (Fig. 11a).[236] In the absence of an electric field, the colloidal particles with a volume fraction of 22% were self-assembled into NPCs with a reflection peak at 605 nm and red structural color due to electrostatic repulsion. Once an electric field was applied (−1.8 V), the negatively charged silica particles were subjected to coulombic forces and migrated to the anode, leading to a blueshift of the reflection peak from 605 to 500 nm ($\Delta\lambda$ = 105 nm, Fig. 11b). However, the limited tuning range of structural colors may restrict their electrochromic properties. Chen *et al.* reported sensitive electrochromic NPCs by the self-assembly of silica in a mixture of propylene carbonate and ETPTA.[242] Due to the low volume fraction of silica (20%) and the conductive environment offered by propylene carbonate, the NPCs display a large tuning range of reflection wavelengths ($\Delta\lambda$ = 208 nm, from 620 to 412 nm) under a voltage of 3.3 V (Fig. 11c).

Except for the color tunability, the color saturation of electrochromic NPCs requires extra attention, which is crucial to practical application. SiO_2 or PS-based electrochromic NPCs show unsatisfactory reflectance and dim colors due to the small Δn between the particles and solvents. One can enhance the

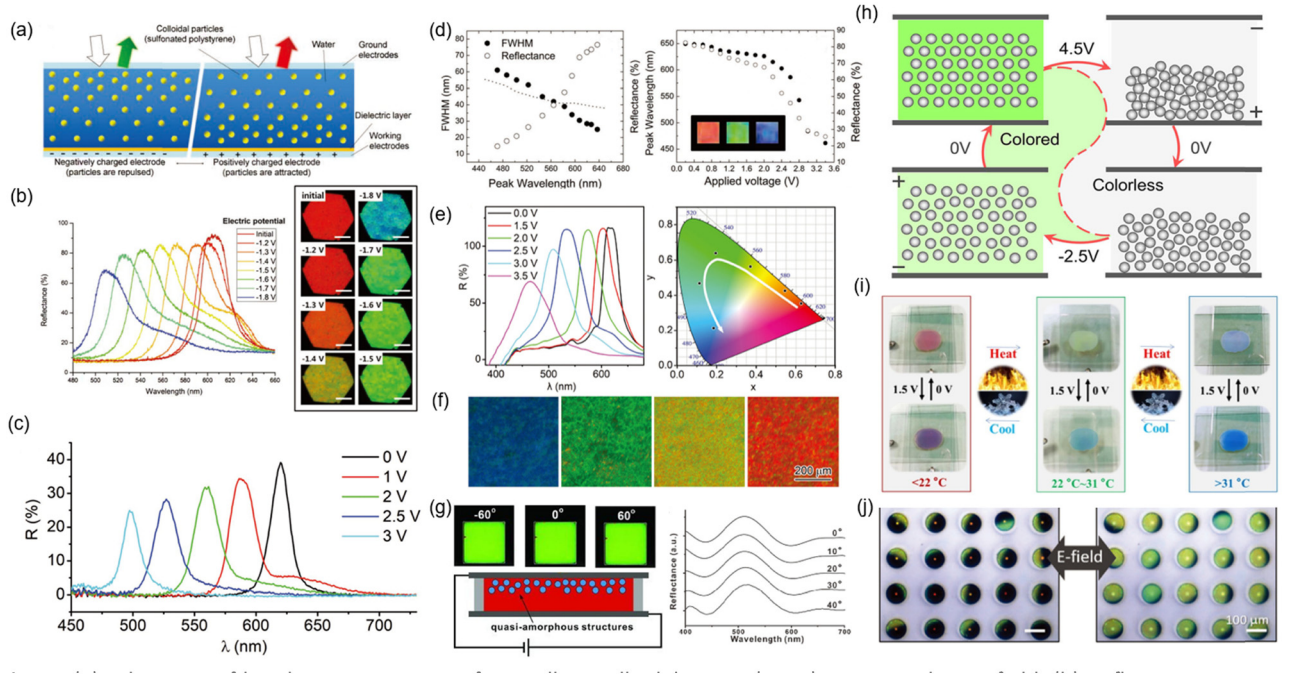

Fig. 11 (a) Schematic of bandgap engineering of crystalline colloidal arrays (CCAs) using an electric field. (b) Reflectance spectra of CCAs and the corresponding optical microscope images for various magnitudes of the DC electric field. Reproduced with permission.[236] Copyright 2010, Wiley-VCH. (c) Blueshift of the reflection peak for photonic crystal E-ink with the increase in the electric field. Reproduced with permission.[242] Copyright 2017, Wiley-VCH. (d) The peak reflectance and the peak FWHM as a function of the peak wavelength. The simulated value of FWHM is included as a reference (dotted line). Relationship between applied voltage *vs.* reflectance (○) and peak position (●). Reproduced with permission.[243] Copyright 2012, Wiley-VCH. (e) Reflection spectra of CeO_2@SiO_2/propylene-carbonate liquid PC in different electric fields. CIE chromaticity diagram showing the color changes in a different electric field. (f) Optical microscope images for liquid PC at 3.5, 2.5, 2.0, and 0 V, respectively. Reproduced with permission.[131] Copyright 2018, Wiley-VCH. (g) Schematic structure of photonic display pixel, photographs were taken at 2.5 V, and the reflection spectra of a photonic display pixel exhibiting green color at 3 V. Reproduced with permission.[10] Copyright 2010, Wiley-VCH. (h) Structural change of the SiO_2/PCb-PEG-EGERPC (30/60/5/5 vol%) as it was switched between the colored state and the colorless state by an electric field. Reproduced with permission.[245] Copyright 2022, Springer Nature. (i) Digital photos of the display unit at different temperatures and voltages. Reproduced with permission.[246] Copyright 2022, Elsevier. (j) OM images show a collective change in the orientation of Janus microspheres in a square array under an alternating current electric field, where the plasmonic faces (left) and photonic faces (right) are alternately up. Reproduced with permission.[248] Copyright 2022, Wiley-VCH.

color saturation and reflectance of electrochromic NPCs by a large Δn using high refractive index materials as building blocks. To date, colloidal particles with high refractive indexes (n) such as Cu_2O (n = 2.7), CdS (n = 2.52), ZnS (n = 2.35), CeO_2 (n = 2.2), and Fe_3O_4 (n = 2.42) have been fabricated. However, most of them are not ideal candidates for preparing electrochromic NPCs due to the lack of strong surface charge and the intense light absorption by these materials. Han *et al.* successfully prepared highly charged ZnS@SiO_2 particles (−48 mV) by coating silica on the surface of ZnS particles and self-assembled them into NPCs in deionized water.[243] Due to the high surface potential and high refractive index of ZnS@SiO_2 particles, ZnS@SiO_2 NPCs show brilliant colors (reflectance: ~90%) even with a low volume fraction (5.4%). The large particle spacing enables the NPCs to shift the reflection wavelength from 650 to 450 nm ($\Delta\lambda$ = 200 nm) at a voltage of 3.2 V (Fig. 11d). Similarly, Fu *et al.* synthesized CeO_2@SiO_2 colloidal particles and assembled them in a propylene carbonate solution to prepare electrochromic NPCs.[131] As shown in Fig. 11e and f, the large Δn between CeO_2@SiO_2 particles and propylene carbonate renders NPCs with a wide photonic band gap, high reflectance (>90%), and highly saturated structural colors. Compared to electrochromic NPCs with a crystalline structure, electrochromic NPCs with amorphous structures show greater potential in display applications due to their angle-independent structural colors. Kang *et al.* reported electrochromic NPCs with angle-independent structural colors prepared by a moderate polydispersity of Fe_3O_4@SiO_2.[10] The electrochromic NPCs display a large $\Delta\lambda$ (165 nm) due to their low concentrations of Fe_3O_4@SiO_2 (25 wt%) under a voltage of 4 V. In addition, the polydispersity of the particles was regulated to be moderately high (δ_{core} = 14%, $\delta_{core+shell}$ = 9%) to inhibit the crystalline nature; thus, their structural colors are angle-independent (Fig. 11g).

3.4.2 Low-power electrochromic NPCs. In addition, the low power consumption of electrochromic NPCs is highly desired and important in practical applications. Recently, Ge's group developed low-power electrochromic NPCs based on weak-polar and bistable-state colloidal systems.[244,245] The weak-polar electrochromic NPCs were prepared by hydrophobic SiO_2 particles, 1,2-dichlorobenzene (DCB), and dioctyl sulfosuccinate sodium salt (AOT) as reversed micelles. The weak-polar solvent DCB

acts as a dielectric medium with less screening effect, thus achieving strong coulombic interactions between the particles and the electrode. The electrochromic NPCs exhibited a large $\Delta\lambda$ (180 nm) under voltage in the range from 0.5 to 1.7 V due to the strong coulombic interaction and the low fraction of silica (17%). Moreover, they reported electrochromic NPCs with bistable and switchable properties by introducing polyethylene glycol (PEG) (Fig. 11h). The electrochromic NPCs display a colored state at the pristine state due to the order packing of silica particles. After applying a short time of voltage, the order structure is broken, leading to color transformation from a colored to a colorless state. PEG is used to increase the viscosity of the colloidal dispersion to hold the two states, which can be reversibly switched. Based on these characteristics, these electrochromic NPCs can easily switch their colors from ''on'' to ''off'' states with a relatively low consumption of electric power. However, it is difficult for this kind of electrochromic NPCs to display multiple colors in one unit under an electric field, and materials and techniques that can address this problem are practically required.

3.4.3 Electrochromic NPCs based on electrical anisotropy. Unlike the electrochromic NPCs based on liquid colloidal NPCs, Huang *et al.* reported an electrochromic system by co-assembling viologens with core–interlayer–shell (CIS) particles *via* a shear-induced assembly technique.[246] In this electrochromic system, the color brightness can be actively tuned by the voltage because of the different absorption of visible light at 0 and 1.5 V by viologens as chromophores (Fig. 11i). In addition, electrochromic NPCs can be realized by designing two-color Janus microspheres with electrical anisotropy on photonic microspheres.[135,247] For example, Kim *et al.* reported an electrically responsive Janus photonic microsphere that can display both structural and plasmonic colors (Fig. 11j).[248] Photonic microspheres were prepared by the self-assembly of silica in emulsion droplets of a photocurable resin and the selective removal of silica. The directional deposition of gold or aluminum on photonic microspheres produces plasmonic color in the upper hemisphere while maintaining the structural color in the lower hemisphere. When an electric field was applied, an electric dipole was generated in each Janus microsphere due to the different electrical properties of the two hemispheres.[249] Therefore, the Janus microspheres rotate with the change in the electric field direction, thereby achieving switching between the structural and plasma colors under electric field modulation. Unlike others, these electrochromic NPCs cannot generate continuous color change in response to the electric field.

3.5 Chemical-chromic NPCs

Chemical-chromic NPCs are complex response systems that can change their structural colors in response to ions, solvents, and biomolecules through variations in their lattice distance and refractive index.[250–255]

3.5.1 Ions-responsive NPCs. For instance, chemical-chromic NPCs that can selectively sense Pb^{2+}, Ba^{2+}, and K^{+} were first reported by Asher *et al.* through the introduction of a molecular recognition group (crown ether) into the polymer network of hydrogel NPCs (Fig. 12a).[256] Crown ethers can be complex with these cations and anchor the charge in the polymer network. The Donnan potential generated by the mobile counterion to the crown ether-bound cation leads to an increase in the osmotic pressure within the gel, which results in the swelling of the gel and the red shift of the reflection wavelength. The swelling degree of the hydrogel is related to the number of covalently-linked charged groups. Thus, chemical-chromic NPCs can detect Pb^{2+} in the concentration range of 0.1 μM to 10 mM. Similarly, grafting 8-hydroxyquinolinyl[257] and benzo-9-crown-3[258] to the hydrogel network can be used to detect Cu^{2+} (also Ni^{2+}, Co^{2+}, and Zn^{2+}) and Be^{2+}, respectively. Zhang *et al.* reported a PAIPAM gel-based chemical-chromic, which is stable and sensitive to ionic strength. As shown in Fig. 12b and c, the diffraction peak shifts over 450 nm as the [NaCl] increases from 10 to 667 mM. The variation in the reflection wavelength can be explained by the ion-induced deswelling of PNIPAM microgels, which results in the shrinkage of lattice distances.

3.5.2 pH-responsive NPCs. pH-responsive NPCs have been well developed, usually based on the interactions between H^{+} and the $-COO^{-}$ or $-NH_2$ from NPC hydrogels.[259–262] Lee *et al.* first reported a polyacrylamide NPCs hydrogel embedded with an array of nonclose-packed PS colloids that can be used to sense pH and ionic strength.[263] The pH-response NPCs showed a redshift of the reflection peak at pH values from 2.0 to 9.6 and a blue shift of the reflection peak at pH values from 9.6 to 11. The dependence of the reflection wavelength of NPCs on pH is derived from the response of ionic gels to changes in protonation and ionic strength. When polyacrylamide hydrogels hydrolyze, some of the amide groups hydrolyze to carboxyl groups and fix the counterions in the gel by ionization, leading to osmotic pressure generation and gel swelling. Thus, ionization increases with increase in pH and leads to gel swelling and reflection wavelength redshift. Upon completion of ionization (pH = 9), a further increase in pH increases the ionic strength, leading to a decrease in osmotic pressure and gel shrinkage. They also prepared pH sensors even with high ionic strength by introducing carboxyl groups into hydroxyethyl methacrylate colloidal arrays to form interpenetrating networks through secondary polymerization.[264] Zhang *et al.* prepared pH-responsive NPCs with defective states by the co-assembly of PNIPAM microgels and P(NIPAM-AA) microgels of the same size.[265,266] P(NIPAM-AA) microgels swell to larger sizes with increasing pH and induce defect formation and optical signal changes in NPCs. Guan *et al.* prepared pH-responsive 1D NPCs of poly(HEA-*co*-AA)-coated Fe_3O_4 particles.[267] As the pH increased from 3.6 to 7.2, the reflection peak of 1D NPCs was redshifted by 210 nm (Fig. 12d). Meanwhile, 1D NPCs have high resolution (2 μm) and fast response speed (40 ms).

3.5.3 Biomolecular-responsive NPCs. NPCs for biomolecular detection have been widely studied for their potential application in clinical diagnosis.[268–270] For example, Sharma *et al.* prepared NPC hydrogels for detecting creatinine levels by functionalizing polyacrylamide NPC with creatinine deiminase (CD) enzyme and 2-nitrophenol (2NPh) titration groups.[271] The

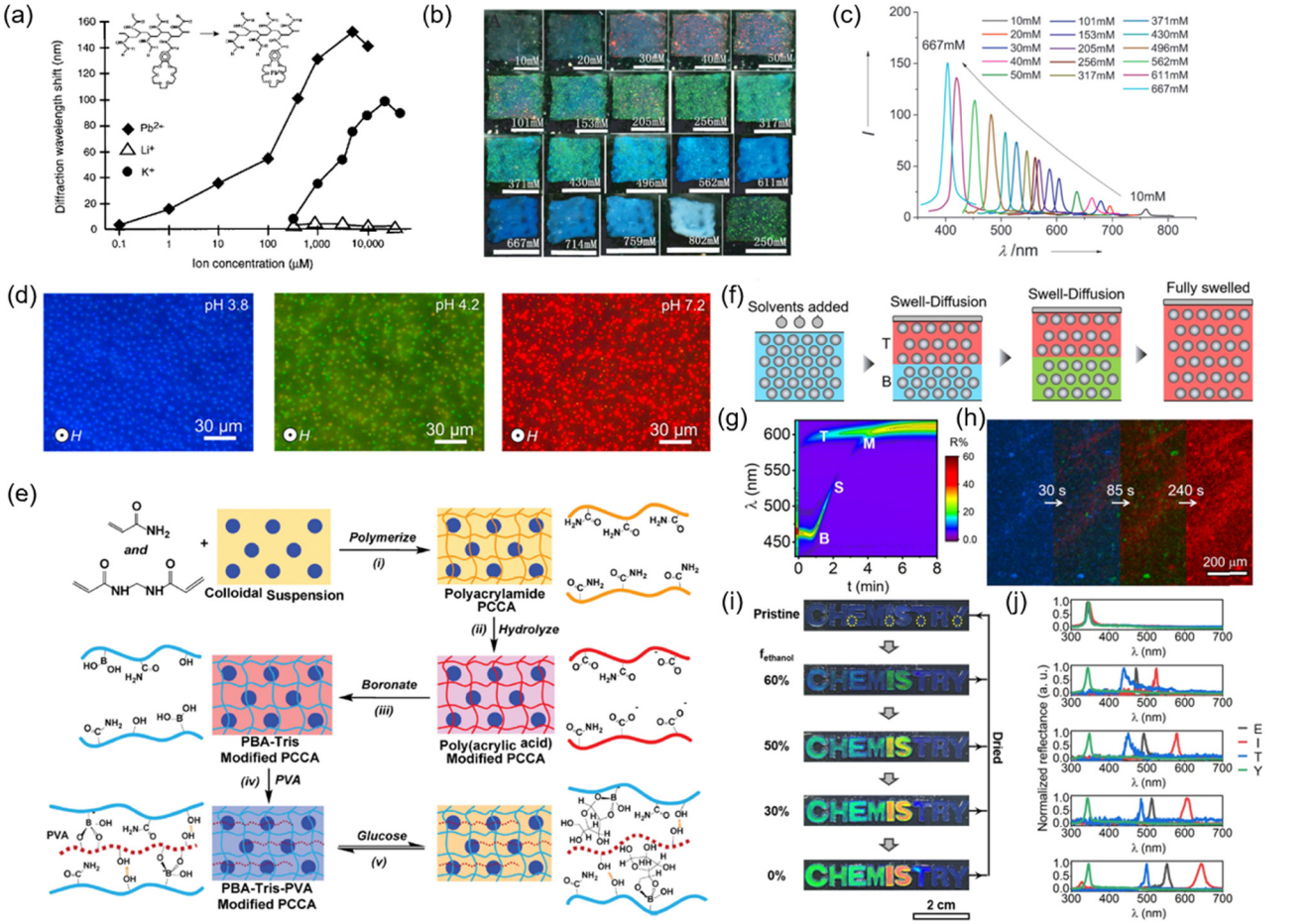

Fig. 12 (a) Dependence of the diffracted wavelength of the PCCA sensor on the concentration of cations bound by the crown ether. Reproduced with permission.[28] Copyright 1997, Springer Nature. (b) Photographs of a freestanding PMCC film taken with [NaCl] increasing from 0 to 750 mM. (c) Reflection spectra of the PMCC film measured at various [NaCl] values. Reproduced with permission.[206] Copyright 2013, Wiley-VCH. (d) Dark-field optical microscopy images of the as-obtained Fe_3O_4@PVP@poly(HEA-*co*-AA) photonic nanochains of the same batch in different pH buffer solutions. Reproduced with permission.[267] Copyright 2020, American Chemical Society. (e) Synthetic steps for forming the glucose-responsive polymerized crystalline colloidal array (PCCA). Reproduced with permission.[275] Copyright 2014, Wiley-VCH. (f) The working mechanism of the photonic paper in detecting the solvent. (g) 3D color counter map and (h) the microscopy images of the color change of the photonic paper used to detect ethanol. Reproduced with permission.[282] Copyright 2020, American Chemical Society. (i) Digital images of photonic crystals in a pristine state and immersed in the mixture of HAc and ethanol. The f_{PEGDA} of CHEM, IS, T, and RY is 5%, 1%, 12.5%, and 100%, respectively. (j) Reflection spectra of photonic crystals under dried state and immersed in mixed solvents with different $f_{ethanol}$: 60%, 50%, 30%, 0%. Reproduced with permission.[286] Copyright 2021, Elsevier.

limit for its detection of creatinine at the physiological pH and salinity is 6 μM. When the hydrogel is exposed to the creatinine environment, creatinine is hydrolyzed by the CD enzyme and then releases OH^-. The increased pH causes 2NPh deprotonation, resulting in hydrogel swelling and the redshift of the reflection peak. Walker *et al.* reported an NPC hydrogel for the detection of ultratrace amounts of sulfur phosphorus (4.26 fM) in a water solution.[272] The acetylcholinesterase (AChE) introduced in the hydrogel binds organophosphates to generate anion and dowsing potentials, which leads to hydrogel swelling and reflection wavelength redshift. Alexeev *et al.* first prepared glucose-sensing NPC hydrogels by grafting borate derivatives into a polyacrylamide-PEG polymer network.[273,274] The bis-bidentate complexes between glucose and borate lead to volume contraction of the hydrogel and the blueshift of the reflection peak position. Similarly, Zhang *et al.* prepared hydrogel NPCs with linear and rapid responses to glucose concentration under simulated physiological conditions by introducing volume resetting agents into phenylboronic acid-modified hydrogel NPCs.[275] The volume resetting agent caused glucose to form a 1 : 1 complex mainly with PBA, resulting in hydrogel volume dissolution and a redshift of the NPC reflection peak (Fig. 12e).

3.5.4 Solvatochromic NPCs. For solvatochromic NPCs, their reflection signal and colors change in solvents based on the swelling of the polymer. In such a system, the difference in affinity, solubility parameter, polarity, and refractive index between solvents and the polymer matrix of the NPCs is crucial to the detection of solvent species.[179,267,276–281] In general, it is a great challenge for conventional solvatochromic PCs to distinguish solvents with similar refractive indexes because their reflection wavelengths only depend on the refractive

indexes of solvents. Ge *et al.* proposed a method to distinguish solvents by recording the dynamic reflection spectrum (DRS) of NPC gels interacting with solvents and converting them into geometric patterns.[276] Based on the complex interaction between the solvents and the NPC gels, solvents (partial isomers) with similar refractive indices can be distinguished to some extent. However, the poor stability and nonrecyclability of NPC gels will limit their availability. Therefore, NPCs with good stability, recyclability, and accurate identification of solvents (homologues, isomers, similar refractive indexes, and structures) are highly desired. Our group established a dynamic swelling reflection spectrum (DSRS) to distinguish homologues, isomers, and other solvents with similar refractive indices based on the swelling interactions between the swellable NPC paper and the solvent.[282] When the top layer of the NPC paper is in contact with the solvent to be detected, the initial reflection wavelength of the swellable NPC will immediately split into two reflection signals due to the different swelling degrees between the top and bottom of the NPC paper, and these two reflection signals tend to merge in the swelling process (Fig. 12f–h). The variations in reflection signals and merging times are highly sensitive to the polarity and refractive index of the solvent, and this difference can be significantly amplified in DSRS, leading to the distinction of the solvent from its unique geometric pattern. Therefore, various isomers (alcohols, acids, bases, esters, and aromatics), isomers (propanol, butanol, dichlorobenzene, and trimethylbenzene), and other solvents with similar refractive index and structures can be accurately distinguished. Compared to DRS, the NPC paper for DSRS is stable and reusable. The working mechanism of DSRS is quite different from the DRS, where the NPC gel undergoes a complex swelling or extraction process and a complex diffusion behavior of the solvent in the NPC gel. In addition, DSRS can explain the trend of reflection intensity, which is important for understanding the working mechanism and identifying solvents with similar refractive indices. Based on a similar principle, the NPCs that can be swelled by water vapor can detect environmental humidity.[283] Besides opal structures that detect solvents, collapsed inverse opal structures can also sense solvents.[284] Kim *et al.* prepared a nonclose-packed macroporous hydrogel that can respond to a water–ethanol mixture.[281] The reflection peaks of NPC hydrogels changed with the concentration of ethanol, and this variation was due to the higher affinity of PEG chains for water than ethanol and the higher affinity of acrylate crosslinked junctions for ethanol than water in the acrylate matrix hydrogels.

Our group developed solvatochromic NPCs that can detect the concentration of solvent (ethanol and acetic acid) by controlling the crosslinking degree of swellable NPCs. There are two strategies to control the crosslinking degree of NPC, one of which is to swell NPC with a crosslinker. For example, NPC prints that can change their structural colors in response to the mixture of the ethanol–water were fabricated by the region-selective swelling of the premade NPC paper with 2-hydroxyethyl methacrylate (HEMA) and fixing the swelled region through photopolymerization.[285] The NPC paper with nonclose-packing structures was fabricated by the self-assembly of silica particles into poly(propylene glycol)acrylate (PPGA). The background can change its reflection wavelength and color (blue, clear, green, yellow, and red) depending on the volume fraction of ethanol. In contrast, the pattern will keep its reflection wavelength and structural color regardless of the solvent. Another is to mix different proportions of crosslinker into the NPC precursor solution. We prepared NPCs that can respond to different concentrations of acetic acid (a mixture of acetic acid and ethanol) by fixing nonclose-packed colloidal arrays with PEGPEA and PEGDA (Fig. 12i and j).[286] The crosslinking degree determined the maximum shift of the reflection wavelength, and the reflection peak position was tuned using the volume fraction of ethanol accordingly.

4. Applications of NPCs

Compared with CPCs, NPCs typically exhibit a larger tunable wavelength range, faster response, and higher sensitivity under similar stimuli due to the larger interparticle distances allowing for better responsive capability and speed. NPCs' unique capabilities in mechanochromic, chemical-chromic, thermochromic, magnetochromic, and electrochromic properties make them applicable in new applications in sensors, printing, anticounterfeiting, display, and fluorescence modulation.

4.1 Sensors

NPCs are highly attractive because of their capability of converting physical, chemical, and biological stimuli into visual readout colors. Hence, NPCs have been widely used for force/strain sensors, chemical sensors, biological sensors, and temperature sensors.[287]

4.1.1 Force/strain sensors. Mechanochromic NPCs can be used as visual force/strain sensors since they can change their structural colors by shrinking or expanding their lattice distances in response to mechanical forces. A good force sensor is considered to require a wide detection range, fast sensing speed, high sensitivity, and long-term stability. Hong *et al.* reported a method for preparing elastic PC hydrogel by the physical crosslinking of colloidal arrays.[180] The hydrogel PC has high deformability with a tensile deformation of over 2800% and a compressive deformation of over 98%. Zhu *et al.* introduced ionic liquids into mechanochromic NPCs to prepare photonic ionogels, which can sense strain by outputting optical and electrical signals (Fig. 13a).[188] Very recently, our group prepared extremely sensitive artificial chameleon skin NPCs by the simple self-assembly of silica particles into acrylates.[156,201,203,288] Compared to others, these artificial chameleon skins, showing high sensitivity, fast responsiveness, long-term stability, and good reversibility, are excellent candidates for self-reporting strains of earthworms instantly by outputting different colors during peristalsis.[201] As shown in Fig. 13b, the artificial chameleon skin can be directly covered on the skin of an earthworm and shows a bright red color when the earthworm is in a relaxed state. As the earthworm moves

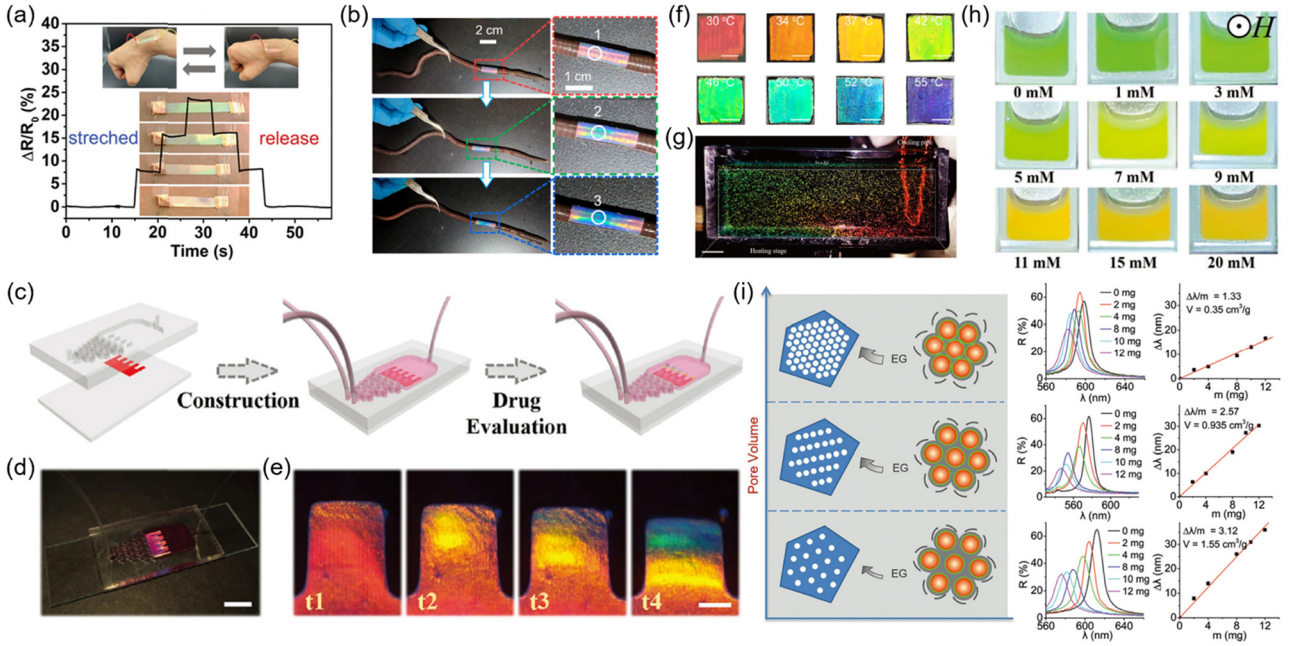

Fig. 13 (a) Real-time detection of various human motions recorded by the visual I-skin attached to the wrist. Reproduced with permission.[188] Copyright 2021, Wiley-VCH. (b) Digital photographs of the mechanochromic photonic skin of different strains attached to an earthworm. Reproduced with permission.[201] Copyright 2022, American Chemical Society. (c) Schematic diagram of the fabrication and assembly of heart-on-a-chip for drug evaluation. (d) Optical photograph showing the derived heart-on-a-chip. (e) Microscopy photographs showing the structural color variation in the functional hydrogel. Reproduced with permission.[289] Copyright 2022, Wiley-VCH. (f) Digital photographs of the thermochromic NCP PC film under different temperatures. Reproduced with permission.[133] Copyright 2022, American Chemical Society. (g) Photograph of a convection cell containing microcapsules in an aqueous medium. Reproduced with permission.[292] Copyright 2018, Wiley-VCH. (h) Digital photographs during the cyclic sweep of varying [glucose]. Reproduced with permission.[299] Copyright 2022, Wiley-VCH. (i) Porous material with a larger pore volume induces greater lattice shrinkage. Reflection peak blueshifts with the addition of mesoporous silica standards with known pore diameters. Reproduced with permission.[36] Copyright 2018, Wiley-VCH.

forward, its segments increase and the length of the artificial chameleon skin increases accordingly, thereby changing the color of the artificial chameleon skin from red to green and blue. These artificial chameleon skins may be applicable for visually reporting the strains of other annelids and animals, such as leeches, lobworms, and snakes.

Mechanochromic NPCs are an ideal platform for constructing biochips and detecting cellular microscopic forces.[289,290] Sun *et al.* prepared hydrogels with conductive and anisotropic structural colors by polymerizing NPCs on thin sheets of super-aligned carbon nanotube sheets (SACNTs).[289] The hydrogel consists of a hydrogel layer with a nonclose-packed structure and a conductive methacrylate gelatin/SACNTs film. Anisotropic SACNTs can induce cardiomyocyte alignment, and their conductivity promotes the synchronized beating of cardiomyocytes. The consistent beating of cardiomyocytes leads to the deformation of the hydrogel of NPCs and causes changes in the reflection wavelength and structural color. Fig. 13c–e shows the heart-on-a-chip with a conductive NPC hydrogel as the platform and the structural color change of the NPC hydrogel driven by the beating of cardiomyocytes.

4.1.2 Temperature sensors. Thermochromic NPCs are promising for temperature sensors because they can sensitively change their structural colors in response to thermal stimuli.[124,208,291,292] For example, Wu *et al.* prepared NPC films by filling PNIPAM hydrogels into the gaps of ZnS nonclose-packed array by a two-step filling method and used these films to sense temperature. The structural color of thermochromic sensors was blueshifted from red to orange, yellow, green, cyan, and blue as the temperature increased from 30 to 55 °C (Fig. 13f). In addition to the temperature sensor in the form of a film, microenvironmental temperature sensors have been developed based on the NPC temperature capsule, which can be used as an individual temperature sensor unit.[67,205,293] Weitz *et al.* reported the preparation of thermochromic microcapsules by immobilizing nonclose-packed colloidal crystals in NIPAM hydrogels by microfluidic techniques.[205] When the NPC microcapsules were heated from 22 to 40 °C, PNIPAm gel shrinkage resulted in a blueshift of the structural colors of the microcapsules from deep red to green. Due to the small diameter of NPC microcapsules (100 μm) and their ability to work independently, they can output different structural colors to report the variations in microenvironmental temperature. Similarly, Choi *et al.* assembled the core–shell particles into colloidal crystals by depletion attraction and encapsulated them into microcapsule cores.[292] The p(NIPAm-*co*-AAc) shell of the colloidal particles enabled the colloidal crystals to quickly tune the structural color in response to temperature changes. The spherical symmetry of the microcapsules caused the colloidal crystals to display an angle-independent structural

color. The structural color of microcapsules shifted from red to green when the temperature was heated from 25 to 38 °C. The spatial distribution of temperature information can be obtained by observing the structural color of microcapsules dispersed in water (Fig. 13g). In addition, Furumi *et al.* demonstrated the application of NIPAM gel particles-based liquid NPCs for temperature sensing.[294] The NPCs show bright structural colors at 28 °C. When a finger attaches to the liquid NPC and its temperature is increased to 29.5 °C, the structural color of the attached region disappears due to the shrinkage of the gel particles.

4.1.3 Chemical and biological sensors. NPC sensors that can visually sense pH,[261,263–267] ions,[28,255–258] solvents,[179,264,276,277,283,295] biomolecules,[271–273,275] and microorganisms[261,296,297] are significant for daily life. For example, Kong *et al.* reported the real-time and *in situ* detection of microenvironmental pH and adaptive fluids by self-adaptive magnetic photonic nanochain cilia arrays (SMPNCAs).[262] SMPNCAs were prepared by the magnetic assembly and UV-assisted hydrogen bonding-guided template polymerization techniques printed on a glass substrate. SMPNCAs tuned the interparticle distance and exhibited different structural colors in response to changes in the pH value of the environment through reversible volume changes of the hydrogel shell. The structural color of SMPNCAs is blueshifted from red to green when the pH value is decreased from 6.2 to 4.3. NPC-based hydrofluoric acid (HF) sensors can visually and precisely detect 0–10 mM HF.[295] Our group reported an HF sensor by self-assembling the nonclose-packed silica particles into hydroxyethyl acrylate (HEA) and subsequently swelling in water. When the NPC hydrogel was immersed in HF aqueous solution, the silica particles were slightly etched by HF, causing a further swelling of the NPC hydrogel and a redshift of the structural colors. This HF sensor is customizable, portable, easy to use, and low cost (<0.01 per sensor), which offers highly practical value and mass production potential. Most NPC sensors for the quantitative analysis of solvents are based on the recording of the reflection wavelength shift caused by the variations of lattice distance and refractive index during the swelling process. Wang *et al.* reported an NPC sensor by the shear-induced assembly of core–interlayer–shell particles into diethylene glycol dimethacrylate (DEGMEMA) to detect the solution of ethanol/water or ethanol/octane.[279] The as-prepared NPC film was tailored as a test strip to detect ethanol concentration by immersion in the ethanol/octane solutions. With the ethanol concentration increasing from 0% to 9%, the structural color of test strips redshift from green to orange. NPC sensors for sensing biomolecules such as glucose have been widely studied for their advantages of visual readout and noninvasive detection of diabetes.[269,270,275,298] Cai *et al.* prepared glucose-sensing NPC probes with response times in the seconds range by the selective concentration polymerization of monomers in microheterogeneous solutions of dimethyl sulfoxide and water.[299] The NPC probe consists of one-dimensional nonclosely-packed magnetic nanochains wrapped in poly(3-acrylamido phenylboronic acid-*co*-N-2-hydroxyethyl acrylamide) (poly(AAPBA-*co*-HEAAm)). As the glucose concentration varied from 0 to 20 mM, the structural color of the NPC probe redshifts from green to orange (Fig. 13h).

Biological sensors based on NPCs can detect microorganisms in a simple, efficient, low-cost, and visual way. For instance, Asher *et al.* reported a 2D NPC to selectively detect *Candida albicans*.[296] The biological sensor consists of a Concanavalin A (Con A) protein hydrogel embedded in a 2D NPC, and their detection limit for *Candida albicans* is about 32 CFU mL^{-1}. When the concentration of *Candida albicans* increases from 0 to 6×10^5 CFU mL^{-1}, the structural color of the biological sensor blueshifts from green to blue due to the crosslinking of the cell-surface mannan and hydrogel Con A sites and the reduction of Con A hydrogel volume.

4.1.4 Other sensors. Magnetochromic NPCs can be used to detect the magnetic field strength.[219,300,301] For example, He *et al.* developed a general and mild approach for the fabrication of highly dispersive anisotropic magnetic colloids by the low-temperature conversion of nonmagnetic templates and their application for the naked-eye detection of extremely weak magnetic fields.[219] Due to the high sensitivity of the ferromagnetic Fe_3O_4@p-SiO_2 particles, the magnetic sensor changes its colors from yellow to green as the field strength increases from 7 to 239 Gauss. Ge *et al.* reported a liquid NPC-based mesopore detection technique by the measurement of the reflection wavelength changes.[36] The liquid NPCs were prepared by the self-assembly of silica particles into an ethylene glycol/ethanol solution. When the liquid NPCs are mixed with mesoporous materials, part of the solvents will be irreversibly absorbed into the mesopore, leading to a decrease in the lattice distance and blueshifts of reflection wavelength. As shown in Fig. 13i, the pore volume is positively correlated with the changes in reflection wavelength caused by the unit mass of the porous material. In addition, they found that the pore diameter is negatively related to the average absorption temperature of the mesopores. Based on the relationship between the volume and diameter of the mesopore and the reflection wavelength, the pore volume and diameter of mesoporous material can be measured in about 2 hours.

4.2 Printing

NPC-based printing techniques can create patterns with iridescent and photobleaching-resistant structural colors. NPCs are usually used as ink for the direct printing of patterns.[15,95,302–307] NPC inks consisting of polymerizable monomers and colloidal particles form NPCs by repulsive forces between colloidal particles after printing into patterns and fixing the ordered structure by light curing. Multicolor patterns are realized by the regulation of the diameter and volume fraction of the building blocks. For example, Kim *et al.* reported a strategy to realize structural color printing by the direct writing of NPC inks.[154] NPC inks were configured by dispersing silica particles in a light-curing resin at a volume fraction suitable for the printing and crystallization of colloidal particles. The printing of the pattern was accomplished by a dispenser following a pre-programmed pattern trajectory and controlling the writing speed (Fig. 14a). Multicolor patterns can

be written directly on various substrates as well as peeled from the substrate to form self-supporting NPC films. Furthermore, inks can also be used for 3D printing.[308] Song *et al.* first reported the fabrication of 3D NPC structures by a continuous digital light processing (DLP) 3D printing strategy and hydrogen bonding-assisted NPC inks.[309] Uniform dispersion induced by hydrogen bonding and suction force induced by continuous curing mode enable simultaneous colloidal assembly and printing. As shown in Fig. 14b, the koi fish model with four structural colors has been fabricated by controlling the ink volume and the diameter of the PS particles to print in segments. Gu *et al.* developed a sacrificial scaffold-mediated two-photon lithography (TPL) strategy that combines a bottom-up nanoparticle self-assembly process with a top-down TPL process to fabricate 3D NPC microstructures.[310] Fig. 14c illustrates the simple geometry and complex lotus-like 3D microstructure with brilliant structural colors.

The structural color of the printing patterns can also be modulated by the magnetic field and electrical field. Kwon *et al.* demonstrated a high-resolution pattern with multiple structural colors using a single NPC material.[15] This material, M-ink, was developed by self-assembly into 1D NPCs *via* magnetically attractive and repulsive forces in a photocurable resin. During the printing process, a magnetic field was used to modulate the structural color and fix the preset pattern by masking and lithography (Fig. 14d). Chen *et al.* reported electrochromic NPCs for electric field-assisted multicolor printing, which was self-assembled by silica particles into a mixture of propylene carbonate and ETPTA (Fig. 14e).[242] The prepared NPCs, as E-ink, have an electrochromic, sub-stable, reversible assembly, and polymerizable properties, thus leading to the preparation of structurally color-tunable, grayscale controllable, and instantaneously immobilized patterns.

Generally, patterns printed directly using NPC as ink are fixed by chemical crosslinking and cannot be reconfigured. To address this issue, Ge *et al.* reported a rewritable NPC paper using hygroscopic salts as inks.[95] The NPC paper was prepared by the magnetic assembly of Fe_3O_4@SiO_2 colloidal particles in PEGDA, followed by UV curing to fix the structures. An aqueous solution of salt chloride was used to swell the polymer matrix, causing an increase in the lattice distance and redshift of reflection wavelength. The pattern can be retained for a long time because of the hygroscopic properties of chloride salts. The NPC paper can be rinsed with distilled water to dissolve the

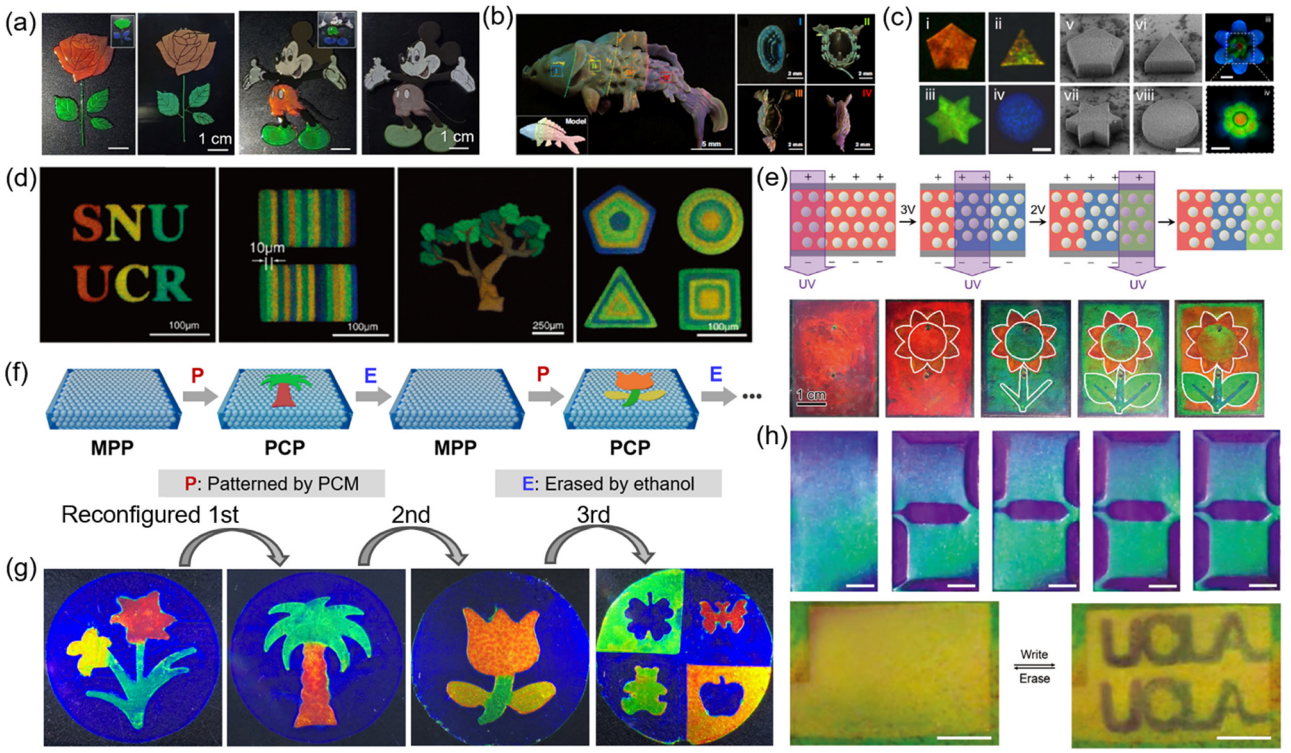

Fig. 14 (a) A rose and leaves are direct-written using EA and UA inks. The inset is an off-normal observation. Mickey Mouse printed using EA and UA inks. Reproduced with permission.[154] Copyright 2021, American Association for the Advancement of Science. (b) Optical image of the multistructural color koi fish continuously printed with four different PS latex particle diameters. Reproduced with permission.[309] Copyright 2022, Springer Nature. (c) 2D colloidal crystal microstructures with different geometries and colors. Reproduced with permission.[310] Copyright 2022, Springer Nature. (d) High-resolution multicolor patterns are produced using magnetic ink. Reproduced with permission.[85] Copyright 2012, American Chemical Society. (e) Mechanism of multicolor printing *via* repeated electric tuning and UV curing. Lithographic printing of multicolor flowers by periodical photomask covering, electric field tuning, and UV curing. Reproduced with permission.[242] Copyright 2017, Wiley-VCH. (f) Schematic illustration of the reconfiguration process. (g) Digital photos of PC paper and patterns of each reconfiguration. Reproduced with permission.[288] Copyright 2022, American Association for the Advancement of Science. (h) Selected images of a photonic paper sequentially demonstrating digits 0–9. Reproduced with permission.[311] Copyright 2018, Wiley-VCH.

residual salt and return to its original state after drying; thus, the photonic paper can be written repeatedly. Our group reported a reconfigurable printing strategy through the combination of swellable NPC paper and phase change material (PCM).[288] The patterns can be printed by region-selective swelling NPC paper using PCM as ink and erased by soaking the print in ethanol to remove the PCM (Fig. 14f). As illustrated in Fig. 14g, the patterns with diverse color contrasts have been printed by controlling the swelling time and can be reconfigured repeatedly. Full-color and high-resolution patterns can be reconfigured in a green and low-cost manner and exhibit long-term stability and recordable properties under normal conditions. In addition, the patterns show different mechanochromic properties relying on the initial wavelength and structural colors after swelling. Based on their unique characteristics, the as-prepared patterns can be used for a novel pressure-based anticounterfeiting mode with programmable color changes of patterns under pressure. Pei *et al.* combined 1D NPCs, shape memory polymers, and electroactive polymers to develop an ink-free rewritable NPC paper.[311] NPC papers were prepared by embedding Fe_3O_4@C particle-assembled 1D NPCs into bistable electroactive polymers. The electric actuation caused the deformation of the electroactive polymer, leading to a reduction of the interparticle spacing and a blue-shift of the structural color in the driven region (Fig. 14h). The pattern printed by the electric drive can be permanently retained by the shape memory property of NPC paper until it is heated back to its initial state. The pattern can be rewritten over 500 times on photonic paper without noticeable degradation.

4.3 Anticounterfeiting

Anticounterfeiting technology has gained much attention for its wide application on banknotes, identification documents, stamps, and luxury goods.[312–315] Among the various anticounterfeiting materials, NPCs show potential for anticounterfeiting applications due to their resistance to photobleaching, angle-dependence, and tunable structural colors. The optical properties of NPCs arise from their periodic structure and corresponding materials, rendering them difficult to replicate or simulate.[316,317] Anticounterfeiting based on NPCs can be divided into two types. The first type is nonresponsive NPCs based on anticounterfeiting technology, which mainly utilize the angular correlation of their structural colors, ultranarrow optical forbidden bands, and high optical transparency.[318] Lee *et al.* reported a strategy to prepare highly transparent NPCs and multilayer structures by light-curing colloidal crystal suspensions.[47] An optical palette of structural colors was realized by overlapping multiple layers of NPCs. In addition, multicolor NPCs micropatterns were prepared by a photolithography process. The NPC micropatterns presented rich structural color during the angle change. Our group combined near-infrared photonic crystals (NIRPCs) of different reflection wavelengths with their spatial reflection spectra (SRS) to build a new coding–decoding system.[51] NIRPC films were obtained by the self-assembly of silica particles in PEGPEA. The coding information of NIRPCs was hidden under ambient conditions due to their similar structural color but can be revealed by the SRS patterns. More complex coding can be realized by overlaying multiple layers of films (Fig. 15a and b).

The other anticounterfeit strategy is to use responsive NPCs to create structural color changes in their anticounterfeit patterns under corresponding stimuli.[195,228,280,319,320] Our group prepared responsive photonic prints (RPPs) by the selective swelling of swellable photonic paper with HEMA as the ink.[285] The RPPs can rapidly and reversibly display five structural colors in different concentrations of alcohol solutions, benefiting from the asymmetric solvation behavior between the patterns of RPPs and the background. Inspired by chameleons and insect wings, we designed the NPC gels that can reversibly switch their colors based on the matching/mismatching of the refractive index.[56] The NPC gels were prepared by fixing the nonclose-packed silica particles in the mixture of HEA and PEGPEA through photopolymerization and swelling in solvents. Due to the matching of the refractive index ($\Delta = 0$), these NPC gels are highly transparent with the off state in water but show iridescent colors with the on state in other solvents because of $\Delta n \neq 0$. As shown in Fig. 15c, the as-prepared NPC patterns were invisible in water and exhibited a brilliant multicolor in acetonitrile. In addition, we reported a dual-mode anticounterfeit photonic pattern based on photoluminescent (PL) and responsive NPCs.[321] Responsive NPCs were prepared by assembling dye-doped silica in non/swellable polymers. Under normal conditions, the prepared photonic patterns had uniform structural color due to similar particle size, lattice constants, and refractive index. When the photonic patterns are exposed to UV irradiation or immersed in water, the hidden patterns based on PL and structural colors can be displayed immediately and reversibly (Fig. 15d). Li *et al.* developed a novel multiangle photochromic NPCs.[322] The photochromic NPCs were prepared by mixing spiropyran powder with CIS particles through BIOT-induced self-assembly. The patterns of NPCs exhibited different color-switching indoors and outdoors due to the photochromic molecules turning fuchsia under UV irradiation (Fig. 15e).

NPCs-based ''invisible photonic prints'' have patterns that are invisible under normal conditions and can only be recognized when stimulated by force,[323] magnetic fields,[324,325] or solvents.[303,305,326] Ge *et al.* reported an invisible print based on water-responsive 1D NPCs, which was prepared using photolithography to create different crosslinking or degrees of hydrophobicity on photonic paper containing siloxane.[303] Upon inking of the invisible pattern in water, the different dissolution rates of the pattern and the background caused different reflection wavelengths and structural colors between them. Thus, the pattern was revealed (Fig. 15f). Subsequently, they developed an invisible print based on mechanochromic NPCs. The invisible print was prepared by soaking photonic paper in a crosslinking agent (PEGDA) and selectively UV-curing the patterned parts.[323] The crosslinked patterns were close to the photonic structure of the background but with different mechanochromic abilities so that the patterns were invisible in the relaxed state but revealed under photonic paper deformation (Fig. 15g). Our group reported a simple and rapid

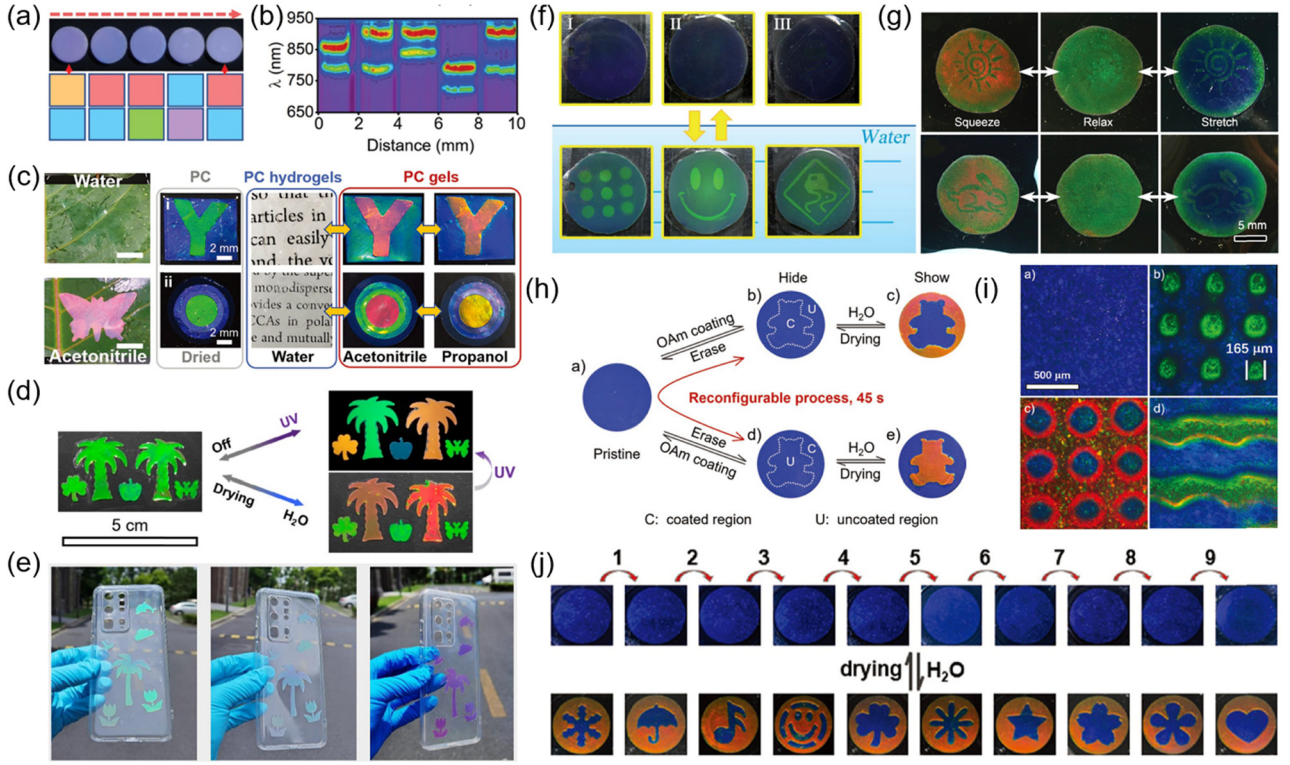

Fig. 15 (a) Digital photographs, schematics, and corresponding (b) SRS patterns of line codings with combinations of dual layers. Reproduced with permission.[51] Copyright 2021, The Royal Society of Chemistry. (c) Digital photos of the PC gel with a butterfly pattern in water and acetonitrile on the leaves. Digital photos of the PC gel with a butterfly pattern in water and acetonitrile on the leaves. Reproduced with permission.[56] Copyright 2022, Wiley-VCH. (d) Digital photo invisible photonic crystal prints in a pristine state under UV illumination and soaked in water. Reproduced with permission.[321] Copyright 2021, Wiley-VCH. (e) Multiangle photochromism (outdoors) effect of the functional PC films with different patterns on the phone case. Reproduced with permission.[322] Copyright 2022, American Chemical Society. (f) Photos of invisible prints prepared by crosslinking (I, II) and modification (III) methods, respectively, where the corresponding samples are soaked in water for 5 min. Reproduced with permission.[303] Copyright 2012, The Royal Society of Chemistry. (g) Invisible photonic prints of sunlight and a rabbit hidden in a relaxed state and shown by deformation. Reproduced with permission.[323] Copyright 2014, Wiley-VCH. (h) Reconfigurable construction of an invisible photonic pattern. (i) Invisible photonic print with various high-resolution patterns. (j) Digital photos of the invisible photonic print with reconfigurable patterns that can be hidden and shown in a dried state and in water, respectively. The diameter of the circle is 1 cm. Reproduced with permission.[326] Copyright 2020, Wiley-VCH.

strategy for preparing invisible photonic prints with a reconfigurable pattern that involves selectively coating a layer of oleylamine (OAm) on hydrophilic photonic paper (Fig. 15h).[326] Owing to the different swelling abilities of the pattern and the background area, the pattern was invisible under normal conditions, and once it was soaked with water, the pattern was revealed in a short time (2 s) with a large color contrast. Moreover, the invisible pattern can be reconfigured without losing its properties on a macro/microscopic scale (Fig. 15i and j).

4.4 Display

NPCs are promising materials for next-generation display devices due to their nonphotobleaching structural colors, high contrast, and low energy consumption. Displays are mainly based on electrochromic NPCs displays,[131,135,230,236,239–241,243,247,327] magnetochromic NPC displays,[159,215,216,222,226,235,328,329] and mechanochromic NPCs. Shim *et al.* reported electrochromic NPCs formed by nonclose-packed and highly charged PS particles.[236] On being exposed to an electric field, the lattice of NPCs was compressed along the [111] direction, and the structural color blueshifted due to the electrical packing force applied to the particles. The color of the pattern can be changed quickly and reversibly by applying a localized electric field and regulating the voltage (Fig. 16a). Fu *et al.* developed an electrochromic NPC display with a wide tuning range, high saturation structured color, fast electrical response, good reversibility, and better operating stability.[131] CeO_2@SiO_2 has a high refractive index, forming a large refractive index contrast with propylene carbonate, resulting in NPC with a wide bandgap and high saturation structural color. The dynamic pixel patterns displayed by 3 × 3 cell arrays fabricated from NPCs under programmed electric fields reveal their great potential for applications in the display (Fig. 16b and c).

The structural color of the magnetochromic NPC display can be actively tuned by the magnetic field. Fang *et al.* reported a magnetochromic NPC ink that can be used for optical displays.[222] The NPC ink was prepared by dispersing Fe_3O_4 particles in ethylene glycol and forming an emulsion in silicone rubber. The Fe_3O_4 particles can be well preserved within the

emulsion droplets of the ink and result in a structured color change from red to blue with the increase in the applied magnetic field strength (Fig. 16d and e). Magnetochromic NPC inks can be 3D printed to form custom patterns (Fig. 16f). Li *et al.* reported the magnetic assembly of tetragonal colloidal crystals from magnetic nanorods and demonstrated the assembly of magnetic nanorods along a size-dependent critical angle. The morphological anisotropy and magnetic anisotropy of magnetic nanorods lead to the nonclose-packed and hard-contact phase. The tetragonal colloidal crystals with nonclose-packed structures exhibited bright structural colors that could be actively tuned by magnetic field orientation (Fig. 16g–i). Photonic Janus spheres with programmable structural color switching with magnetic field response were designed by Kim *et al.*[235] The resin on the lighter side of the Janus ball contains carbon black and magnetic nanoparticles, and the heavier resin was the NPC self-assembled from silica. The direction of the magnetic moment of the Janus ball was determined by the direction of the external magnetic field during the UV curing process. As shown in Fig. 16j, the butterfly pattern consisting of two green and red Janus balls with opposite magnetic moment directions presented structural color switching under different external magnetic field directions.

Ge *et al.* demonstrated the potential of mechanochromic NPCs for display applications by selectively pressing mechanochromic NPCs gels embedded in PDMS through coaxially-fitted cylinders or hollow cylinder pins to generate red, green, and blue pixels.[199] NPCs with high sensitivity and wide tunable wavelength range are essential for high-resolution and multicolor displays.[153,180,187] Our group used the as-prepared mechanochromic NPCs for multicolor and high-resolution

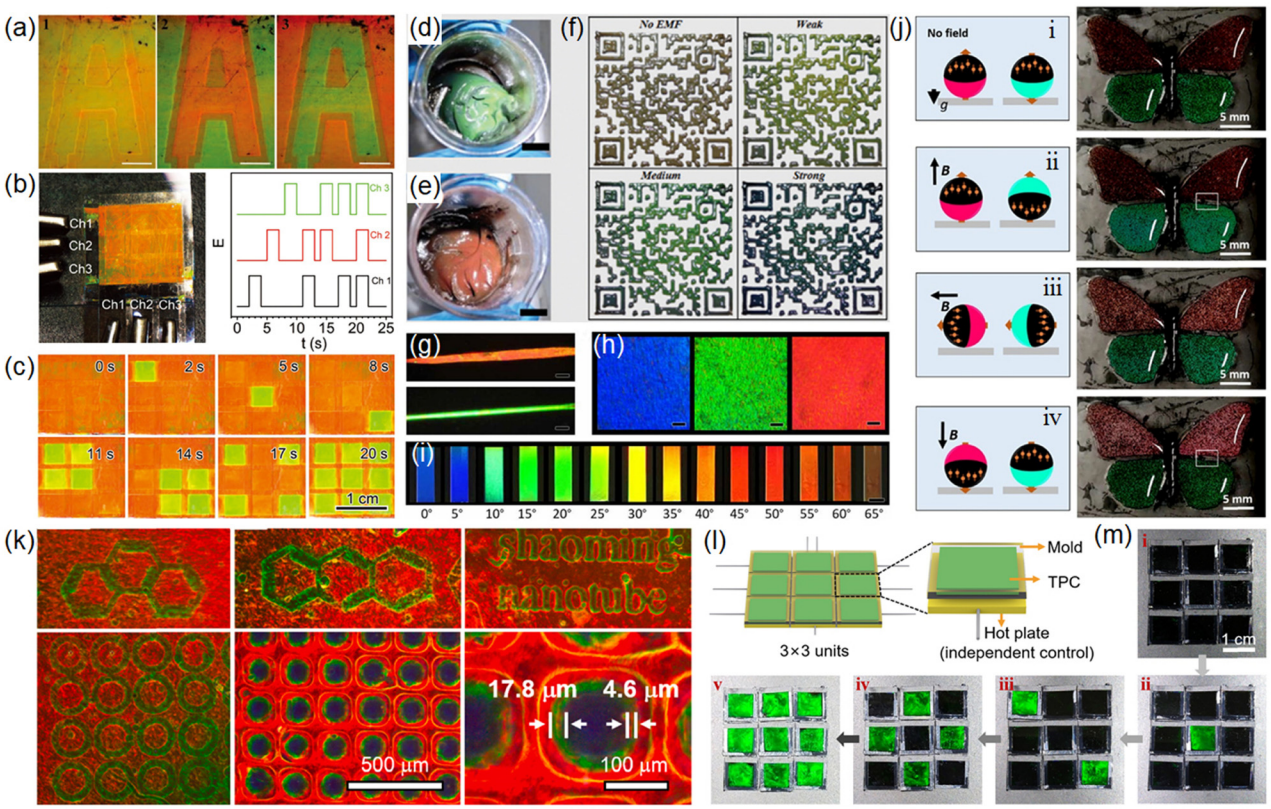

Fig. 16 (a) 1: Optical microscope image of CCAs without an electric field. 2 and 3: Optical microscope images showing "A" taken at reversely tuned states. The scale bar is 1 mm. Reproduced with permission.[236] Copyright 2010, Wiley-VCH. (b) PC-based display unit composed of a 3 × 3-pixel cell array. Programmed potentials on three channels. (c) Digital photos of the PC display unit at the denoted times. Reproduced with permission.[131] Copyright 2018, Wiley-VCH. Photos of the MRPC emulsion ink made using (d) MNCs-400 and (e) MNCs-300 for 3D printing under EMF, displaying their main jade green and brownish-red colors. (f) Photos of the 5 × 5 cm QR codes printed using the MRPC ink made with MNCs-400, showing its grey color in the absence of EMF and blueshifting structural color with increasing EMF strength. Reproduced with permission.[222] Copyright 2021, The Royal Society of Chemistry. (g) Optical microscopy images of a bct crystal under different orientations. (h) Optical microscopy images of the bct crystals under different magnetic field directions: blue at 0°, green at 20°, and red at 45°. (i) Structural colors of rod dispersion under different magnetic fields. Reproduced with permission.[130] Copyright 2021, American Association for the Advancement of Science. (j) Sets of schematics and the optical image showing regioselective color switching in a butterfly pattern under four different field conditions. Reproduced with permission.[235] Copyright 2020, American Chemical Society. (k) Multicolor and high-resolution patterns at the microscale. Reproduced with permission.[156] Copyright 2022, Elsevier. (l) Schematic illustration of the display array consisting of 9 TPC-based pixels. (m) Digital photos of any desired patterns by controlling the temperature of each pixel. Reproduced with permission.[213] Copyright 2022, Wiley-VCH.

displays based on their high sensitivity, fast response time, and good reversibility.[156] The micropatterns of the structural isomers of anthracene, letters, and circular arrays were prepared by pressing mechanochromic NPCs onto finely patterned stamps (Fig. 16k). In addition, we developed display applications based on the unique and attractive ''off/on'' characteristics of thermochromic photonic crystals (TPCs).[213] As shown in Fig. 16l, the prepared liquid TPC was injected into a mold as the display units. The initial liquid TPC at room temperature shows the black color of the background due to the refractive index matching. When the heating plate selectively heats the display unit, the liquid TPC increases in reflectance and structural colors appear as a result of the increased refractive index contrast (Fig. 16m).

4.5 Optical devices

The photonic bandgap of NPCs has attracted much attention for their potential applications in lasers,[57,177,294,330] filters,[331,332] and fluorescence modulation.[333] Foulger *et al.* reported the dynamic tuning of the emission spectrum of thin-film organic lasers by mechanochromic NPCs.[57] The reflection peaks of NPCs not only coincided with the photoluminescence peaks of rhodamine B (RhB) dyes but were also able to reflect most of the fluorescence into the cavity to promote stimulated emission. Ge *et al.* prepared an NPC film with an ultranarrow band gap.[331] The high crystallinity of the microcrystals in the NPCs, uniform crystal orientation, and very close refractive indices between silica and PEGDA resulted in an ultranarrow photonic forbidden band (FWHM: 6 nm). NPCs films combined with commercial optical filters can produce monochromatic transmitted light. Zhu *et al.* demonstrated the dynamic modulation of fluorescence luminescence by mechanochromic NPCs.[333] During the stretching of mechanochromic NPC, the PL strength of the film surface increased by 1.8 times when PBG was matched with the PL peak, while the PL strength of RhB doped into the film decreased by 40%. The above results indicate the potential of mechanochromic NPC as a platform for the dynamic regulation of PL.

5. Conclusion

Given their unique nonclosely packed structures and tunable optical signals in response to external stimulus, NPCs are considered to be promising materials for intelligent color change. This review summarizes the recent advances in the fabrication strategies, stimuli-responsive functions, and emerging applications of NPCs. A series of fabrication strategies for 1–3D NPCs are described, including magnetic assembly for 1D NPCs, reactive ion etching for 2D NPCs, and electrostatic self-assembly, magnetic field-induced assembly, shear-induced assembly, a combination of self-assembly, and micromachining for 3D NPCs. NPCs with mechanochromic, chemicalchromic, magnetochromic, and electrochromic properties are classified according to their different functions, and their working mechanisms are delineated. In addition, various applications of NPCs are discussed in detail, such as highly sensitive sensors employed for sensing force/strain, biochemical stimuli, and temperatures; NPC-based multicolor, high-resolution, reconfigurable pattern printing technology; anticounterfeiting labels based on NPC's angle-dependent structural color and stimuli-responsive functions; NPC displays based on the electric field, magnetic field, force, and temperature regulation; and optical devices based on the PBG of NPCs.

Although NPCs have made significant progress in recent years, challenges still remain in their fabrication, optical properties, and functionalities. First, 1D NPCs can be prepared simply and rapidly by the magnetic assembly, but the area of the magnetic field limits their large-scale assembly. The fabrication of 2D NPCs is high-cost and typically requires a time-consuming and complex process. 3D NPCs can be simply and rapidly fabricated by assembling colloidal particles into polymers or solvents. However, there are still some challenges. For example, the high crystallization threshold of colloidal particles leads to a low volume fraction of polymers of 3D NPCs, which limits their response speed and sensitivity. Second, the refractive index values of polymeric matrices are usually in the range of 1.3–1.5, close to those of the most widely used colloidal particles such as silica (n = 1.46) and polystyrene (n = 1.59). The small Δn between building blocks and polymeric matrices leads to a weak reflectance and color saturation of NPCs. Ideal NPCs with high sensitivity and high reflectance usually require a low crystalline threshold of building blocks and a large Δn. Third, large-scale fabrication, long-term stability, reversibility, and usability are critical for practical applications. Finally, single-functional NPCs can no longer meet the diverse needs of people, and the development of multifunctional NPCs is highly desirable. We believe that the combination of novel functional polymers and building blocks may offer new possibilities to prepare multifunctional NPCs and facilitate their all-round applications.

Author contributions

D. P. Yang and S. M. Huang conceived the project and supervised the writing. Y. Hu and S. Y. Yu contributed equally to this work and the writing of the manuscript. B. R. Wei and D. K. Ma contributed to the revision of the manuscript.

Conflicts of interest

The authors declare no competing interests.

Acknowledgements

This work was financially supported by the National Natural Science Foundation of China (51920105004, 21673160, and 51372173), NSFZJ for Distinguished Young Scholars (LR16B010002), the Natural Science Foundation of Guangdong Province (2023A-1515010063), and the Guangzhou Science and Technology Program (202201010525).

Notes and references

1 P. Vukusic and J. R. Sambles, *Nature*, 2003, **424**, 852–855.
2 X. Gao, X. Yan, X. Yao, L. Xu, K. Zhang, J. Zhang, B. Yang and L. Jiang, *Adv. Mater.*, 2007, **19**, 2213–2217.
3 Y. Zhao, Z. Xie, H. Gu, C. Zhu and Z. Gu, *Chem. Soc. Rev.*, 2012, **41**, 3297–3317.
4 J. Teyssier, S. V. Saenko, D. van der Marel and M. C. Milinkovitch, *Nat. Commun.*, 2015, **6**, 6368.
5 S. Wu, H. Xia, J. Xu, X. Sun and X. Liu, *Adv. Mater.*, 2018, **30**, 1803362.
6 J. P. Vigneron and P. Simonis, *Phys. B*, 2012, **407**, 4032–4036.
7 Z. Cai, Z. Li, S. Ravaine, M. He, Y. Song, Y. Yin, H. Zheng, J. Teng and A. Zhang, *Chem. Soc. Rev.*, 2021, **50**, 5898–5951.
8 A. C. Arsenault, D. P. Puzzo, I. Manners and G. A. Ozin, *Nat. Photonics*, 2007, **1**, 468–472.
9 D. P. Puzzo, A. C. Arsenault, I. Manners and G. A. Ozin, *Angew. Chem., Int. Ed.*, 2009, **48**, 943–947.
10 I. Lee, D. Kim, J. Kal, H. Baek, D. Kwak, D. Go, E. Kim, C. Kang, J. Chung, Y. Jang, S. Ji, J. Joo and Y. Kang, *Adv. Mater.*, 2010, **22**, 4973–4977.
11 S. Y. Lee, S.-H. Kim, H. Hwang, J. Y. Sim and S.-M. Yang, *Adv. Mater.*, 2014, **26**, 2391–2397.
12 L. Bai, V. C. Mai, Y. Lim, S. Hou, H. Mohwald and H. Duan, *Adv. Mater.*, 2018, **30**, 1705667.
13 M. Chen, Y. Tian, J. Zhang, R. Hong, L. Chen, S. Chen and D. Y. Son, *J. Mater. Chem. C*, 2016, **4**, 8765–8771.
14 B. Li, C. Ouyang, D. Yang, Y. Ye, D. Ma, L. Luo and S. Huang, *J. Colloid Interface Sci.*, 2021, **604**, 178–187.
15 H. Kim, J. Ge, J. Kim, S.-E. Choi, H. Lee, H. Lee, W. Park, Y. Yin and S. Kwon, *Nat. Photonics*, 2009, **3**, 534–540.
16 Y. Fang, Y. Ni, S.-Y. Leo, C. Taylor, V. Basile and P. Jiang, *Nat. Commun.*, 2015, **6**, 7416.
17 J.-S. Lee, K. Je and S.-H. Kim, *Adv. Funct. Mater.*, 2016, **26**, 4587–4594.
18 M. Gao, L. Li and Y. Song, *J. Mater. Chem. C*, 2017, **5**, 2971–2993.
19 Y. Wu, J. Ren, S. Zhang and S. Wu, *ACS Appl. Mater. Interfaces*, 2020, **12**, 10867–10874.
20 A. J. J. Kragt, D. C. Hoekstra, S. Stallinga, D. J. Broer and A. P. H. J. Schenning, *Adv. Mater.*, 2019, **31**, 1903120.
21 Y. Hu, Y. Zhang, D. Yang, D. Ma and S. Huang, *Mater. Adv.*, 2021, **2**, 6499–6518.
22 Y. Hu, D. Yang and S. Huang, *ACS Omega*, 2019, **4**, 18771–18779.
23 D. Yang, G. Liao and S. Huang, *Langmuir*, 2019, **35**, 8428–8435.
24 D. Yang, W. Luo, Y. Huang and S. Huang, *ACS Omega*, 2019, **4**, 528–534.
25 Y. Y. Diao, X. Y. Liu, G. W. Toh, L. Shi and J. Zi, *Adv. Funct. Mater.*, 2013, **23**, 5373–5380.
26 J. Hou, H. Zhang, Q. Yang, M. Li, L. Jiang and Y. Song, *Small*, 2015, **11**, 2738–2742.
27 M. Qin, Y. Huang, Y. Li, M. Su, B. Chen, H. Sun, P. Yong, C. Ye, F. Li and Y. Song, *Angew. Chem., Int. Ed.*, 2016, **55**, 6911–6914.
28 J. H. Holtz and S. A. Asher, *Nature*, 1997, **389**, 829–832.
29 O. D. Velev and E. W. Kaler, *Langmuir*, 1999, **15**, 3693–3698.
30 J. D. Debord and L. A. Lyon, *J. Phys. Chem. B*, 2000, **104**, 6327–6331.
31 X. Hu, G. Li, M. Li, J. Huang, Y. Li, Y. Gao and Y. Zhang, *Adv. Funct. Mater.*, 2008, **18**, 575–583.
32 Y. Takeoka, *J. Mater. Chem. C*, 2013, **1**, 6059–6074.
33 L. Bai, Z. Xie, W. Wang, C. Yuan, Y. Zhao, Z. Mu, Q. Zhong and Z. Gu, *ACS Nano*, 2014, **8**, 11094–11100.
34 A. Belmonte, Y. Y. Ussembayev, T. Bus, I. Nys, K. Neyts and A. Schenning, *Small*, 2020, **16**, e1905219.
35 M. Kuang, J. Wang and L. Jiang, *Chem. Soc. Rev.*, 2016, **45**, 6833–6854.
36 B. Zhu, Q. Fu, K. Chen and J. Ge, *Angew. Chem., Int. Ed.*, 2018, **57**, 252–256.
37 H. Zhang, H. Chen, J.-H. Lee, E. Kim, K.-Y. Chan, H. Venkatesan, M. H. Adegun, O. G. Agbabiaka, X. Shen, Q. Zheng, J. Yang and J.-K. Kim, *Adv. Funct. Mater.*, 2022, 32.
38 X. Hu, Z. Huang, X. Zhou, P. Li, Y. Wang, Z. Huang, M. Su, W. Ren, F. Li, M. Li, Y. Chen and Y. Song, *Adv. Mater.*, 2017, **29**, 1703236.
39 Y. Zhan, Y. Wang, Q. Cheng, C. Li, K. Li, H. Li, J. Peng, B. Lu, Y. Wang, Y. Song, L. Jiang and M. Li, *Angew. Chem., Int. Ed.*, 2019, **58**, 16456–16462.
40 Y. Takeoka, S. Yoshioka, A. Takano, S. Arai, K. Nueangnoraj, H. Nishihara, M. Teshima, Y. Ohtsuka and T. Seki, *Angew. Chem., Int. Ed.*, 2013, **52**, 7261–7265.
41 Q. Li, Y. Zhang, L. Shi, H. Qiu, S. Zhang, N. Qi, J. Hu, W. Yuan, X. Zhang and K.-Q. Zhang, *ACS Nano*, 2018, **12**, 3095–3102.
42 Y. Dong, Z. Ma, D.-P. Song, G. Ma and Y. Li, *ACS Nano*, 2021, **15**, 8770–8779.
43 I. B. Burgess, L. Mishchenko, B. D. Hatton, M. Kolle, M. Loncar and J. Aizenberg, *J. Am. Chem. Soc.*, 2011, **133**, 12430–12432.
44 K. Zhong, J. Li, L. Liu, S. Van Cleuvenbergen, K. Song and K. Clays, *Adv. Mater.*, 2018, **30**, 1707246.
45 Y. Qi, W. Niu, S. Zhang, S. Wu, L. Chu, W. Ma and B. Tang, *Adv. Funct. Mater.*, 2019, **29**, 1906799.
46 D. Yang, G. Liao and S. Huang, *J. Mater. Chem. C*, 2019, **7**, 11776–11782.
47 H. S. Lee, T. S. Shim, H. Hwang, S.-M. Yang and S.-H. Kim, *Chem. Mater.*, 2013, **25**, 2684–2690.
48 F. Liu, S. Zhang, Y. Meng and B. Tang, *Small*, 2020, **16**, 2002319.
49 D. Yang, Y. Hu, Y. Hu and S. Huang, *J. Phys. Chem. C*, 2020, **124**, 6328–6336.
50 X. Yang, D. Yang, Y. Chen, Y. Hu and S. Huang, *Part. Part. Syst. Charact.*, 2020, **37**, 2000043.
51 C. Ouyang, Y. Zhang, D. Yang, D. Ma and S. Huang, *J. Mater. Chem. C*, 2021, **9**, 4466–4473.
52 S. Yu, Z. Tian, D. Yang, X. Zhou, D. Ma and S. Huang, *Adv. Mater. Interfaces*, 2021, **8**, 2100789.
53 S. Chen, D. Bu, Y. Hu, X. Xiao, D. Yang, D. Ma and S. Huang, *Adv. Photonics Res.*, 2021, **3**, 2100246.

54 Z. Tian, Z. Zhang, D. Zhang, D. Yang, C. Cao and S. Huang, *ACS Appl. Nano Mater.*, 2022, **5**, 12787–12796.
55 C. Xu, C. Huang, D. Yang, L. Luo and S. Huang, *ACS Omega*, 2022, **7**, 7320–7326.
56 Z. Zhang, B. Wei, D. Yang and S. Huang, *Adv. Mater. Interfaces*, 2022, **9**, 2201252.
57 J. R. Lawrence, Y. R. Ying, P. Jiang and S. H. Foulger, *Adv. Mater.*, 2006, **18**, 300–303.
58 Z. Yin, H. Li, W. Xu, S. Cui, D. Zhou, X. Chen, Y. Zhu, G. Qin and H. Song, *Adv. Mater.*, 2016, **28**, 2518–2525.
59 X. Wu, R. Hong, J. Meng, R. Cheng, Z. Zhu, G. Wu, Q. Li, C.-F. Wang and S. Chen, *Angew. Chem., Int. Ed.*, 2019, **58**, 13556–13564.
60 B. Liu, Z. Meng, S. Wu, Y. Wu and S. Zhang, *Nanoscale Horiz.*, 2018, **3**, 616–623.
61 W.-Y. Yu, D.-K. Ma, D.-P. Yang, X.-G. Yang, Q.-L. Xu, W. Chen and S. Huang, *Phys. Chem. Chem. Phys.*, 2020, **22**, 20202–20211.
62 J. Hou, M. Li and Y. Song, *Angew. Chem., Int. Ed.*, 2018, **57**, 2544–2553.
63 J. Ge and Y. Yin, *Angew. Chem., Int. Ed.*, 2011, **50**, 1492–1522.
64 A. Yadav, N. Yadav, V. Agrawal, S. P. Polyutov, A. S. Tsipotan, S. V. Karpov, V. V. Slabko, V. S. Yadav, Y. Wu, H. Zheng and S. RamaKrishna, *J. Mater. Chem. C*, 2021, **9**, 3368–3383.
65 G. Chen and W. Hong, *Adv. Opt. Mater.*, 2020, **8**, 2000984.
66 J. B. Kim, S. Y. Lee, J. M. Lee and S.-H. Kim, *ACS Appl. Mater. Interfaces*, 2019, **11**, 14485–14509.
67 Y. Zhao, L. Shang, Y. Cheng and Z. Gu, *Acc. Chem. Res.*, 2014, **47**, 3632–3642.
68 G. Chen and W. Hong, *Adv. Opt. Mater.*, 2020, **8**, 2000984.
69 J. Hou, M. Li and Y. Song, *Nano Today*, 2018, **22**, 132–144.
70 P. Wu, J. Wang and L. Jiang, *Mater. Horiz.*, 2020, **7**, 338–365.
71 E. S. A. Goerlitzer, R. N. K. Taylor and N. Vogel, *Adv. Mater.*, 2018, **30**, 1706654.
72 J. Yang, M. K. Choi, D.-H. Kim and T. Hyeon, *Adv. Mater.*, 2016, **28**, 1176–1207.
73 G. von Freymann, V. Kitaev, B. V. Lotschz and G. A. Ozin, *Chem. Soc. Rev.*, 2013, **42**, 2528–2554.
74 Y. Wang, X. Cao, J. Cheng, B. Yao, Y. Zhao, S. Wu, B. Ju, S. Zhang, X. He and W. Niu, *ACS Nano*, 2021, **15**, 3509–3521.
75 W. Ma, Y. Kou, P. Zhao and S. Zhang, *ACS Appl. Polym. Mater.*, 2020, **2**, 1605–1613.
76 Y. F. Yue, M. A. Haque, T. Kurokawa, T. Nakajima and J. P. Gong, *Adv. Mater.*, 2013, **25**, 3106–3110.
77 M. A. Haque, G. Kamita, T. Kurokawa, K. Tsujii and J. P. Gong, *Adv. Mater.*, 2010, **22**, 5110–5114.
78 J. Ge, Y. Hu and Y. Yin, *Angew. Chem., Int. Ed.*, 2007, **46**, 7428–7431.
79 J. Ge and Y. Yin, *Adv. Mater.*, 2008, **20**, 3485–3491.
80 X.-Q. Wang, C.-F. Wang, Z.-F. Zhou and S. Chen, *Adv. Opt. Mater.*, 2014, **2**, 652–662.
81 X. L. Xu, G. Friedman, K. D. Humfeld, S. A. Majetich and S. A. Asher, *Adv. Mater.*, 2001, **13**, 1681–1684.
82 X. L. Xu, G. Friedman, K. D. Humfeld, S. A. Majetich and S. A. Asher, *Chem. Mater.*, 2002, **14**, 1249–1256.
83 Z. Li, F. Yang and Y. Yin, *Adv. Funct. Mater.*, 2020, 30.
84 M. Wang, L. He and Y. Yin, *Mater. Today*, 2013, **16**, 110–116.
85 L. He, M. Wang, J. Ge and Y. Yin, *Acc. Chem. Res.*, 2012, **45**, 1431–1440.
86 K. J. M. Bishop, C. E. Wilmer, S. Soh and B. A. Grzybowski, *Small*, 2009, **5**, 1600–1630.
87 Y. Kraftmakher, *Eur. J. Phys.*, 2007, **28**, 409–414.
88 J. Ge, L. He, Y. Hu and Y. Yin, *Nanoscale*, 2011, **3**, 177–183.
89 G. M. Whitesides and M. Boncheva, *Proc. Natl. Acad. Sci. U. S. A.*, 2002, **99**, 4769–4774.
90 J. Ge, Y. Hu, M. Biasini, W. P. Beyermann and Y. Yin, *Angew. Chem., Int. Ed.*, 2007, **46**, 4342–4345.
91 J. Ge, L. He, J. Goebl and Y. Yin, *J. Am. Chem. Soc.*, 2009, **131**, 3484–3486.
92 Y. Hu, L. He and Y. Yin, *Small*, 2012, **8**, 3795–3799.
93 G. S. Roberts, R. Sanchez, R. Kemp, T. Wood and P. Bartlett, *Langmuir*, 2008, **24**, 6530–6541.
94 M. F. Hsu, E. R. Dufresne and D. A. Weitz, *Langmuir*, 2005, **21**, 4881–4887.
95 J. Ge, J. Goebl, L. He, Z. Lu and Y. Yin, *Adv. Mater.*, 2009, **21**, 4259–4264.
96 T. Thurn-Albrecht, J. Schotter, C. A. Kastle, N. Emley, T. Shibauchi, L. Krusin-Elbaum, K. Guarini, C. T. Black, M. T. Tuominen and T. P. Russell, *Science*, 2000, **290**, 2126–2129.
97 Y. Lei and W. K. Chim, *J. Am. Chem. Soc.*, 2005, **127**, 1487–1492.
98 D. G. Choi, S. Kim, S. G. Jang, S. M. Yang, J. R. Jeong and S. C. Shin, *Chem. Mater.*, 2004, **16**, 4208–4211.
99 A. Kosiorek, W. Kandulski, P. Chudzinski, K. Kempa and M. Giersig, *Nano Lett.*, 2004, **4**, 1359–1363.
100 Y. N. Xia, B. Gates, Y. D. Yin and Y. Lu, *Adv. Mater.*, 2000, **12**, 693–713.
101 S. Venkatesh, P. Jiang and B. Jiang, *Langmuir*, 2007, **23**, 8231–8235.
102 J. T. Han, D. H. Lee, C. Y. Ryu and K. W. Cho, *J. Am. Chem. Soc.*, 2004, **126**, 4796–4797.
103 W.-L. Min, P. Jiang and B. Jiang, *Nanotechnology*, 2008, 19.
104 Y. Li, T. Sasaki, Y. Shimizu and N. Koshizaki, *Small*, 2008, **4**, 2286–2291.
105 H. Yang and P. Jiang, *J. Colloid Interface Sci.*, 2010, **352**, 558–565.
106 C. Hagleitner, A. Hierlemann, D. Lange, A. Kummer, N. Kerness, O. Brand and H. Baltes, *Nature*, 2001, **414**, 293–296.
107 H. Q. Shi, W. B. Tsai, M. D. Garrison, S. Ferrari and B. D. Ratner, *Nature*, 1999, **398**, 593–597.
108 G. Zhang, D. Y. Wang, Z. Z. Gu, J. Hartmann and H. Mohwald, *Chem. Mater.*, 2005, **17**, 5268–5274.
109 C. Lopez, *Adv. Mater.*, 2003, **15**, 1679–1704.
110 C. Haginoya, M. Ishibashi and K. Koike, *Appl. Phys. Lett.*, 1997, **71**, 2934–2936.
111 T. Fujimura, T. Tamura, T. Itoh, C. Haginoya, Y. Komori and T. Koda, *Appl. Phys. Lett.*, 2001, **78**, 1478–1480.

112 D. G. Choi, H. K. Yu, S. G. Jang and S. M. Yang, *J. Am. Chem. Soc.*, 2004, **126**, 7019–7025.
113 B. J. Y. Tan, C. H. Sow, K. Y. Lim, F. C. Cheong, G. L. Chong, A. T. S. Wee and C. K. Ong, *J. Phys. Chem. B*, 2004, **108**, 18575–18579.
114 X. Yan, J. M. Yao, G. Lu, X. Li, J. H. Zhang, K. Han and B. Yang, *J. Am. Chem. Soc.*, 2005, **127**, 7688–7689.
115 Z. Ren, X. Li, J. Zhang, W. Li, X. Zhang and B. Yang, *Langmuir*, 2007, **23**, 8272–8276.
116 Z. Sun and B. Yang, *Sci. China: Chem.*, 2011, **54**, 275–285.
117 Z. Wang, J. Zhang, J. Xie, C. Li, Y. Li, S. Liang, Z. Tian, T. Wang, H. Zhang, H. Li, W. Xu and B. Yang, *Adv. Funct. Mater.*, 2010, **20**, 3784–3790.
118 X. Yan, J. M. Yao, G. A. Lu, X. Chen, K. Zhang and B. Yang, *J. Am. Chem. Soc.*, 2004, **126**, 10510–10511.
119 T. Ito, C. Katsura, H. Sugimoto, E. Nakanishi and K. Inomata, *Langmuir*, 2013, **29**, 13951–13957.
120 P. Jiang, *Chem. Commun.*, 2005, 1699–1701.
121 C.-H. Sun, W.-L. Min and P. Jiang, *Chem. Commun.*, 2008, 3163–3165.
122 P. A. Rundquist, P. Photinos, S. Jagannathan and S. A. Asher, *J. Chem. Phys.*, 1989, **91**, 4932–4941.
123 S. A. Asher, J. Holtz, L. Liu and Z. Wu, *J. Am. Chem. Soc.*, 1994, **116**, 4997–4998.
124 J. M. Weissman, H. B. Sunkara, A. S. Tse and S. A. Asher, *Science*, 1996, **274**, 959–960.
125 Z. B. Hu, X. H. Lu and J. Gao, *Adv. Mater.*, 2001, **13**, 1708–1712.
126 X. Li, D. Zhao, K. J. Shea, X. Li and X. Lu, *Mater. Horiz.*, 2021, **8**, 932–938.
127 P. Jiang and M. J. McFarland, *J. Am. Chem. Soc.*, 2004, **126**, 13778–13786.
128 S.-H. Kim, S.-J. Jeon, G.-R. Yi, C.-J. Heo, J. H. Choi and S.-M. Yang, *Adv. Mater.*, 2008, **20**, 1649–1655.
129 L. He, V. Malik, M. Wang, Y. Hu, F. E. Anson and Y. Yin, *Nanoscale*, 2012, **4**, 4438–4442.
130 Z. Li, C. Qian, W. Xu, C. Zhu and Y. Yin, *Sci. Adv.*, 2021, **7**, eabh1289.
131 Q. Fu, H. Zhu and J. Ge, *Adv. Funct. Mater.*, 2018, **28**, 1804628.
132 J. Luo, D. Qu, A. Tikhonov, J. Bohn and S. A. Asher, *J. Colloid Interface Sci.*, 2010, **345**, 131–137.
133 Y. Wu, Y. Wang, S. Zhang and S. Wu, *ACS Nano*, 2021, **15**, 15720–15729.
134 D. Yang, S. Ye and J. Ge, *J. Am. Chem. Soc.*, 2013, **135**, 18370–18376.
135 S.-H. Kim, S.-J. Jeon, W. C. Jeong, H. S. Park and S.-M. Yang, *Adv. Mater.*, 2008, **20**, 4129–4134.
136 S.-H. Kim, J.-M. Lim, W. C. Jeong, D.-G. Choi and S.-M. Yang, *Adv. Mater.*, 2008, **20**, 3211–3217.
137 H. Fudouzi and T. Sawada, *Langmuir*, 2006, **22**, 1365–1368.
138 M. Kepinska, A. Starczewska and P. Duka, *Opt. Mater.*, 2017, **73**, 437–440.
139 R. J. Gehr and R. W. Boyd, *Chem. Mater.*, 1996, **8**, 1807–1819.
140 D. Antonioli, S. Deregibus, G. Panzarasa, K. Sparnacci, M. Laus, L. Berti, L. Frezza, M. Gambini, L. Boarino, E. Enrico and D. Comoretto, *Polym. Int.*, 2012, **61**, 1294–1301.
141 R. Fenollosa and F. Meseguer, *Adv. Mater.*, 2003, **15**, 1282–1285.
142 F. Meseguer and R. Fenollosa, *J. Mater. Chem.*, 2005, **15**, 4577–4580.
143 L. Wang, Q. Yan and X. S. Zhao, *J. Mater. Chem.*, 2006, **16**, 4598–4602.
144 Y.-S. Cho, G.-R. Yi, J. H. Moon, D.-C. Kim, B.-J. Lee and S.-M. Yang, *J. Colloid Interface Sci.*, 2010, **341**, 209–214.
145 M. Del Pozo, C. Delaney, C. W. M. Bastiaansen, D. Diamond, A. Schenning and L. Florea, *ACS Nano*, 2020, **14**, 9832–9839.
146 T. Ding, K. Song, K. Clays and C.-H. Tung, *Langmuir*, 2010, **26**, 4535–4539.
147 Z. Zhang, W. Shen, C. Ye, Y. Luo, S. Li, M. Li, C. Xu and Y. Song, *J. Mater. Chem.*, 2012, **22**, 5300–5303.
148 J. J. Bohn, M. Ben-Moshe, A. Tikhonov, D. Qu, D. N. Lamont and S. A. Asher, *J. Colloid Interface Sci.*, 2010, **344**, 298–307.
149 J. M. Jethmalani and W. T. Ford, *Chem. Mater.*, 1996, **8**, 2138–2146.
150 J. Hu, X.-W. Zhao, Y.-J. Zhao, J. Li, W.-Y. Xu, Z.-Y. Wen, M. Xu and Z.-Z. Gu, *J. Mater. Chem.*, 2009, **19**, 5730–5736.
151 H. Ding, C. Liu, B. Ye, F. Fu, H. Wang, Y. Zhao and Z. Gu, *ACS Appl. Mater. Interfaces*, 2016, **8**, 6796–6801.
152 Y. Xia, N. Trung Dac, M. Yang, B. Lee, A. Santos, P. Podsiadlo, Z. Tang, S. C. Glotzer and N. A. Kotov, *Nat. Nanotechnol.*, 2011, **6**, 580–587.
153 G. H. Lee, T. M. Choi, B. Kim, S. H. Han, J. M. Lee and S.-H. Kim, *ACS Nano*, 2017, **11**, 11350–11357.
154 J. B. Kim, C. Chae, S. H. Han, S. Y. Lee and S.-H. Kim, *Sci. Adv.*, 2021, **7**, eabj8780.
155 Z. Yan, Z. Zhang, W. Wu, X. Ji, S. Sun, Y. Jiang, C. C. Tan, L. Yang, C. T. Chong, C.-W. Qiu and R. Zhao, *Nat. Nanotechnol.*, 2021, **16**, 795–801.
156 Y. Hu, D. Yang, D. Ma and S. Huang, *Chem. Eng. J.*, 2022, **429**, 132342.
157 Z. Li and Y. Yin, *Adv. Mater.*, 2019, **31**, 1807061.
158 L. He, Y. Hu, H. Kim, J. Ge, S. Kwon and Y. Yin, *Nano Lett.*, 2010, **10**, 4708–4714.
159 Z. Li, X. Wang, L. Han, C. Zhu, H. Xin and Y. Yin, *Adv. Mater.*, 2022, **34**, 2107398.
160 O. L. J. Pursiainen, J. J. Baumberg, H. Winkler, B. Viel, P. Spahn and T. Ruhl, *Adv. Mater.*, 2008, **20**, 1484–1487.
161 C. E. Finlayson, P. Spahn, D. R. E. Snoswell, G. Yates, A. Kontogeorgos, A. I. Haines, G. P. Hellmann and J. J. Baumberg, *Adv. Mater.*, 2011, **23**, 1540–1544.
162 C. G. Schaefer, M. Gallei, J. T. Zahn, J. Engelhardt, G. P. Hellmann and M. Rehahn, *Chem. Mater.*, 2013, **25**, 2309–2318.
163 Q. Zhao, C. E. Finlayson, C. G. Schaefer, P. Spahn, M. Gallei, L. Herrmann, A. V. Petukhov and J. J. Baumberg, *Adv. Opt. Mater.*, 2016, **4**, 1494–1500.
164 M. Gallei, *Macromol. Rapid Commun.*, 2018, **39**, 1800428.
165 Q. Zhao, C. E. Finlayson, D. R. E. Snoswell, A. Haines, C. Schaefer, P. Spahn, G. P. Hellmann, A. V. Petukhov,

L. Herrmann, P. Burdet, P. A. Midgley, S. Butler, M. Mackley, Q. Guo and J. J. Baumberg, *Nat. Commun.*, 2016, **7**, 11661.
166 H. Li, P. Wu, G. Zhao, J. Guo and C. Wang, *J. Colloid Interface Sci.*, 2021, **584**, 145–153.
167 Z. Ren, X. Zhang, J. Zhang, X. Li, X. Pan, X. Fei, Z. Cui and B. Yang, *J. Mater. Chem.*, 2008, **18**, 3536–3538.
168 X. Liu, J. Liu, B. Wei, D. Yang, L. Luo, D. Ma and S. Huang, *Adv. Sci.*, 2023, 2302240, DOI: **10.1002/advs.202302240**.
169 S. Xiao, T. Wang, T. Liu, C. Zhou, X. Jiang and J. Zhang, *J. Phys. D: Appl. Phys.*, 2020, **53**, 503002.
170 L. Lin, M. Wang, X. Peng, E. N. Lissek, Z. Mao, L. Scarabelli, E. Adkins, S. Coskun, H. E. Unalan, B. A. Korgel, L. M. Liz-Marzan, E.-L. Florin and Y. Zheng, *Nat. Photonics*, 2018, **12**, 195–201.
171 A. Kuzyk, R. Schreiber, H. Zhang, A. O. Govorov, T. Liedl and N. Liu, *Nat. Mater.*, 2014, **13**, 862–866.
172 D. B. Litt, M. R. Jones, M. Hentschel, Y. Wang, S. Yang, H. D. Ha, X. Zhang and A. P. Alivisatos, *Nano Lett.*, 2018, **18**, 859–864.
173 M. Li, Q. Lyu, B. Peng, X. Chen, L. Zhang and J. Zhu, *Adv. Mater.*, 2022, **34**, 2110488.
174 Y. Qi, S. Zhang and A.-H. Lu, *Small Struct.*, 2022, **3**, 2200101.
175 Y. Iwayama, J. Yamanaka, Y. Takiguchi, M. Takasaka, K. Ito, T. Shinohara, T. Sawada and M. Yonese, *Langmuir*, 2003, **19**, 977–980.
176 B. Viel, T. Ruhl and G. P. Hellmann, *Chem. Mater.*, 2007, **19**, 5673–5679.
177 S. Furumi, T. Kanai and T. Sawada, *Adv. Mater.*, 2011, **23**, 3815–3820.
178 S. Shang, Z. Liu, Q. Zhang, H. Wang and Y. Li, *J. Mater. Chem. A*, 2015, **3**, 11093–11097.
179 C. G. Schaefer, T. Winter, S. Heidt, C. Dietz, T. Ding, J. J. Baumberg and M. Gallei, *J. Mater. Chem. C*, 2015, **3**, 2204–2214.
180 J. Chen, L. Xu, M. Yang, X. Chen, X. Chen and W. Hong, *Chem. Mater.*, 2019, **31**, 8918–8926.
181 G. H. Lee, J. B. Kim, T. M. Choi, J. M. Lee and S.-H. Kim, *Small*, 2019, **15**, 1804548.
182 C.-H. Hsieh, Y.-C. Lu and H. Yang, *ACS Appl. Mater. Interfaces*, 2020, **12**, 36478–36484.
183 E. Miwa, K. Watanabe, F. Asai, T. Seki, K. Urayama, J. Odent, J.-M. Raquez and Y. Takeoka, *ACS Appl. Polym. Mater.*, 2020, **2**, 4078–4089.
184 G. H. Lee, S. H. Han, J. B. Kim, D. J. Kim, S. Lee, W. M. Hamonangan, J. M. Lee and S.-H. Kim, *ACS Appl. Polym. Mater.*, 2020, **2**, 706–714.
185 K. Watanabe, E. Miwa, F. Asai, T. Seki, K. Urayama, T. Nakatani, S. Fujinami, T. Hoshino, M. Takata, C. Liu, K. Mayumi, K. Ito and Y. Takeoka, *ACS Materials Lett.*, 2020, **2**, 325–330.
186 Y. G. Kim, S. Park, Y. H. Choi, S. H. Han and S.-H. Kim, *ACS Nano*, 2021, **15**, 12438–12448.
187 J. H. Kim, J. B. Kim, Y. H. Choi, S. Park and S.-H. Kim, *Small*, 2022, **18**, 2105225.
188 Q. Lyu, S. Wang, B. Peng, X. Chen, S. Du, M. Li, L. Zhang and J. Zhu, *Small*, 2021, **17**, 2103271.
189 P. Wu, X. Shen, C. G. Schafer, J. Pan, J. Guo and C. Wang, *Nanoscale*, 2019, **11**, 20015–20023.
190 B. Wei, Y. Hu, D. Yang and S. Huang, *Adv. Sensor Res.*, 2023, 2200078, DOI: **10.1002/adsr.202200078**.
191 S. H. Foulger, P. Jiang, A. C. Lattam, D. W. Smith and J. Ballato, *Langmuir*, 2001, **17**, 6023–6026.
192 J. M. Jethmalani and W. T. Ford, *Langmuir*, 1997, **13**, 3338–3344.
193 X. Jia, J. Wang, K. Wang and J. Zhu, *Langmuir*, 2015, **31**, 8732–8737.
194 Z. Liu, Q. Zhang, H. Wang and Y. Li, *J. Colloid Interface Sci.*, 2013, **406**, 18–23.
195 S. Shang, Q. Zhang, H. Wang and Y. Li, *J. Colloid Interface Sci.*, 2016, **483**, 11–16.
196 L. Zhang, M. Li, Q. Lyu and J. Zhu, *Polym. Chem.*, 2020, **11**, 6413–6422.
197 C. G. Schaefer, C. Lederle, K. Zentel, B. Stuehn and M. Gallei, *Macromol. Rapid Commun.*, 2014, **35**, 1852–1860.
198 H. Ding, C. Liu, H. Gu, Y. Zhao, B. Wang and Z. Gu, *ACS Photonics*, 2014, **1**, 121–126.
199 D. Yang, S. Ye and J. Ge, *Adv. Funct. Mater.*, 2014, **24**, 3197–3205.
200 Z. Zhang, B. Wei, Y. Hu, D. Yang, D. Ma and S. Huang, *Cell Rep. Phys. Sci.*, 2023, **4**, 101387.
201 Y. Hu, B. Wei, D. Yang, D. Ma and S. Huang, *ACS Appl. Mater. Interfaces*, 2022, **14**, 11672–11680.
202 G. H. Lee, S. H. Han, J. B. Kim, J. H. Kim, J. M. Lee and S.-H. Kim, *Chem. Mater.*, 2019, **31**, 8154–8162.
203 A. Li, D. Yang, C. Cao, Y. Hu and S. Huang, *Adv. Mater. Interfaces*, 2022, **9**, 2200051.
204 C. E. Reese, A. V. Mikhonin, M. Kamenjicki, A. Tikhonov and S. A. Asher, *J. Am. Chem. Soc.*, 2004, **126**, 1493–1496.
205 T. Kanai, D. Lee, H. C. Shum and D. A. Weitz, *Small*, 2010, **6**, 807–810.
206 M. Chen, L. Zhou, Y. Guan and Y. Zhang, *Angew. Chem., Int. Ed.*, 2013, **52**, 9961–9965.
207 H. Ma, M. Zhu, W. Luo, W. Li, K. Fang, F. Mou and J. Guan, *J. Mater. Chem. C*, 2015, **3**, 2848–2855.
208 T. Kanai, H. Yano, N. Kobayashi and T. Sawada, *ACS Macro Lett.*, 2017, **6**, 1196–1200.
209 S. Shang, P. Zhu, H. Wang, Y. Li and S. Yang, *ACS Appl. Mater. Interfaces*, 2020, **12**, 50844–50851.
210 X. Gong, C. Hou, Q. Zhang, Y. Li and H. Wang, *ACS Appl. Mater. Interfaces*, 2020, **12**, 51225–51235.
211 Y. Liu, Q. Fan, G. Zhu, G. Shi, H. Ma, W. Li, T. Wu, J. Chen, Y. Yin and J. Guan, *Mater. Horiz.*, 2021, **8**, 2032–2040.
212 M. Kumoda, M. Watanabe and Y. Takeoka, *Langmuir*, 2006, **22**, 4403–4407.
213 Y. Hu, D. Yang, D. Ma and S. Huang, *Adv. Opt. Mater.*, 2022, **10**, 2200769.
214 H. Li, M. Zhu, F. Tian, W. Hua, J. Guo and C. Wang, *Chem. Eng. J.*, 2021, **426**, 130683.
215 J. Ge, H. Lee, L. He, J. Kim, Z. Lu, H. Kim, J. Goebl, S. Kwon and Y. Yin, *J. Am. Chem. Soc.*, 2009, **131**, 15687–15694.

216 C. Zhu, W. Xu, L. Chen, W. Zhang, H. Xu and Z.-Z. Gu, *Adv. Funct. Mater.*, 2011, **21**, 2043–2048.
217 Y. Hu, L. He, X. Han, M. Wang and Y. Yin, *Nano Res.*, 2015, **8**, 611–620.
218 P. Yang, H. Li, S. Zhang, L. Chen, H. Zhou, R. Tang, T. Zhou, F. Bao, Q. Zhang, L. He and X. Zhang, *Nanoscale*, 2016, **8**, 19036–19042.
219 S. Zhang, C. Li, Y. Yu, Z. Zhu, W. Zhang, R. Tang, W. Sun, W. Xie, Y. Li, J. Yu, L. He and X. Zhang, *J. Mater. Chem. C*, 2018, **6**, 5528–5535.
220 J. Chi, C. Shao, Y. Zhang, D. Ni, T. Kong and Y. Zhao, *Nanoscale*, 2019, **11**, 12898–12904.
221 J. Zhang, Y. Qin, Y. Shen, C. Jiang, Y.-T. Tao, S. Chen, B. B. Xu and Z. Yu, *Adv. Mater. Interfaces*, 2021, **8**, 2001201.
222 Y. Fang, W. Fei, X. Shen, J. Guo and C. Wang, *Mater. Horiz.*, 2021, **8**, 2079–2087.
223 J. Ge, Y. Hu, T. Zhang, T. Huynh and Y. Yin, *Langmuir*, 2008, **24**, 3671–3680.
224 Y. Hu, L. He and Y. Yin, *Angew. Chem., Int. Ed.*, 2011, **50**, 3747–3750.
225 M. Wang, L. He, Y. Hu and Y. Yin, *J. Mater. Chem. C*, 2013, **1**, 6151–6156.
226 M. Wang, L. He, W. Xu, X. Wang and Y. Yin, *Angew. Chem., Int. Ed.*, 2015, **54**, 7077–7081.
227 J. Liu, M. Xiao, C. Li, H. Li, Z. Wu, Q. Zhu, R. Tang, A. B. Xu and L. He, *J. Mater. Chem. C*, 2019, **7**, 15042–15048.
228 Z. Li, M. Wang, X. Zhang, D. Wang, W. Xu and Y. Yin, *Nano Lett.*, 2019, **19**, 6673–6680.
229 H. Li, C. R. Li, W. Sun, Y. Z. Wang, W. Q. Hua, J. J. Liu, S. M. Zhang, Z. J. Chen, S. H. Wang, Z. Y. Wu, Q. S. Zhu, R. J. Tang, J. Yu, L. He, G. A. Ozin and X. H. Zhang, *Adv. Mater.*, 2019, **31**, 1900388.
230 J. Liu, Y. Mao and J. Ge, *Nanoscale*, 2012, **4**, 1598–1605.
231 S.-N. Yin, C.-F. Wang, Z.-Y. Yu, J. Wang, S.-S. Liu and S. Chen, *Adv. Mater.*, 2011, **23**, 2915–2919.
232 S.-S. Liu, C.-F. Wang, X.-Q. Wang, J. Zhang, Y. Tian, S.-N. Yin and S. Chen, *J. Mater. Chem. C*, 2014, **2**, 9431–9438.
233 H. Wang, S. Yang, S.-N. Yin, L. Chen and S. Chen, *ACS Appl. Mater. Interfaces*, 2015, **7**, 8827–8833.
234 H. S. Lee, J. H. Kim, J.-S. Lee, J. Y. Sim, J. Y. Seo, Y.-K. Oh, S.-M. Yang and S.-H. Kim, *Adv. Mater.*, 2014, **26**, 5801–5807.
235 S. K. Nam, J. B. Kim, S. H. Han and S.-H. Kim, *ACS Nano*, 2020, **14**, 15714–15722.
236 T. S. Shim, S.-H. Kim, J. Y. Sim, J.-M. Lim and S.-M. Yang, *Adv. Mater.*, 2010, **22**, 4494–4498.
237 J. Liu, Y. Mao and J. Ge, *J. Mater. Chem. C*, 2013, **1**, 6129–6135.
238 M. G. Han, C.-J. Heo, C. G. Shin, H. Shim, J. W. Kim, Y. W. Jin and S. Lee, *J. Mater. Chem. C*, 2013, **1**, 5791–5798.
239 M. G. Han, C.-J. Heo, H. Shim, C. G. Shin, S.-J. Lim, J. W. Kim, Y. W. Jin and S. Lee, *Adv. Opt. Mater.*, 2014, **2**, 535–541.
240 Y. Luo, J. Zhang, A. Sun, C. Chu, S. Zhou, J. Guo, T. Chen and G. Xu, *J. Mater. Chem. C*, 2014, **2**, 1990–1994.
241 H.-S. Yang, J. Jang, B.-S. Lee, T.-H. Kang, J.-J. Park and W.-R. Yu, *Langmuir*, 2017, **33**, 9057–9065.
242 K. Chen, Q. Fu, S. Ye and J. Ge, *Adv. Funct. Mater.*, 2017, **27**, 1702825.
243 M. G. Han, C. G. Shin, S.-J. Jeon, H. Shim, C.-J. Heo, H. Jin, J. W. Kim and S. Lee, *Adv. Mater.*, 2012, **24**, 6438–6444.
244 G. Bao, W. Yu, Q. Fu and J. Ge, *Adv. Opt. Mater.*, 2022, **10**, 2201188.
245 Q. Fu, W. Yu, G. Bao and J. Ge, *Nat. Commun.*, 2022, **13**, 7007.
246 H. Huang, H. Li, X. Shen, K. Gu, J. Guo and C. Wang, *Chem. Eng. J.*, 2022, **429**, 132437.
247 J. B. Kim, S. Y. Lee, N. G. Min, S. Y. Lee and S.-H. Kim, *Adv. Mater.*, 2020, **32**, 2001384.
248 J. B. Kim, J.-W. Kim, M. Kim and S.-H. Kim, *Small*, 2022, **18**, 2201437.
249 T. Nisisako, T. Torii, T. Takahashi and Y. Takizawa, *Adv. Mater.*, 2006, **18**, 1152–1156.
250 P. Shen, Y. Zhang, Z. Cai, R. Liu, X. Xu, R. Li, J.-J. Wang and D. A. Yang, *J. Mater. Chem. C*, 2021, **9**, 5840–5857.
251 C. Fenzl, T. Hirsch and O. S. Wolfbeis, *Angew. Chem., Int. Ed.*, 2014, **53**, 3318–3335.
252 Y. Dai, H. Bao, J. Lin, P. Rungta and S. H. Foulger, *J. Colloid Interface Sci.*, 2012, **377**, 485–488.
253 Y. Zhang and J. Ge, *RSC Adv.*, 2020, **10**, 10972–10979.
254 W. Liu, L. Bao, B. Liu, R. Liu, L. Li and Z. Wu, *J. Colloid Interface Sci.*, 2020, **580**, 681–689.
255 B. Ye, F. Rong, H. Gu, Z. Xie, Y. Cheng, Y. Zhao and Z. Gu, *Chem. Commun.*, 2013, **49**, 5331–5333.
256 J. H. Holtz, J. S. W. Holtz, C. H. Munro and S. A. Asher, *Anal. Chem.*, 1998, **70**, 780–791.
257 S. A. Asher, A. C. Sharma, A. V. Goponenko and M. M. Ward, *Anal. Chem.*, 2003, **75**, 1676–1683.
258 J. Qin, B. Dong, L. Cao and W. Wang, *J. Mater. Chem. C*, 2018, **6**, 4234–4242.
259 Y. J. Lee and P. V. Braun, *Adv. Mater.*, 2003, **15**, 563–566.
260 X. Jia, K. Wang, J. Wang, Y. Hu, L. Shen and J. Zhu, *Eur. Polym. J.*, 2016, **83**, 60–66.
261 G. Xie, S. Du, Q. Huang, M. Mo, Y. Gao, M. Li, J. Tao, L. Zhang and J. Zhu, *ACS Appl. Mater. Interfaces*, 2022, **14**, 5856–5866.
262 L. Kong, Y. Feng, W. Luo, F. Mou, K. Ying, Y. Pu, M. You, K. Fang, H. Ma and J. Guan, *Adv. Funct. Mater.*, 2020, **30**, 2005243.
263 K. Lee and S. A. Asher, *J. Am. Chem. Soc.*, 2000, **122**, 9534–9537.
264 M. Xu, A. V. Goponenko and S. A. Asher, *J. Am. Chem. Soc.*, 2008, **130**, 3113–3119.
265 M. Chen, Y. Zhang, S. Jia, L. Zhou, Y. Guan and Y. Zhang, *Angew. Chem., Int. Ed.*, 2015, **54**, 9257–9261.
266 Z. Tang, S. Jia, L. Yao, Y. Guan and Y. Zhang, *J. Colloid Interface Sci.*, 2018, **526**, 83–89.
267 W. Luo, Q. Cui, K. Fang, K. Chen, H. Ma and J. Guan, *Nano Lett.*, 2020, **20**, 803–811.
268 M. Kamenjicki and S. A. Asher, *Sens. Actuators, B*, 2005, **106**, 373–377.
269 L. Jin, Y. Zhao, X. Liu, Y. Wang, B. Ye, Z. Xie and Z. Gu, *Soft Matter*, 2012, **8**, 4911–4917.

270 S. Jia, Z. Tang, Y. Guan and Y. Zhang, *ACS Appl. Mater. Interfaces*, 2018, **10**, 14254–14258.
271 A. C. Sharma, T. Jana, R. Kesavamoorthy, L. J. Shi, M. A. Virji, D. N. Finegold and S. A. Asher, *J. Am. Chem. Soc.*, 2004, **126**, 2971–2977.
272 J. P. Walker and S. A. Asher, *Anal. Chem.*, 2005, **77**, 1596–1600.
273 V. L. Alexeev, S. Das, D. N. Finegold and S. A. Asher, *Clin. Chem.*, 2004, **50**, 2353–2360.
274 V. L. Alexeev, A. C. Sharma, A. V. Goponenko, S. Das, I. K. Lednev, C. S. Wilcox, D. N. Finegold and S. A. Asher, *Anal. Chem.*, 2003, **75**, 2316–2323.
275 C. Zhang, G. G. Cano and P. V. Braun, *Adv. Mater.*, 2014, **26**, 5678–5683.
276 Y. Zhang, Q. Fu and J. Ge, *Nat. Commun.*, 2015, **6**, 7510.
277 X. Jia, T. Zhang, J. Wang, K. Wang, H. Tan, Y. Hu, L. Zhang and J. Zhu, *Langmuir*, 2018, **34**, 3987–3992.
278 X. Dong, P. Wu, C. G. Schaefer, L. Zhang, C. E. Finlayson and C. Wang, *Mater. Des.*, 2018, **160**, 417–426.
279 X. Shen, P. Wu, C. G. Schafer, J. Guo and C. Wang, *Nanoscale*, 2019, **11**, 1253–1261.
280 J. He, X. Shen, H. Li, Y. Yao, J. Guo and C. Wang, *ACS Appl. Mater. Interfaces*, 2022, **14**, 27251–27261.
281 J. H. Kim, G. H. Lee, J. B. Kim and S.-H. Kim, *Adv. Funct. Mater.*, 2020, **30**, 2001318.
282 Y. Hu, Y. Zhang, T. Chen, D. Yang, D. Ma and S. Huang, *ACS Appl. Mater. Interfaces*, 2020, **12**, 45174–45183.
283 R. Xuan, Q. Wu, Y. Yin and J. Ge, *J. Mater. Chem.*, 2011, **21**, 3672–3676.
284 K. Chen, Y. Zhang and J. Ge, *ACS Appl. Mater. Interfaces*, 2019, **11**, 45256–45264.
285 D. Yang, C. Ouyang, Y. Zhang, D. Ma and S. Huang, *Adv. Mater. Interfaces*, 2021, **8**, 2001905.
286 D. Yang, C. Ouyang, Y. Zhang, D. Ma, Y. Ye, D. Bu and S. Huang, *J. Colloid Interface Sci.*, 2021, **590**, 134–143.
287 M. Qin, J. Li and Y. Song, *Anal. Chem.*, 2022, **94**, 9497–9507.
288 D. Yang, Y. Hu, D. Ma, J. Ge and S. Huang, *Research*, 2022, **2022**, 9838071.
289 L. Sun, Z. Chen, D. Xu and Y. Zhao, *Adv. Sci.*, 2022, **9**, 2105777.
290 Z. Chen, Y. Yu, J. Guo, L. Sun and Y. Zhao, *Adv. Funct. Mater.*, 2021, **31**, 2007527.
291 G. Isapour, B. H. Miller and M. Kolle, *Adv. Photonics Res.*, 2021, **3**, 2100043.
292 T. M. Choi, K. Je, J.-G. Park, G. H. Lee and S.-H. Kim, *Adv. Mater.*, 2018, **30**, 1803387.
293 T. Kanai, D. Lee, H. C. Shum, R. K. Shah and D. A. Weitz, *Adv. Mater.*, 2010, **22**, 4998–5002.
294 N. Iwata, T. Koike, K. Tokuhiro, R. Sato and S. Furumi, *ACS Appl. Mater. Interfaces*, 2021, **13**, 57893–57907.
295 Z. Zhang, B. Wei, D. Yang, D. Ma and S. Huang, *J. Colloid Interface Sci.*, 2023, **634**, 314–322.
296 Z. Cai, D. H. Kwak, D. Punihaole, Z. Hong, S. S. Velankar, X. Liu and S. A. Asher, *Angew. Chem., Int. Ed.*, 2015, **54**, 13036–13040.
297 Y. Gao, Y. Chen, M. Li, L. Jia, L. Zhang and J. Zhu, *Sens. Actuators, B*, 2021, **329**, 129137.
298 Y. Liu, Y. Zhang and Y. Guan, *Chem. Commun.*, 2009, 1867–1869.
299 J. Cai, W. Luo, J. Pan, G. Li, Y. Pu, L. Si, G. Shi, Y. Shao, H. Ma and J. Guan, *Adv. Sci.*, 2022, **9**, 2105239.
300 L. He, Y. Hu, M. Wang and Y. Yin, *ACS Nano*, 2012, **6**, 4196–4202.
301 Y. Zhang, Y. Jiang, X. Wu and J. Ge, *J. Mater. Chem. C*, 2017, **5**, 9288–9295.
302 J. Ge, S. Kwon and Y. Yin, *J. Mater. Chem.*, 2010, **20**, 5777–5784.
303 R. Xuan and J. Ge, *J. Mater. Chem.*, 2012, **22**, 367–372.
304 D. Yang, S. Ye and J. Ge, *Chem. Commun.*, 2015, **51**, 16972–16975.
305 S. Ye and J. Ge, *J. Mater. Chem. C*, 2015, **3**, 8097–8103.
306 L. Jia, M. Li, L. Jiang, H. Gao, H. Tan, B. Peng, J. Xu, L. Zhang and J. Zhu, *J. Mater. Chem. C*, 2020, **8**, 9286–9292.
307 Y. Li, Q. Fan, X. Wang, G. Liu, L. Chai, L. Zhou, J. Shao and Y. Yin, *Adv. Funct. Mater.*, 2021, **31**, 2010746.
308 J. Liao, C. Ye, J. Guo, C. E. Garciamendez-Mijares, P. Agrawal, X. Kuang, J. O. Japo, Z. Wang, X. Mu, W. Li, T. Ching, L. S. Mille, C. Zhu, X. Zhang, Z. Gu and Y. S. Zhang, *Mater. Today*, 2022, **56**, 29–41.
309 Y. Zhang, L. Zhang, C. Zhang, J. Wang, J. Liu, C. Ye, Z. Dong, L. Wu and Y. Song, *Nat. Commun.*, 2022, **13**, 7095.
310 K. Liu, H. Ding, S. Li, Y. Niu, Y. Zeng, J. Zhang, X. Du and Z. Gu, *Nat. Commun.*, 2022, **13**, 4563.
311 Y. Xie, Y. Meng, W. Wang, E. Zhang, J. Leng and Q. Pei, *Adv. Funct. Mater.*, 2018, **28**, 1802430.
312 B. Hardwick, W. Jackson, G. Wilson and A. W. H. Mau, *Adv. Mater.*, 2001, **13**, 980–984.
313 A. Mullard, *Nat. Med.*, 2010, **16**, 361.
314 E. L. Prime and D. H. Solomon, *Angew. Chem., Int. Ed.*, 2010, **49**, 3726–3736.
315 B. Yoon, J. Lee, I. S. Park, S. Jeon, J. Lee and J.-M. Kim, *J. Mater. Chem. C*, 2013, **1**, 2388–2403.
316 R. Xuan and J. Ge, *Langmuir*, 2011, **27**, 5694–5699.
317 W. Wang, Y. Zhou, L. Yang, X. Yang, Y. Yao, Y. Meng and B. Tang, *Adv. Funct. Mater.*, 2022, **32**, 2204744.
318 D. Yang, Y. Qin, S. Ye and J. Ge, *Adv. Funct. Mater.*, 2014, **24**, 817–825.
319 S. Shang, Q. Zhang, H. Wang and Y. Li, *J. Colloid Interface Sci.*, 2017, **485**, 18–24.
320 Y. Dong, A. Bazrafshan, A. Pokutta, F. Sulejmani, W. Sun, J. D. Combs, K. C. Clarke and K. Salaita, *ACS Nano*, 2019, **13**, 9918–9926.
321 C. Xu, D. Yang, L. Luo, D. Ma and S. Huang, *Adv. Photonics Res.*, 2021, **2**, 2000197.
322 H. Li, G. Zhao, M. Zhu, J. Guo and C. Wang, *ACS Appl. Mater. Interfaces*, 2022, **14**, 14618–14629.
323 S. Ye, Q. Fu and J. Ge, *Adv. Funct. Mater.*, 2014, **24**, 6430–6438.
324 H. Hu, J. Tang, H. Zhong, Z. Xi, C. Chen and Q. Chen, *Sci. Rep.*, 2013, **3**, 1484.
325 H. Hu, H. Zhong, C. Chen and Q. Chen, *J. Mater. Chem. C*, 2014, **2**, 3695–3702.
326 Y. Hu, D. Yang and S. Huang, *Adv. Opt. Mater.*, 2020, **8**, 1901541.
327 S. Song, Y. Liu, X. Liu, J. Ge, D. Ge and L. Yang, *J. Mater. Chem. C*, 2022, **10**, 3114–3120.

328 W. Wang, X. Fan, F. Li, J. Qiu, M. M. Umair, W. Ren, B. Ju, S. Zhang and B. Tang, *Adv. Opt. Mater.*, 2018, **6**, 1701093.
329 H. Ma, Y. Tan, J. Cao, S. C. Lian, K. Chen, W. Luo and J. Guan, *J. Mater. Chem. C*, 2018, **6**, 4531–4540.
330 S.-H. Kim, S.-H. Kim, W. C. Jeong and S.-M. Yang, *Chem. Mater.*, 2009, **21**, 4993–4999.
331 Q. Fu, A. Chen, L. Shi and J. Ge, *Chem. Commun.*, 2015, **51**, 7382–7385.
332 X. Shen, J. Du, J. Sun, J. Guo, X. Hu and C. Wang, *ACS Appl. Mater. Interfaces*, 2020, **12**, 39639–39648.
333 X. Chen, P. Ren, M. Li, Q. Lyu, L. Zhang and J. Zhu, *Chem. Eng. J.*, 2021, **426**, 131259.